Condensed Matter and Nanostructured Materials

Cumulative Habilitation Thesis

Hamburg University of Technology

TUHH

written by

Dr. rer. nat. Tommy Hofmann

Berlin

2023

DOI: https://doi.org/10.15480/882.13558
ORCID ID: https://orcid.org/0009-0001-3690-3258

In Copyright: http://rightsstatements.org/vocab/InC/1.0/

Meiner Mutter und meinem Vater in Liebe und Dankbarkeit. Ihnen verdanke ich Alles.

Acknowledgments

Writing an acknowledgment is a tricky thing. Many people contribute to a project like this. They support the writer on professional or on private levels over many years. But often these lines blur and it appears impossible to honor their help in any adequate way. So let me try a fairly humble approach. To all colleagues, friends and my family, to companions of the past, present and maybe future I simply say "Thank You"!

That said, a few honorable mentions are required:

Klaus Habicht: He is my chief in command for many years. I owe him for the position, which I currently hold. The support during hard times will never be forgotten. I thank him for supporting everything related to my research interests that center around "stuff in confinement". Without him, this thesis would not have been possible. I also appreciate his exceptional patience in listening to the scientific monologues, which I enjoy so much.

Klaus Knorr: He gave the very first lecture that I ever attended at an university. I made my diploma in his group and he supervised me during my time as a PhD student. It was an awesome experience. He taught me much. The rest is history.

Patrick Huber: I know him since my first days in Prof. Knorr's group. Over the years he became one of my closest collaborators. I thank him for continuously involving me in his fascinating research projects. One day these experiments will save the world. He is always more than willing to discuss new scientific ideas or help with ongoing projects.

The Brookhaven crew: I had the honor to work for Ben Ocko as a postdoc for two years. He is a nice guy who taught me how to write a descent paper. From him I learned what it means to perform a proper synchrotron experiment. Let me simply state that sleeping is not foreseen. My gratitude goes also to Antonio Checco. He enlightened me with his definition of the "Golden Experiment". Sumit Kewelramani a fellow postdoc is a good friend since our time in Brookhaven. I miss our trips to Manhattan. They were always a welcome distraction.

Norbert Stüßer: I do not think that I discussed with anyone else more diverse topics. Our talks covered differential forms, tensors, Lebesque integrals, hydrodynamics, elasticity, magnetism, quantum mechanics, field theories, variational calculus and many things more. These discussions were always a delight. Whenever I had a new problem, that means roughly once a week, he had the appropriate book.

Andreas Hoser: First, I learned a lot from him about how to run a neutron scattering experiment and how to deal with external users. He called me Private, I called him Sergeant. Later, I learned even more about red wine. I became the apprentice, he is the master.

Dirk Wallacher: We are working together since the early days of my diploma thesis. I thank him for the invaluable support over many years. It was always a lot of fun. There is not more to say.

Abstract

This thesis marks the culmination of research activities on pore-confined and nanostructured matter that lasted over a decade. It starts with a comprehensive overview of studied porous materials as well as nanostructured surfaces. Nanoscale wetting is the first scientific core topic of the thesis. It elaborates on how X-ray scattering techniques in combination with nanosculptured substrates are utilized to validate the Augemented Young-Laplace equation on sub-10 nanometer length scales. The crystal structure of nanoconfined solids is at the forefront of the second core topic. As a highlight, elastic neutron scattering studies evidence quasi-single crystalline growth of deuterium nanocrystals in porous silicon. Studies on the dynamics in nanostructured matter are the third pillar this thesis rests on. Diverse topics are covered such as molecular diffusion in pore-confined liquids and phonon propagation in mesoporous silicon. Studies on the thermal transport in spark plasma sintered porous silicon culminate in a novel model for the thermal conductivity of structured, porous systems. The thesis closes with a list of the key publications that emerged from these fascinating studies.

Zusammenfassung

Diese Dissertation markiert den Höhepunkt zehnjähriger Forschungstätigkeit auf dem Gebiet porenbegrenzter und nanostrukturierter Materie. Sie beginnt mit einem umfassenden Überblick über untersuchte poröse Materialien sowie nanostrukturierte Oberflächen. Nanoskalige Benetzung ist das erste wissenschaftliche Kernthema der Dissertation. Röntgenstreutechniken in Kombination mit nanostrukturierten Substraten werden verwendet, um die erweiterte Young-Laplace-Gleichung auf Längenskalen von unter 10 Nanometern zu validieren. Die Kristallstruktur von nanoskaligen Festkörpern steht im Vordergrund des zweiten Kernthemas. Als Highlight belegen Studien mittels elastischer Neutronenstreuung das quasi-einkristalline Wachstum von Deuterium-Nanokristallen in porösem Silizium. Studien zur Dynamik in nanostrukturierter Materie sind die dritte Säule, auf der diese Arbeit ruht. Es werden verschiedenste Themen behandelt, wie molekulare Diffusion in porenbegrenzten Flüssigkeiten und Phononenausbreitung in mesoporösem Silizium. Untersuchungen zum Wärmetransport in gesintertem porösem Silizium führen zu einem neuartigen Modell für die Wärmeleitfähigkeit von strukturierten, porösen Systemen. Die Arbeit schließt mit einer Auflistung der wichtigsten Veröffentlichungen, die aus diesen faszinierenden Studien hervorgegangen sind.

Contents

Chapter 1

Introduction

Condensed matter behaves on nanometer-sized length scales fundamentally different than as macroscopic bulk system. As the system size is reduced, structure and dynamics are altered by geometric confinement, the increasing importance of surface and interface energies and finally by quantum effects.
It is natural that this modified behavior of soft and hard matter motivated numerous studies in the field of fundamental and applied science. At the forefront of these studies stands the common primary objective to understand and predict novel effects unknown in bulk matter and to transfer the gained insights into emerging, superior technologies.
Theoretical and experimental studies cover diverse research fields. To name only a few, there are studies on nanoelasticity [1–4], electronic and thermal transport on the nanoscale [5–8], structural phase behavior [9–11] and nanofluidics [12, 13]. Similar diverse are the studied systems. Nanowires, nanodots are just as interesting as pore-confined matter, nanostructured surfaces or nanocrystals [14–20].
Envisioned technological applications for nanostructured materials are obviously numerous. The design of energy materials that benefit from nanostructuring should be named here as particular active research field. Recent years saw the advent of novel emergent technologies for a green and sustainable energy infrastructure, which heavily rely on structuring on various length scales [21].
Nanoporous electrodes are considered for novel battery concepts [22]. Structuring organic photovoltaics on the nanometer scale is one prerequisite for efficient charge carrier harvesting [23, 24]. Contemporary catalysis and complementary fuel-cell technologies depend on nanostructured materials with huge surface-to-volume ratios and seek to overcome the dependence on expensive platinum [17, 25]. Ionic-liquid based supercapacitors need conductive nanoporous electrodes [26, 27]. Last but not least, thermoelectrics research considers nanostructuring as promising strategy for engineering electronic and thermal transport behavior [28–31].
This cumulative thesis focuses on fundamental questions concerning the behavior of matter on the nanoscale. After the introduction, four main chapters are at the core of this dissertation before a summary and outlook precede the bibliography and list of key publications [32–45].
Chapter 2 is titled *Nanostructured Materials*. It reviews the synthesis of mesoporous silicon, anodic aluminum oxide, SBA-15, carbide derived carbons, nanosculptured Si surfaces and spark plasma sintered silicon. It emphasizes the importance of these materials for the studies on nanostructured matter that are presented in the chapters that follow.
Nanoscale Wetting is the name of chapter 3. It discusses in detail theoretical models

to describe wetting on nanostructured substrates. X-ray scattering experiments put the validity of these models to the test. Further, the formation of nanobubbles in confined liquids is reported as peculiar wetting scenario in SBA-15.
Structure of Nanoconfined Matter is the topic of chapter 4. It focuses on the influence of nanoconfinement on crystal structure or liquid-solid and solid-solid phase transitions. The texture of nanoconfined, cryogenic solids is revealed by neutron diffraction. X-ray diffraction elucidates the morphology of nanoimprinted polymer films.
Dynamics in Nanoconfined Matter becomes forefront in the fifth and final chapter. The self-diffusion of organic liquids upon nanoconfinement is probed with quasi-elastic neutron spectroscopy. Similarly, inelastic neutron scattering experiments reveal the phonon dispersion in single-crystalline, mesoporous silicon. The chapter closes with a detailed study on heat transport (phonon transport) in sintered silicon.

Chapter 2

Nanostructured Materials

2.1 Porous Materials

I present in my thesis studies that utilize porous materials to probe the structure and dynamics of nanoscale matter. Although in part commercially available, all porous materials were synthesized within our project groups to guarantee full control over sample properties.
"Porous materials" stands hereinafter as generic term for microporous and mesoporous materials. Labeling materials with pore diameters $< 2\,\text{nm}$ as "microporous" and with pore diameters in the range from $2\,\text{nm}$ - $50\,\text{nm}$ as "mesoporous", follows the somehow counter-intuitive IUPAC classification [46].
Mesoporous silicon (pSi) is used in the thesis to study the crystallographic structure of nanoconfined deuterium and nitrogen, to elucidate stochastic motions in molecular liquids and to identify the influence of nanostructuring on lattice dynamics [34, 35, 38, 39]. The dynamics in ionic liquids upon confinement in porous carbide derived carbons (CDCs) is investigated by neutron scattering techniques [45].
Anodic aluminum oxide (AAO) is the host for nanoconfined oxygen in elastic neutron scattering experiments [36], whereas the formation of nanobubbles is observed in fluorinated pentane confined in mesoporous silica (SBA-15) [37]. Spark plasma sintered Si (SPS-(p)Si) is utilized to probe the effect of porosity and hierarchical structuring on thermal conductivity [41].

2.1.1 Porous Silicon

Crystalline silicon with nanometer-sized pores in the range from $1\,\text{nm}$ - $50\,\text{nm}$ is commonly referred to as micro- and mesoporous silicon [47]. Its first synthesis by means of electrochemical etching dates back to 1956 [48]. Twenty to thirty years later, its high internal surface was found to be useful for spectroscopic studies and for the synthesis of thick oxide layers on silicon or dielectric layers [49–52]. But it was in the nineties, that the interest in pSi, to use Sailor's words [53], exploded with the discovery of its photoluminescence properties [54, 55]. Since then, pSi found widespread applications in fundamental as well as applied science [13, 53, 56, 57].
Among its appealing properties are biocompatibility, tunable surface chemistry, huge pore-surface to pore-volume ratios, and controllable morphology. Further, its synthesis relies on an earth abundant, non-toxic and cheap source material [58, 59]. Because of this diversity, scientists and engineers propose pSi on a technological level for micro- and nanofluidic applications [60], novel electrodes for ion batteries [61, 62], solar cell technology [63, 64], on-chip heat management, thermoelectric elements

[30, 65], photonic and sensor applications [66–68] and to consider photoluminescence-based cancer markers [69, 70].
On a more fundamental level, pSi emerged in recent decades as versatile host material to study the effect of nanoconfinement on the structural and dynamic properties of condensed matter [13, 71–73]. For a detailed and comprehensive review of pSi and its role in fundamental and applied science, I refer the interested reader to references from Huber [13] and Sailor [53].
E-beam lithography [74, 75] (→ Sec. 2.2.2), polymer-template processing in combination with reactive ion etching [76, 77] (→ Sec. 2.2.1), metal assisted etching [78–80] and dry etching [81–83] are sophisticated, modern approaches to nanostructure silicon with exceptionally high control of pore and pitch sizes as well as pore arrangement. However, these methods are often limited to the synthesis of thin films, are time consuming, expensive and do not allow for scalable synthesis of macroscopic amounts of micro- and mesoporous silicon. Consequently, today electrochemical wet-etching of silicon in hydrofluoric acid [47, 53] appears still as an effective and competitive method.
A novel etching cell for small-scale pSi anodization is described in key publication [40]. It utilizes a vertical setup in which the silicon wafer, supported by an aluminum plate, serves as anode (→ Fig. 2.1) and an electrolyte resistant platinum wire as counter electrode. Both electrodes are immersed in the electrolyte and a double-walled containment for the electrolyte complies with highest safety standards. Except for a venting outlet, the etching cell is designed as closed system that prevents selective evaporation of the aqueous electrolytes and guarantees long-term stability of the etching conditions.
Lehmann and Gösele were the first to propose a three-step model for the electrochemical half-reactions at the anode upon etching [54] of p-doped silicon in hydrofluoric acid-based electrolytes. According to their model, holes (h^+) support in a first, electrochemical step the replacement of the hydrogen passivation at a [100] crystalline Si surface by a fluorine passivation (→ R 1). In the second, purely chemical step, silicon tetrafluoride is dissolved from the Si crystal and the dangling bonds in the crystal are again hydrogen terminated (→ R 2) before in the final step, the stable complex H_2SiF_6 forms in the electrolyte (→ R 3). The cathodic half-reaction is trivial and accounts only for the electrochemical proton oxidation.
Another crucial aspect in Lehmann and Gösele's description of pSi etching is the charge carrier (h^+) depletion in the walls between neighboring pores due to quantum size effects. It ultimately leads to the suppression of reaction path R 1 at the pore walls and therefore the lateral pore growth as etching at the pore bottom continues. The formation of "tubular" nanochannels along the [100] direction is in this sense a self-regulating process.

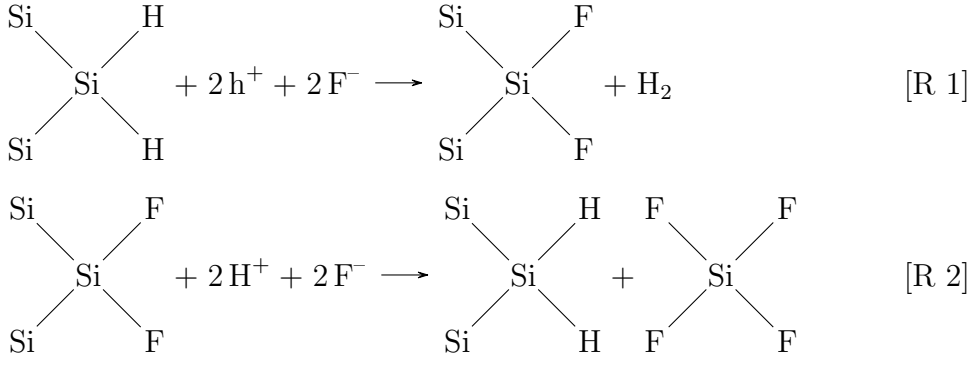

[R 1]

[R 2]

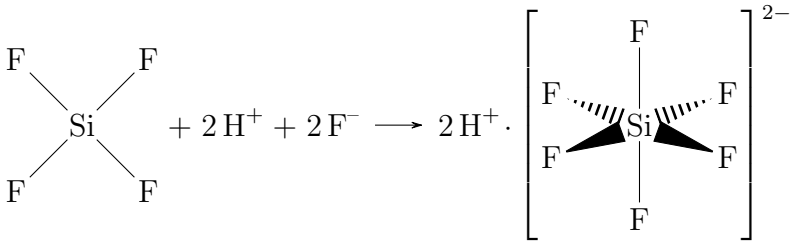

[R 3]

Zhang provides in his review [84] also a comprehensive account of the reaction pathways during etching that cause the formation of pSi. Furthermore, he details how the pore morphology is tuned by adjusting etching parameters like electrolyte concentration, anodization current and doping of the Si source material.

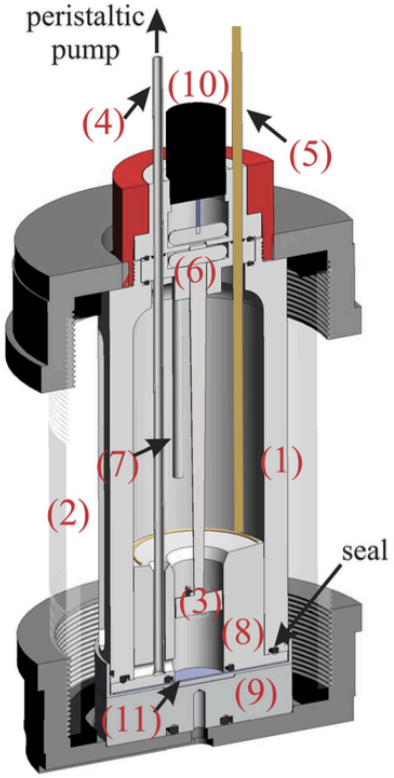

Figure 2.1: Anodization cell: (1) inner container, (2) outer container, (3) stirring bar, (4) Pt-tube, (5) Pt-cathode, (6) magnetic coupling, (7) venting, (8) high-current adapter, (9) Al-anode, (10) motor, and (11) Si wafer. Reprinted from Ref. [40], with the permission of AIP Publishing.

Figure 2.2 shows a scanning electron microscopy (SEM) image of a typical pSi sample, which is used for the studies of this thesis. The top view of the micrograph shows polygonal pores roughly 10 nm across. The side view exhibits the dendrite-like pore channels along a [100] direction of the single crystalline Si wafers, which were used as source material. The anodization of the respective sample utilizes an hydrofluoric acid (48 wt%) : ethanol (99 wt%) electrolyte in the volume ratio 4 : 6, a constant current density of $j = 13\,\mathrm{mA\,cm^{-2}}$ and a p-doped single crystalline [100] Si-wafer with a resistivity of $\rho = 0.01\,\Omega\,\mathrm{cm}$ - $0.02\,\Omega\,\mathrm{cm}$. An increased current density of $j = 215\,\mathrm{mA\,cm^{-2}}$ causes after a 4 h anodization a roughly 160 µm thick self-supporting pSi membrane to detach from the wafer after 40 s.

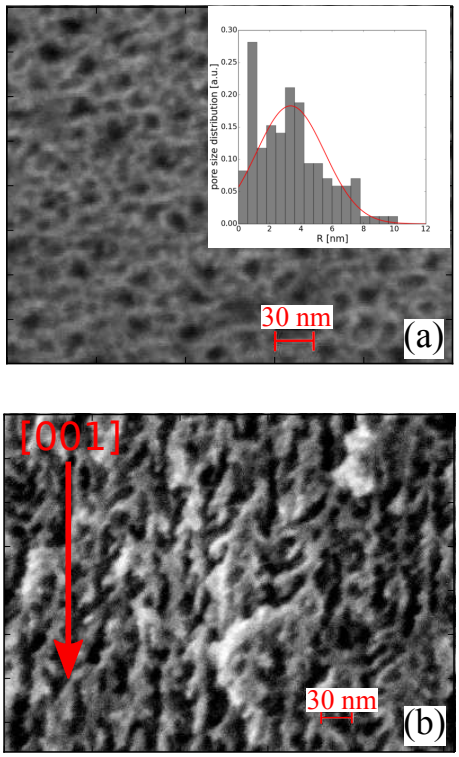

Figure 2.2: SEM micrograph of pSi recorded with a SEM LEO GEMENI microscope employing electron energies of 15 keV: (a) Top view of the pores in etched silicon. The inset illustrates the pore size distribution as inferred from a contrast analysis of the SEM image. (b) Side view of the pores. Reprinted with permission from Ref. [38]. Copyright 2017 Elsevier.

2.1.2 Anodic Aluminum Oxide

The next mesoporous material with a fairly long history to be introduced is anodic aluminum oxide. Whereas industrial anodization of metals dates back one century into the 1920's, the first detailed studies on AAO itself emerged in the 1950's [85]. Diggle, Downie, and Goulding [86] published 1969 a first comprehensive account reviewing its formation process. The next notable milestones are the 1981 work by Thompson and Wood [87], which broadened the understanding of AAO formation during anodization and the seminal work by Masuda and Fukuda [88] on self-ordered AAO structures in 1995.

AAO resembles in its pore morphology pSi. It as well covers a similar field of applications. Sensing applications benefit from the high tunability of optical properties [89, 90] and huge surface-to-volume ratios motivate drug delivery studies [91]. It finds widespread application as template to grow nanostructures such as nanowires [92]. Similar to pSi, it is a suited host material to investigate the properties of nanoconfined matter. I refer to the review article from Ruiz-Clavijo, Caballero-Calero, and Martín-González [90] for a detailed account on the fabrication and application of AAO.

Kojda et al. tailor in [36] an electrochemical anodization procedure [93, 94] to synthesize mesoporous AAO membranes with tubular pores in the 10 nm range. Polycrystalline aluminum foils (purity $> 99\,\%$) are anodized in sulfuric acid ($c = 10\,\mathrm{wt}\%$) at constant voltage $U = 7\,\mathrm{V}$ and constant electrolyte temperature $T = -2\,^{\circ}\mathrm{C}$ for

48 h. Hereby, the electrochemical reaction converts bulk aluminum in mesoporous anodic aluminum oxide [94, 95].
The specific anodization parameters cause the growth of a 15 µm - 20 µm thick amorphous AAO layer with 10 nm - 12 nm wide tubular nanochannels on top of residual aluminum as evidenced by sorption isotherms (→ Sec. 2.3.1 & [36]) and SEM microscopy (→ Fig. 2.3).
The SEM images in Fig. 2.3 show a representative membrane. The top view exhibits directly the pore openings with diameters in the stated range from 10 nm - 12 nm. Their lateral arrangement at the surface of the membrane appears mostly arbitrary. But occasionally six neighbors surround a pore in the center. This particular arrangement is a precursor of long-range hexagonal 2d-lattices, which evolve in a self-ordering process when larger pores are synthesized [88, 95]. The side-view exhibits segments of spatially separated, a few micrometers long tubular nanochannels parallel to the surface normal of a synthesized AAO layer.

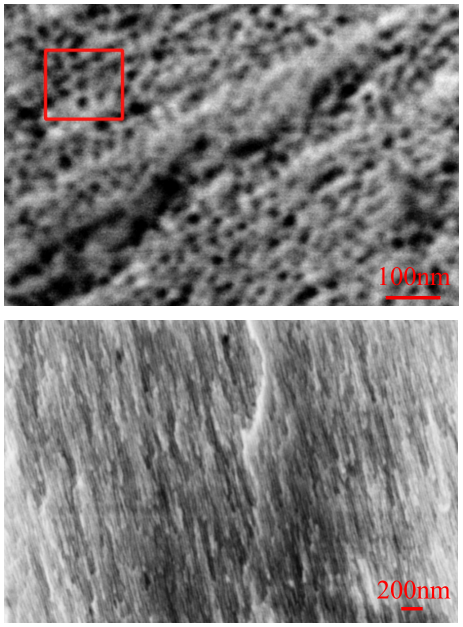

Figure 2.3: SEM images of AAO: Top-view of the pore openings, a rectangle marks a hexagonal arrangement of neighboring pores (top), side-view on tubular nanochannels in a cracked alumina membrane (bottom). Reprinted from Ref. [36], with the permission of AIP Publishing.

2.1.3 SBA-15

Porous silicates form an entire material class. Zeolites and Vycor® are well known examples [96–99]. The mesoporous silica SBA-15 is a more recent development. It was first synthesized in the 1990's at the Santa Barbara University of California, giving it its exotic, but not particularly inventive name "Santa Barbara Amorphous 15" [100].
SBA-15 is a template-grown, powdery silica matrix with tubular pores that are arranged by design on a hexagonal 2D lattice [100]. Its synthesis commonly encompasses three subprocesses: the polymer templating process, the sol-gel process and calcination. A multitude of different synthesis routes [100–102] allows tailoring pore diameters, pore-pore distances [100] or surface functionality [102] in powdery and

monolithic substrates [103].
In the sequence of subprocesses, the morphology of the initially formed polymer micelles molds the morphology of the final SBA-15 silica sample. As the shape of these micelles is not only determined by the attempt to screen hydrophobic polymer blocks in an aqueous solution, which results in regular spherical and cylindrical geometries, but rather is subject to thermally driven, hydrodynamic instabilities like the Rayleigh-Plateau instability, it can be expected that the final silica product reflects morphological artifacts of these instabilities (→ Fig. 3.5) [104–106].
The synthesis of our sample follows a standard recipe of Zhao et al. [100] to obtain a fine grained powder (1 µm) with tubular mesopores roughly 7 nm across and 11 nm apart. The templating process consists of dissolving 4 g of the micelles forming triblockcopolymer $EO_{20}PO_{70}EO_{20}$ at $T = 35\,^{\circ}C$ in 30 g water and 80 g of 2M hydrochloric acid. Subsequently, a sol-gel process is triggered by adding 8.8 g of tetra-ethyl-ortho-silicate as silica source to the solution and stirring for 20 h at constant temperature T. The solid deposit is recovered and dried after additional aging at 80 °C for 12 h. Calcination of the template polymers under oxygen atmosphere at 500 °C for 6 h leaves only the stable silica skeleton and concludes the SBA-15 synthesis.
Fig. 2.4 exhibits an SEM micrograph for a typical SBA-15 sample. The 2D hexagonal lattice of cylindrical pores is shown.

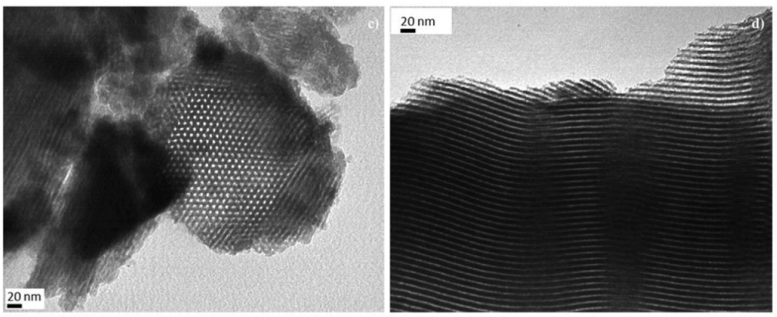

Figure 2.4: SEM micrograph of SBA 15: hexagonal arrangement of the pores (left), tubular pore channels (right). Reprinted from Ref. [107] under CC-BY-NC-ND.

2.1.4 Sintered Porous Silicon

Spark plasma sinterering (SPS) is an advanced and modern technology to synthesize macroscopic samples with an intrinsic micro- or nanostructure starting from powdery source materials. A first patent (Bloxam GB 9020) documents the origins of the technique already in 1906. But it was only at the end of the century that SPS apparatuses were produced on an industrial scale for wide spread applications in industry and science.
At the core of the SPS process is the welding of micrometer or nanometer sized grains at their interfaces in an highly compacted powder. For this purpose, at low voltages, a sufficiently high, pulsed DC current is applied to the specimen at elevated temperatures. The interested reader can consult the articles by Guillon et al. [108] and Nisar et al. [109] for excellent and more comprehensive reviews of the method including its historic background and its manifold applications.
The key publication [41] investigates the nanostructure, porosity and thermal con-

ductivity of SPS-pSi made from crushed pSi and SPS-Si made from commercially available silicon nanopowders both in combination with small amounts of nanostructured aluminum. The initial porosity of the used pSi samples is a defining parameter for the properties of the final SPS-pSi specimen. It can be controlled by the anodization parameters discussed in Sec. 2.1.1. The aluminum additive serves the sole purpose to reduce the melting point of the binary Si-Al eutectic [110].
All powders are compacted in a FCT HP D10-GB system (FCT Systeme GmbH). This closed system combines a SPS furnace with a glovebox. All powder preparation is performed in the absence of air or moisture in order to reduce surface oxides. Whereas the Si nanopowders for SPS-Si itself are bought oxygen free and only handled in the glove box, substantial efforts are required during the SPS-pSi synthesis to avoid oxide contamination of the source material.
Anodized pSi naturally oxidizes. The pSi specimens are therefore flushed with water, rinsed for 2 min in hydrofluoric acid to remove surface oxides and finally rinsed for 6 min in "dry" octane. The last octane bath containing the specimen is transferred into the glovebox of the SPS furnace to dry the pSi membrane in an inert N_2 atmosphere. Still in the glovebox, the membranes are powdered in an agate mortar and filled into graphite dies for sintering.
The samples are densified in vacuum at an uniaxial pressure of 34 MPa at 1273 K and 1473 K and with holding times of 5 min and 10 min. More details on the experimental conditions are summarized in Table S1 of the supplementary information to Ref [41] available online.
The SEM micrographs in Fig. 2.5 exhibit the microstructure of various SPS-pSi samples. The figure indicates also the finite porosities of the final specimens Φ that justify retroactively the characterization of SPS-pSi as porous material. A residual porosity in SPS samples is generally expected after the powder densification but is certainly enhanced when a highly porous source material (pSi) is used.

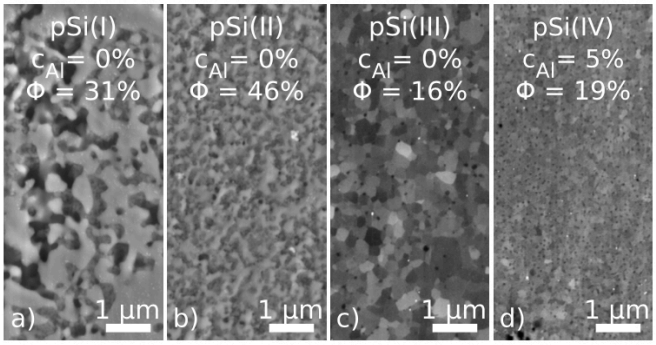

Figure 2.5: SEM micrographs of pSi based samples processed at 1473 K. The microstructure is mainly determined by the initial porosity that is 70%, 53%, 84% and 79% for pSi(I) to pSi(IV). Φ denotes the porosity of the final specimen, c_{Al} the aluminum content during synthesis. Reprinted from Ref. [41] under CC-BY.

2.1.5 Carbide Derived Carbons

Carbide derived carbons (CDCs) are the last class of porous materials that I introduce in this section. The synthesis idea in a nutshell is to remove in metallic precursors, that are the carbides, the metal atoms via etching or hydrothermal cor-

rosion to retain a porous carbon skeleton. Already in 1918, Hutchins patented the chlorine etching of silicon carbide to produce $SiCl_4$. However, porous carbon as a by-product was treated as useless waste material, until in the mid of the century an interest in its properties emerged [111]. It followed for several decades research activities that focused mainly on developing different synthesis routes for CDCs [112–115].
The contemporary interest in CDCs finds its explanation in their potential as advanced functional nanomaterials [26, 116–120]. CDCs excel in tunability of pore size, shape, and surface chemistry. They possess a high electrical conductivity, good (electro)chemical stability, and a large specific surface area, making them interesting candidates for nanostructured electrodes [121].
Silicon carbide (SiC), molybdenum carbide (Mo_2C), and boron carbide (B_4C) microparticles (1 µm - 5 µm wide) are the precursors for the CDCs used in study [45]. They are etched with Cl_2 gas at elevated temperatures T to remove the metal atoms and subsequently annealed in H_2 gas at 600 °C. Additional oxidation and annealing steps help defining the pore size distribution (PSD) and surface functionality.
SiC precursors are etched at $T = 1000$ °C. After the H_2 annealing, they are oxidized in air at 425 °C. A last annealing in high vacuum (10^{-6} Torr) at 1400 °C produces the final specimen subsequently referred to as 'SiC-2'. Mo_2C precursors are etched at slightly lower temperature $T = 900$ °C. Otherwise the 'MoC-15' samples are synthesized under identical conditions than 'SiC-2'. 'BC-6' are B_4C based CDCs, which are synthesized like 'MoC-15'. In contrast, 'BC-6-no' samples are not oxidized. As the final annealing step removes surface functional groups, the surfaces of all synthesized CDCs are chemically identical [118, 122] independent of the used precursor.

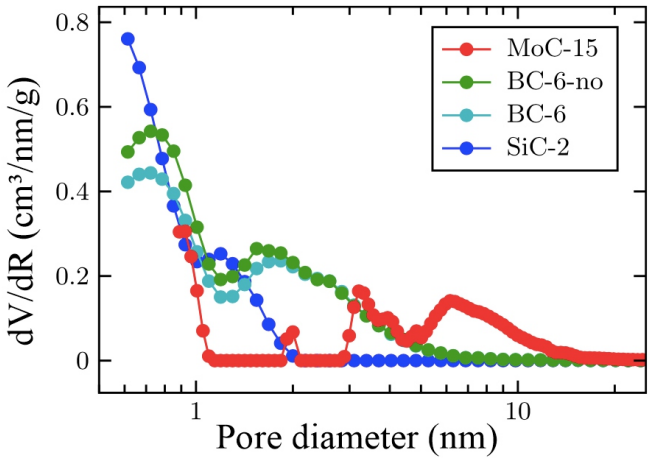

Figure 2.6: Pore size distributions of CDCs. Reprinted from Ref. [45] under CCA 4.0 International.

Fig. 2.6 shows the PSDs for the various CDCs as derived from volumetric N_2 sorption isotherms (→ Sec. 2.3.1). These isotherms measure the uptake of liquid nitrogen in the pore space at $T = 77$ K as the pressure of the coexisting gas phase is changed. The pressure dependent uptake of liquid in combination with a geometric model for the pores allows inferring pore sizes, porosity and specific surfaces of the specimen. The presented analysis of the PSDs relies on a density functional approach [123]

(→ Sec. 2.3.1). It evidences that all samples are polydisperse. The CDCs contain micropores as well as mesopores.

2.2 Nanosculptured Si Surfaces

Some experiments on nanoscale matter necessitate better defined substrates as generally provided by anodization or sintering techniques. Nanowetting experiments in particular demand often nanostructures with highly regular morphologies and well characterized, quasi-monodisperse features that facilitate a comparison with theory. The studies [33] and [42] utilize nanosculptured Si substrates for probing concepts of nanowetting. The term "nanosculptured Si" refers to a flat silicon substrate with nanometer-sized structural features in a shallow surface layer. Members of the project team synthesize these substrates by a combination of polymer templating and reactive ion etching.

2.2.1 Self-Assembled Polymers & Reactive Ion Etching

Block copolymer self-assembly-based fabrication approaches [124] facilitate the synthesis of nanostructured surfaces with properties suitable for studying nanobubble formation at a liquid/solid interface (→ [42]). Block copolymer thin films form autonomously well-defined, periodic patterns of nanometer-scale features. Nanometer-sized domains ($< 20\,\mathrm{nm}$) with high density ($\approx 1011\,\mathrm{cm}^{-2}$) develop in a microphase separation process that is driven by free energy minimization [124]. The last statement is equivalent to saying that the blocks in the copolymer phase separate because they are not inter-mixable.
Intrinsic polymer properties such as the molecular weight (Mw) and the relative volume fractions (f) of the polymer blocks in the copolymer determine the equilibrium pattern dimensions. Thin films of an asymmetric poly(styrene)-b-poly(methyl methacrylate) (PS-b-PMMA) diblock copolymer ($Mw = 67\,\mathrm{kg/mol}$; $f(PS) = 0.7$) phase separate into hexagonally arranged PMMA domains with $\approx 20\,\mathrm{nm}$ diameter and $\approx 40\,\mathrm{nm}$ nearest-neighbor separation and an embedding PS matrix upon annealing at 180 °C for 2 h. Exposure to ultraviolet light degrades the PMMA block and facilitates its removal in acetic acid to obtain a porous PS template.
Nanostructured surfaces are prepared from such porous self-assembled templates on Si substrates using either SF_6-based or a HBr-based plasma etching, followed by an O_2 plasma etch to remove any residual polymer from the Si surface. The anisotropic plasma etching preferentially removes silicon from the pore bottoms. The resulting structured silicon surfaces contain hexagonally packed nanocavities as deep as 165 nm (→ Fig. 2.7) with average diameters only slightly wider than the initial polymer template $w = 28(2)\,\mathrm{nm}$. The nanocavity cross sections are approximately parabolic, independent of their depth. A significant advantage of this fabrication technique is that the nanocavity depth can be controlled by the etching time.

2.2.2 E-beam Lithography & Reactive Ion Etching

The aforementioned templating by means of self-assembled block copolymers intrigues by its simplicity. But it relies on several constraints. One must find the "correct" copolymer with the adequate intrinsic properties, a polymer that microphase

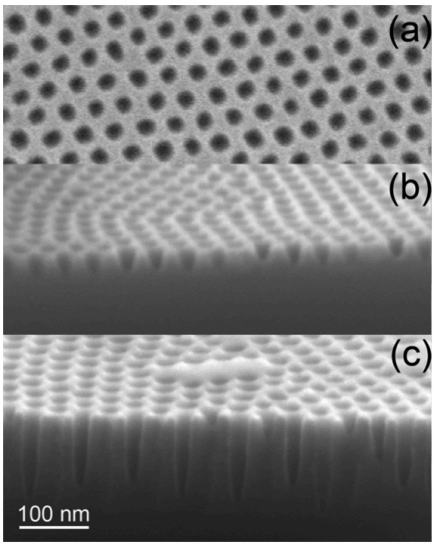

Figure 2.7: Scanning electron microscopy pictures of silicon surfaces patterned with a hexagonal array of nanocavities with an average diameter $w = 28(2)$ nm and various depths: (a) top-view and (b) side-view image of 34 nm deep cavities. (c) Side view of 140 nm deep cavities (the lateral scale is the same for all pictures). Reprinted with permission from Ref. [42]. Copyright 2010 American Chemical Society.

separates and whose blocks react selectively on UV exposure. In this sense, templating via e-beam lithography might be considered as being more flexible although also technologically more demanding and more expensive. Subsequent paragraphs outline the synthesis of nanosculptured Si surfaces by means of combined e-beam lithography and reactive ion etching ($\rightarrow$ [32]). Synthesized samples are used for wetting studies in key publication [33].

In the first step, Si wafers (0.5 mm thick) are spin coated with 60 nm of ZEPA resist from Zeon Chemical. E-beam lithography utilizing a Vistec VB6 instrument at 100 kV is used to write arrays of lines (pitch 45 nm) and arrays of dots (pitch 40 nm) covering an area as large as 1 mm^{-2}.

After writing the pattern, the polymer resist is developed at 3 °C under ultrasonic agitation for 30 s, rinsed in isopropanol, and dried with nitrogen. The second step leaves the silicon covered with an initial polymer template.

The samples are now coated with 10 nm of chromium and the polymer patterns are lifted off using a solvent along with ultrasonic agitation. It leaves a Cr template on the Si substrate, which is the negative image of the initial polymer template.

The samples undergo subsequently inductively coupled plasma-reactive ion etching (ICP-RIE) with CF_4 at a 4 mTorr pressure and a 175 V platen bias. Etching occurs preferentially at unprotected Si-surfaces. Finally, the Cr template is removed with a commercial Cr etch (Cr-9S) and rinsed well with deionized water. The cleaning of the samples with a high density O_2 plasma concludes the synthesis.

The SEM micrograph in Fig. 2.8 exhibits the array of truncated Si cones on a Si substrate. It shows exemplarily the strength of e-beam lithography to synthesize Si nanostructures with an high degree of geometric regularity.

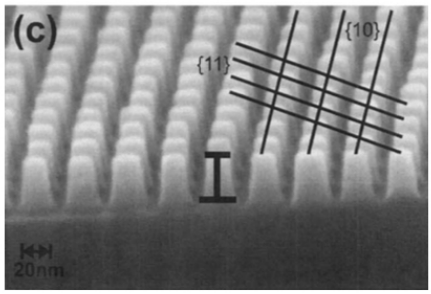

Figure 2.8: 40 nm period array of truncated Si cones: The {10} and {11} planes are shown. Reprinted with permission from Ref. [32]. Copyright 2009 American Vacuum Society.

2.3 Characterization of Morphology

I want to conclude this chapter with a brief overview of characterization techniques for nanostructured materials. In the preceding sections mostly SEM micrographs were shown to appealingly visualize the various materials. Here is however not the place to give an introduction into scanning electron microscopy as a widely known technique.
Rather, it appears as more important to discuss sorption isotherms and grazing incidence X-ray diffraction as characterization tools because both provide invaluable information about the porous and nanosculptured samples that are in the focus of my main studies.

2.3.1 Sorption Isotherms

Sorption isotherms are an important tool to measure the PSD, porosity and specific surface of micro- and mesoporous materials [123]. They determine at $T = 77\,\mathrm{K}$ volumetrically the uptake $f = N/N_0$ of liquid nitrogen in the porous host as the pressure $P_{red} = P/P_0$ of the coexisting gas phase is varied. Here, N and N_0 refer to the number of molecules physisorbed and required to fill the pore space completely. P_0 is the saturation pressure of liquid N_2 at 77 K, P is the vapor pressure of the condensed phase.
Fig. 2.9 shows an adsorption-desorption isotherm measured on pSi. At low pressures ($P_{red} \lesssim 0.65$) a liquid film forms on the pore walls, the pore center remains empty. At higher pressures ($P_{red} \gtrsim 0.65$) a capillary condensate forms in the pore center. This regime is characterized by a pronounced adsorption-desorption hysteresis [125–127].
Various analytical tools are available to analyze the isotherms. The BET-method named after Brunauer, Emmett, and Teller [128] interprets the initial part of the isotherm ($0.1 \lesssim P_{red} \lesssim 0.35$ in Fig. 2.9) as the multilayer growth of a liquid film on a flat substrate. This approach allows inferring a specific surface for the porous materials. In highly porous materials, values as large as $\approx 1000\,\mathrm{m^2\,g^{-1}}$ are observed. The specific surface of the shown pSi is with $\approx 160\,\mathrm{m^2\,g^{-1}}$ smaller.
Barrett, Joyner, and Halenda [129] developed an algorithm to extract the PSD from the isotherms' desorption branch at higher pressures in the capillary condensation regime ($P_{red} \gtrsim 0.65$ in Fig. 2.9). It relies on the Kelvin Eq. (2.1) (→ Sec. 3.1) that relates the relative vapor pressure P_{red} to the mean curvature $\varkappa$ of a liquid-vapor

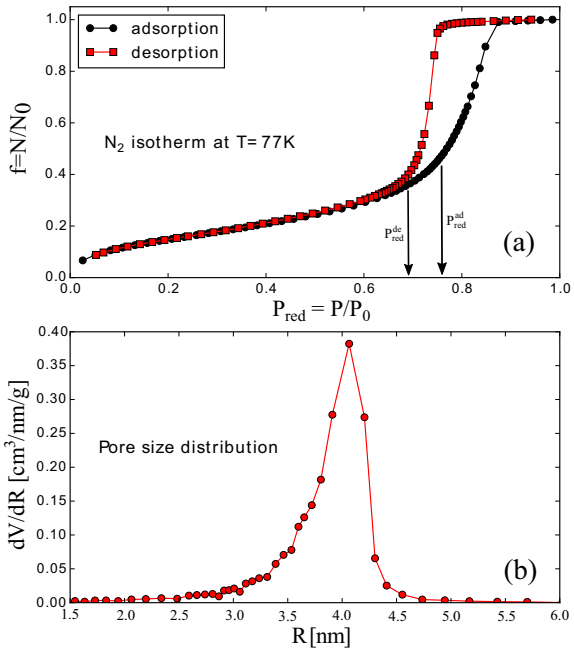

Figure 2.9: (a) N_2 sorption isotherm measured at $T = 77\,\mathrm{K}$ in pSi. (b) PSD in pSi estimated from the desorption branch of the N_2 isotherm applying a BJH-analysis. Reprinted with permission from Ref. [38]. Copyright 2017 Elsevier.

interface depending on the interfacial energy γ_{lv} and the liquid volume per molecule v.

$$k_B T \ln(P_{red}) = 2\gamma_{lv} v \varkappa \tag{2.1}$$

The BJH-algorithm applied to tubular pores assumes in the capillary condensation regime of the isotherm $f(P_{red})$ the existence of a hemispherical meniscus in the pore center. Its radius is identified with the pore radius R itself corrected by the thickness t of a coexisting liquid film on the pore wall. Hence, Eq. (2.1) combined with a model for $t(P_{red})$ [123, 130–132] allows a reparametrization of the isotherm $f(R)$ using $\varkappa = -(R-t)^{-1}$, and a PSD is inferred as the R-derivative of the accumulated pore volume that is $dV/dR \propto df(R)/dR$.[†] Fig. 2.9 shows next to the isotherm the specific (mass-normalized) PSD for a pSi sample. It is obviously mono-modal and more "well-behaved" around its mean value of $R = 4\,\mathrm{nm}$ than the ones encountered for CDCs in Fig. 2.6.

The BJH analysis implies an ensemble of independent pores, hemispherical menisci and ignores mostly the long-range liquid-substrate interactions. For the characterization of mesoporous materials, it seems to be generally agreed to accept these assumptions, an issue, which I shall comment on at the end of Sec. 3.1. For microporous materials, the liquid-substrate interactions definitely necessitate a different approach.

The BJH-algorithm is in some sense a macroscopic approach that is contrasted by microscopic treatments that account in detail for liquid-liquid and liquid-substrate interactions. A prominent example is the density functional approach [123]. It determines the equilibrium density profile of the condensed phase in the pores by

[†]The expression "pore volume distribution" would be more appropriate as we infer from the BJH-algorithm how the total volume distributes over differently sized pores and not the number density of pores with a particular radius.

minimizing the grand potential of the substrate in equilibrium with the liquid (→ Sec. 3.1). Such calculation can provide PSD's if the interaction parameters are known, a particular pore geometry and pore ensemble are assumed (typically independent, cylindrical or slit pores). The appearance of micropores in CDCs justifies retrospectively the analysis of the PSD's in the framework of the density functional theory (→ Sec. 2.1.5).
Finally, I want to emphasize that isotherms can be measured utilizing different cryogenic liquids. N_2 isotherms are often used to characterize porous materials because of obvious practical reasons. But circumstances can arise that lead to a different choice of adsorbate. Microporous samples might for instance require to use liquids with smaller molecule size to guarantee pore access.

2.3.2 Grazing Incidence X-ray Scattering

Grazing incidence small and wide angle X-ray scattering (GISAXS/GIWAXS) are powerful tools to characterize nanostructured surfaces and interfaces [133, 134]. Fig. 2.10 illustrates the GISAXS/GIWAXS scattering geometry utilizing a polymer line grating as thesis relevant example. The strength of the technique arises from the small incidence angle α of the X-rays, which is usually close to the critical angle of the substrate material ($\alpha_{crit} = 0.224°$ for silicon at 8 keV X-rays), and the possibility to probe the scattering signal in a plane perpendicular to the substrate surface.

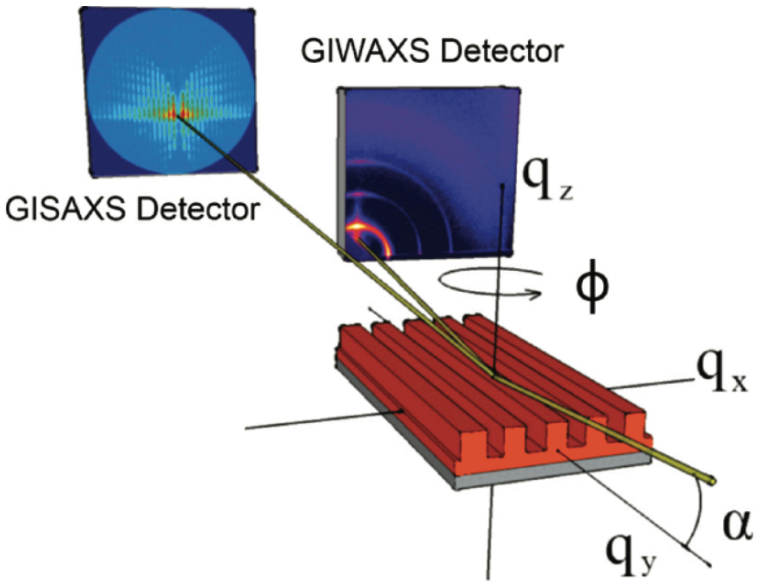

Figure 2.10: Geometry of GISAXS/GIWAXS measurements. The GISAXS detector shows the scattering signal from a line grating imprinted into a polymer film. The GIWAXS detector exhibits the crystallinity of a nanoimprinted polymer film. A reference system is shown for wavevector transfers perpendicular to the film surface (q_z) and in-plane (q_x, q_y). The polar angle Φ measures the sample rotation around its normal. Reprinted with permission from Ref. [44]. Copyright 2010 American Chemical Society.

The scattering signal, recorded ideally with a position sensitive 2D detector, contains information about the in- and out-of-plane structure of the probed specimen.

The small incidence angle renders GISAXS/GIWAXS into a highly surface sensitive technique suited for nanostructure characterization because it controls the X-ray penetration depth and constrains the X-ray wave propagation to a shallow surface region. This constraint is less a consequence of X-ray absorption (in particular at higher X-ray energies) but rather of waveguiding and refraction effects that dominate close to the critical angle and increase the effective scattering volume close to the surface [134]. A large surface illumination (beam projection) upon grazing incidence increases the surface sensitivity further.
The extraction of structural information from the scattering signal poses a formidable task. Grazing incidence diffraction can generally not be treated within the Born approximation typically used for diffraction data analysis [135]. Dynamical scattering theory in form of the Distorted Wave Born approximation (DWBA) must be employed [133] to properly account for X-ray reflection at interfaces and refraction effects.

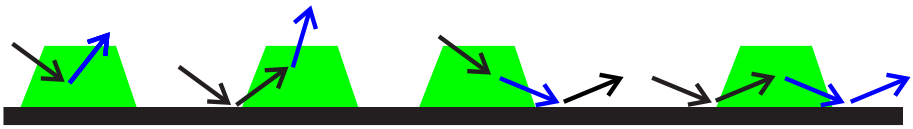

Figure 2.11: Scattering from a nanoisland on a substrate in the DWBA. From left to right: Born scattering, reflection prior to scattering, reflection post scattering, reflection prior to and post scattering.

Fig. 2.11 gives a flavor of the DWBA's complexity. It shows the different scattering events possible for a single nanoisland on a substrate. The first event presents the usual Born approximation. The three additional ones are corrections within the DWBA that account for reflections on the substrate prior to and post scattering. It becomes evident that the effective form factor of the island does not depend only on the wavevector transfer $\vec{q}$ that is the difference between incident and scattered wavevector ($\vec{k}_i$, $\vec{k}_f$) rather it depends on both individually [136]. Only for incidence and scattering angles α and 2Θ significantly larger than the substrate's critical angle, the corrections are ignored and the well-known form factor as Fourier transform of the island's electron density distribution is recovered.
Further complications arise for an ensemble of densely packed islands because refraction effects for X-rays cannot be ignored in such a case. The DWBA effective form factor for one island writes then in its full glory as

$$\begin{aligned} F(\vec{q}_\parallel, k_{iz}, k_{fz}) = & \int d\vec{r}_\parallel \exp(i\vec{q}_\parallel \vec{r}_\parallel) \int dz S(\vec{r}_\parallel, z) \\ & \times\{A^-[k_{iz}(z)]A^-[-k_{fz}(z)]\exp(i[+k_{fz}(z) - k_{iz}(z)]) \\ & +A^+[k_{iz}(z)]A^-[-k_{fz}(z)]\exp(i[+k_{fz}(z) + k_{iz}(z)]) \\ & +A^-[k_{iz}(z)]A^+[-k_{fz}(z)]\exp(i[-k_{fz}(z) - k_{iz}(z)]) \\ & +A^+[k_{iz}(z)]A^+[-k_{fz}(z)]\exp(i[-k_{fz}(z) + k_{iz}(z)])\}. \end{aligned} \tag{2.2}$$

As solutions to the Helmholtz propagation equation [137], A^+ and A^- are the z-dependent electric field amplitudes of upwards and downwards propagating waves in a graded interface [138], which derives from laterally averaging the refraction index $\overline{n}(z)$ in the layer of islands. The wavevector transfer ($\vec{q}_\parallel$, q_z) and the wavevectors ($\vec{k}_{i(f)\parallel}$, $k_{i(f)z}$) of incident (i) and scattered (f) X-rays refer to in- and out-of-plane

coordinates ($\vec{r}_\parallel$, z) with respect to the substrate [133]. The $z-$dependence of the wavevectors reflects the $z-$variation of the refraction index. $S(\vec{r}_\parallel, z)$ is the geometric shape function that takes the value one inside the island and zero outside.
Publication [32] is part of the efforts to establish the challenging DWBA analysis for the characterization of nanostructured surfaces and interfaces. Fig. 2.12 shows the GISAXS scattering signal from the truncated cones that were presented in Fig. 2.8. An analysis using Eq. (2.2) in the framework of the DWBA allows inferring for instance the inclination of the truncated cones. The quantitative GISAXS characterization of an e-beam written line grating ($\rightarrow$ Fig. 3.2) is essential for the wetting studies in 3.1 and publication [33]. Sec. 4.3 and Ref. [44] present a thorough GISAXS/GIWAXS study on the morphology of a nanoimprinted polymer thin film.

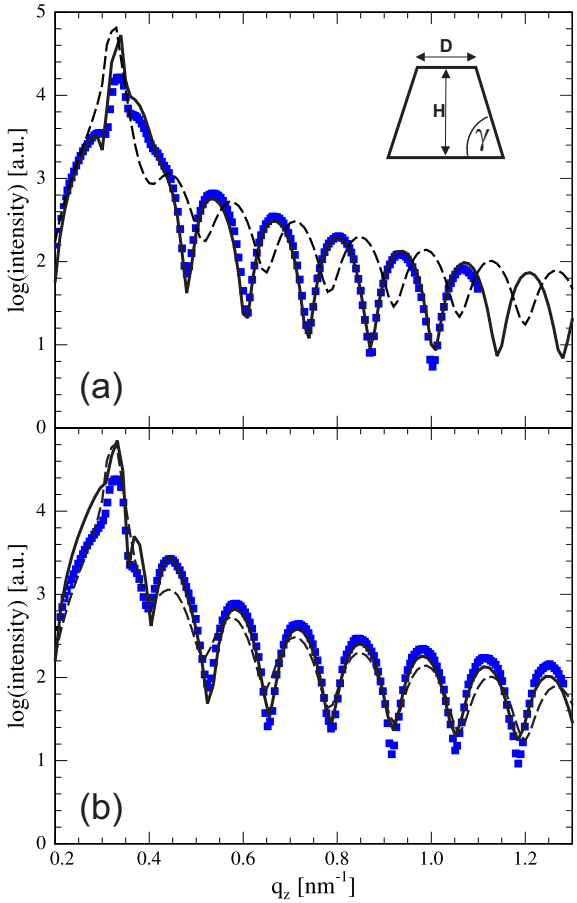

Figure 2.12: Truncated cones: The symbols show the scattering intensity along the (10) and (11) Bragg rods. The data have been fitted (black lines) in the framework of the DWBA using a truncated cone (inset). The dashed lines show a simultaneous fit of the (10) and (11) Bragg rods assuming $\gamma = 90°$. Reprinted with permission from Ref. [32]. Copyright 2009 American Vacuum Society.

As final remark, GISAXS and GIWAXS are by no means trivial scattering techniques. The quantitative data analysis is fairly imposing. It is remarkable, unfortunate but also understandable how many studies employ the technique on a merely qualitative level. Grazing incidence experiments demand further brilliant X-ray sources and a high degree of instrumental precision. Even in the age of next generation lab sources (liquid metal sources), synchrotron-based instruments are the

norm. The reader might want to study the article from Renaud, Lazzari, and Leroy [134] for an overly comprehensive review on grazing incidence scattering techniques, applications and analysis.

Chapter 3

Nanoscale Wetting

3.1 Young-Laplace Equation on the Nanoscale

3.1.1 Macroscopic Wetting: Basics

Two equations describe how a macroscopic amount of liquid V_l wets an ideal solid surface that is rigid, smooth and chemically homogeneous ($\rightarrow$ Fig. 3.1). These are the Young-Laplace Eq. (3.1) and the Young Eq. (3.2).

$$\Delta p = 2\gamma_{lv}\varkappa \tag{3.1}$$

$$\gamma_{sv} = \gamma_{sl} + \gamma_{lv}\cos\Theta \tag{3.2}$$

The Young-Laplace equation is a nonlinear partial differential equation for the liquid vapor interface $l(x, y)$ that describes the pressure difference across the interface depending on its mean curvature $\varkappa$. For a flat substrate, the parametrized interface $l(x, y)$ refers to the height of the liquid above the substrate surface at the two dimensional coordinate (x, y) ($\rightarrow$ Fig. 3.1)
Young's equation states that the contact angle Θ of a liquid on an ideal substrate depends solely on the interfacial energies γ_{sl}, γ_{lv}, and γ_{sv} of the boundaries between solid (s), liquid (l) and vapor (v) phase. Depending on the contact angle, one distinguishes three wetting situations. That are complete, partial, and non-wetting ($\Theta = 0°$, $0° < \Theta < 180°$, $\Theta \geq 180°$).
Eqs. (3.1) and (3.2) derive most eloquently from minimizing a free energy functional $H[\{l(x, y)\}]$ for $l(x, y)$ under the constraint of constant liquid volume $\int dxdyl(x, y) = V_l$. In the absence of gravity, it is for a flat substrate

$$H[\{l(x, y)\}] = \int dxdy\Big(\gamma_{lv}\sqrt{1 + \nabla l^2} + (\gamma_{sl} - \gamma_{sv})\Big) \tag{3.3}$$

with the operator $\nabla = (\partial_x, \partial_y)$. The first term in the integrand gives the energy of the curved liquid-vapor interface. The energies of the planar solid-vapor and solid-liquid interfaces compete in the second term.
One finds more details about the variational treatment of Eq. (3.3) in Refs. [139, 140]. In particular, Collins and Cooke [139] show that Δp takes the role of a Lagrange multiplier and that Eq. (3.2) does neither demand a globally flat substrate nor the absence of gravity, which were both assumed for the sake of simplicity.
First modifications of Eq. (3.2) arise for rough or heterogeneous surfaces [141]. The Wenzel model [142, 143] distinguishes between apparent and real contact areas of liquid and substrate on a rough surface. The Cassie-Baxter model [144, 145] accounts for fractional contact areas between liquid and chemically different surface regions.

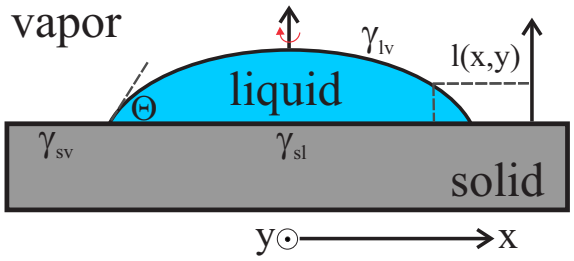

Figure 3.1: Partial wetting of a liquid (blue) on an ideal substrate (gray). θ is the contact angle of the liquid on the solid. $l(x, y)$ is the liquid height above the substrate. The liquid drop has a rotational symmetry around the surface normal on a homogeneous substrate.

3.1.2 Nanoscale Wetting: Theory

A more rigorous approach to describe wetting is required when the system size is reduced to nanometer sized length scales and only tens of nanometer thick liquid films on structured substrates are the object of interest. It becomes important to carefully consider the surface morphology, long-range liquid-solid and liquid-liquid interactions [146] that affect $l(x, y)$.
Long-range molecular interactions are the induction force, the orientation force and the dispersion force [146]. They are collectively known as van der Waals forces and all the interaction energies share the famous $1/r^6$ dependence. The dispersion force is nothing else than the infamous fluctuation induced dipole interaction. It usually dominates over other van der Waals forces except in highly polar systems like water. It is a proposition to replace Eq. (3.3) on the nanoscale with the grand canonical density functional for a non-uniform classical fluid [147, 148]

$$\Omega[\{l(x,y)\}] = \int dxdy\Big(\gamma_{lv}\sqrt{1+\nabla l^2} + \Delta\mu\Delta\rho l + W(x,y,l)\Big). \tag{3.4}$$

$\Delta\mu$ is the difference in chemical potential between bulk liquid-vapor coexistence $\mu_0(T)$ and physisorbed liquid on the solid substrate. $\Delta\rho = \rho_l - \rho_v$ is the particle density difference between liquid and gas phase. The effective interface potential $W(x, y, l)$ ($[W] = \mathrm{J\,m^{-2}}$) accounts for liquid-liquid and liquid-substrate interactions [33, 148, 149].
The liquid-vapor interface $l(x, y)$ is determined from the variational condition

$$\delta\Omega[\{l(x,y)\}]/\delta l(x,y) = 0 \tag{3.5}$$

for an extremal functional in thermal equilibrium. It is $\delta/\delta l$ the variational derivative and one obtains by means of the Euler-Lagrange equation [139, 150] the Augmented Young-Laplace equation (AYE)

$$2\gamma_{lv}\varkappa(x,y) + \Delta\mu\Delta\rho + \frac{dW(x,y,l)}{dl} = 0 \tag{3.6}$$

as equivalent to Eq. (3.5). $\varkappa(x, y)$ represents again the mean curvature of the liquid-vapor interface $l(x, y)$. $dW(x, y)/dl$ is known as disjoining pressure [141].
Eq. (3.6) takes an interesting form if one considers physisorption of liquid films

($\Theta = 0°$) in cylindrical cavities with radius R. With the pressure of the coexisting vapor-phase P and the bulk saturation vapor pressure P_0 it is

$$\Delta\mu = -k_B T \ln(P/P_0) > 0 \tag{3.7}$$

and one writes in appropriate coordinates

$$\Delta\rho k_B T \ln(P/P_0) = -\frac{\gamma_{lv}}{(R-l)} + \frac{dW(l)}{dl} \tag{3.8}$$

with l being the liquid film thickness on the pore wall.
This is a modification of the macroscopic Kelvin equation for the saturation vapor pressure over a curved liquid-vapor interface [151]. Saam and Cole [127] use Eq. (3.8) to explain hysteretic adsorption and desorption in cylindrical pores because it accounts properly for a potential energy $U(l) = dW/dl\Delta\rho^{-1}$ between liquid and substrate.
The Kelvin Eq. (2.1) that was introduced in Sec. 2.3.1 for the BJH-analysis looks slightly different than Eq. (3.8). The reason is that it ignores the disjoining pressure and refers to a hemispherical liquid-vapor interface contrary to the here assumed cylindrical liquid film on the pore walls.
There is another limit of Eq. (3.6) that should be mentioned: the case of a flat substrate ($\varkappa \to 0$). It is elementary that for dispersion forces the effective potential W of a flat film on a flat substrate scales with l^{-2} [141, 146]. It is therefore

$$\Delta\mu = \frac{A}{6\pi\Delta\rho l^3} \tag{3.9}$$

a prediction for the growth of flat liquid films. It is easily verified by experiments and allows extracting interaction parameters relevant for the description of wetting in more complex morphologies ($\to$ [33]). Eq. (3.9) introduces the effective Hamaker constant A [146].
I want to finish this section with a discussion of a simplified but appealing approach to the AYE. A geometric treatment of the AYE, which ignores long-range interaction can be easily devised for not overly complex substrate geometries like trapezoidal groves. Following Rascón and Parry [152], the shape of the liquid-vapor interface for wetted groves can be constructed in a two step process. Initially, the grooves are covered with a liquid film of thickness $t \propto \Delta T^{-1/3} \propto \Delta\mu^{-1/3}$ as one would expect for a flat substrate ($\to$ Eq. (3.9)). Then, a cylinder with radius R given by the conventional Kelvin equation $R = \gamma_{lv}/(\Delta\rho\Delta\mu)$ is fitted (if possible) to the coated surface. Coated surface plus meniscus (if any) define hereafter the liquid vapor interface. The tangential points are taken as the edges of the meniscus, whose shape is the lower part of the cylinder.
The geometric approach to wetting appeals through its simplicity. It allows intriguingly visualizing different wetting regimes ($\to$ Fig. 3.3). The grooves are coated with a thin liquid film in the prefilling regime before filling occurs via capillary condensation, that is the formation of a convex meniscus in the groove center. Postfilling is observed after the meniscus reaches the surface of the sculptured substrate upon subsequent filling. One should however state that such an appealing visualization of wetting cannot be transferred easily to more complex geometries.

3.1.3 Nanoscale Wetting: Experiment

The approach to nanoscale wetting that was just put forward requires of course stringent experimental verification. Ref. [33] details scattering experiments that validate Eqs. (3.4), (3.5), and (3.6) on the 10 nm scale. The conceptual idea relies on analyzing the X-ray scattering intensity from an e-beam written Si surface with a periodic array (spacing $a = 45$ nm) of nanometer sized groves (depth $H = 39.4$ nm, width $D(H/2) = 16$ nm, inclination $\alpha = 80(2)^\circ$, $\rightarrow$ Fig. 3.2) upon gradually filling with liquid perfluoromethylcyclohexane (PFMC).
The thermodynamic control of the wetting process is fairly simple. The nanosculptured Si substrate and a bulk liquid reservoir of PFMC are hermetically sealed in a sample cell with X-ray transparent windows to perform the scattering experiments. Substrate and liquid are spatially separated and only "connected" via the shared vapor phase. The liquid is kept at constant temperature T_0 and the variable temperature $T_0 + \Delta T$ of the substrate allows controlling the chemical potential

$$\Delta\mu = \frac{L}{T_0}\Delta T \tag{3.10}$$

of the physisorbed liquid with respect to the bulk phase and as $\Delta\mu$ approaches zero in the experiment more and more liquid condenses on the nanostructured substrate. Eq. (3.10) with the latent heat per molecule L is easily derived from Eq. (3.7) in conjunction with the Clausius-Clapeyron equation [151].
The gradual wetting is observed in-situ by X-ray diffraction. The periodic arrangement of trapezoidal grooves causes in a transmission X-ray scattering experiment (incident X-rays $\parallel$ substrate normal) well-defined Bragg reflections at wavevector transfers $q_x = n2\pi/a$ with $n = 1,\ 2,\ 3, \ldots$ ($\rightarrow$ Fig. 3.2). The intensity $I(q_x, \Delta T)$ of a Bragg reflection depends on the grooves' coverage $l(x)$ with PFMC. More precisely it scales with the square of the form factor of the electron density distribution ($\rho^e_{Si}(z)$, $\rho^e_l(z)$) of one individual, wetted groove

$$I(q_x, \Delta T) \propto |\int_{-a/2}^{a/2} dx e^{iq_x x}\Big(\int_0^{l(x)} dz[\rho^e_{Si}(z) + \rho^e_l(z)]\Big)|^2. \tag{3.11}$$

Eq. (3.11) provides in combination with the liquid-vapor interface $l(x)$ obtained from a numerical treatment of Eq. (3.5) a direct mean to compare experimental and theoretically expected scattering intensities and an indirect way to check the validity of the AYE.
Fig. 3.3, extracted from [33], manifests the validity of the AYE down to 10 nm length scales. The experimental and theoretical scattering intensities $I(\Delta\mu \propto \Delta T)$ show excellent agreement. This agreement emphasizes in particular the importance of long-range dispersion interactions between structured substrate and liquid film.
Predictions for the X-ray scattering intensities based on Rascón's geometric approach that ignores long-range dispersion forces agree less favorably with the experimental results than the full numerical treatment of the AYE ($\rightarrow$ Fig. 3.3). Ignoring the long-range interaction by using the conventional (macroscopic) Kelvin equation appears as oversimplification on the 10 nm scale.
As a final remark to the geometric approach, I want to point towards consequences of its obvious relation with the BJH analysis for the characterization of mesoporous materials ($\rightarrow$ Sec. 2.3.1). From Fig. 3.3, one concludes that the geometric model

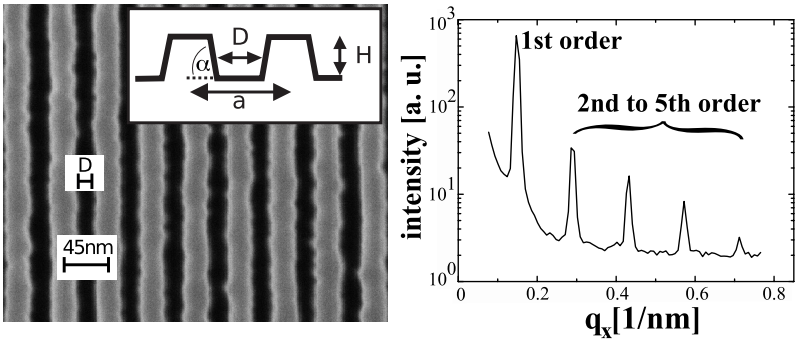

Figure 3.2: (left) SEM image (top view) of the grating. (inset) Trapezoidal cross-sectional shape. (right) X-ray scattering profile along q_x for the pattern shown on the left. Reprinted with permission from Ref. [33]. Copyright 2010 American Physical Society. https://doi.org/10.1103/PhysRevLett.104.106102

and the BJH approach for mesopores underestimate the width of the capillary condensation regime upon filling and therefore implies a narrowed PSD.

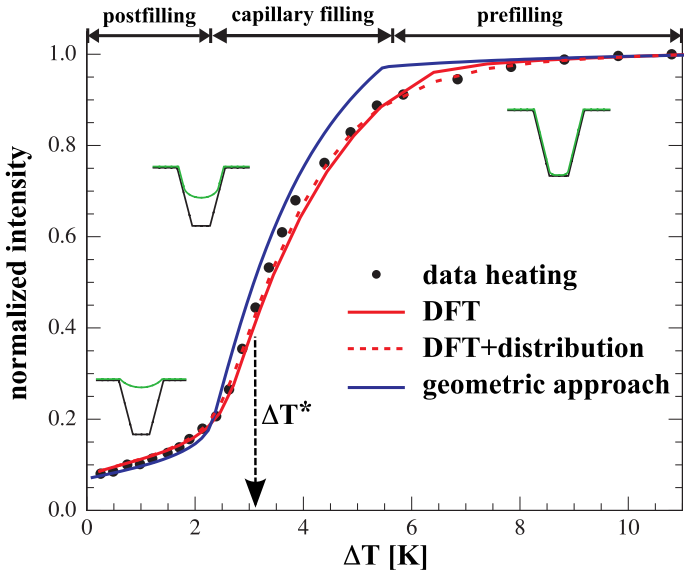

Figure 3.3: Black symbols: X-ray scattering intensity of the first-order Bragg peak as function of ΔT upon heating. Red line (solid): DFT calculation. Red line (dashed): DFT calculation including a 10% wide distribution of D. $\Delta T^* = T_0\gamma_{lv}/(L\rho_l D/2)$ is an estimate for the inflection point of the red curve ($\rightarrow$ original article). Blue line: geometric construction. Reprinted with permission from Ref. [33]. Copyright 2010 American Physical Society. https://doi.org/10.1103/PhysRevLett.104.106102

I refer to publication [33] for more details on the experimental and theoretical parts of the combined X-ray scattering-wetting study. Key publications [42] and [43] provide further insights into nanoscale wetting by means of scattering experiments and microscopic measurements.

3.2 Rayleigh-Plateau Instability & Nanobubbles

Sec. 3.1 clearly shows the potential of X-ray scattering studies on model substrates with well-defined nanostructures for testing fundamental concepts of nanoscale wetting. But it is also possible to look at it from a slightly different perspective. The wetting behavior of liquids on substrates encodes morphological features of the substrate. Probing the wetting behavior of structured materials has therefore the inherent potential to be a powerful method in material science.
Sorption isotherms are in this sense already an indispensable tool to characterize mesoporous materials (→ Sec. 2.3.1). Although running the risk of redundancy let us remember, an isotherm measures the wetting (volumetric uptake) of a volatile liquid in a porous host at constant temperature as the chemical potential of the coexisting gas phase is controlled externally. Subsequently, the BJH-analysis [129] provides one mean to extract a PSD by applying the conventional (macroscopic) Kelvin Eq. (2.1), which ignores long-range solid-liquid interactions.
Another, related analytical technique to characterize porous materials is porosimetry. It measures the forced intrusion of a non-wetting liquid like mercury in the porous network upon applying pressure [123]. A comparison of the pressure necessary for intrusion with the expected capillary pressure of a cylindrical pore $P_c = 2\gamma_{lv}\cos(\Theta)/R$ allows inferring a pore radius R. The capillary pressure appears also as the first term in the AYE (→ Eq. (3.6)).
Publication [37] emphasizes the merit of wetting studies as methodology in material science. I report in the article on synchrotron-based small-angle X-ray scattering experiments on a template-grown, powdery porous silica matrix SBA-15 (→ Sec. 2.1.3) upon in-situ sorption of fluorinated pentane C_5F_{12} along with volumetric gas sorption isotherm measurements (→ Sec. 2.3.1).
In my article [37], I go twofold beyond the conventional BJH-analysis to characterize the PSD, or more generally the pore morphology of SBA-15. I apply a microscopic sorption model (→ Eq. (3.8)) to analyze isotherms. Additionally, I interpret X-ray scattering signals, which become apparent only in a partially filled host, as a consequence of periodic morphological features in SBA-15 on the 10 nm length scale.
Within the mean-field model of Saam and Cole [127] based on Eq. (3.8) for vapor condensation in a cylindrical pore, a N_2 and C_5F_{12} sorption isotherm is well described by a bimodal pore radius distribution dominated by meso- and micropores with 3.4 nm and 1.6 nm mean radius. One assigns these two distinct mean pore sizes as usual to the radii of the tubular nanochannels (mesopores) and the size of side branches (micropores) that form during the polymer calcination and emanate from the main channels [153].
In small-angle X-ray scattering experiments on the powdery SBA-15, two different periodicities become evident (→ Fig. 3.4). One of them ($d_1 = 11.5$ nm) reflects the next nearest neighbor distance in a 2D-hexagonal lattice of tubular mesopores [18] (→ Fig. 2.4). It is expected by design as a consequence of the described templating approach that includes the self-assembling of cylindrical micelles on the 2D-lattice to screen hydrophobic polymer blocks most efficiently from the aqueous solution prior to the sol-gel process (→ Sec. 2.1.3).
A second, slightly smaller periodicity ($d_2 = 11.4$ nm) found during in-situ sorption and freezing experiments is traced back to a superstructure along the cylindrical mesopores. It is compatible with periodic pore corrugations found in electron to-

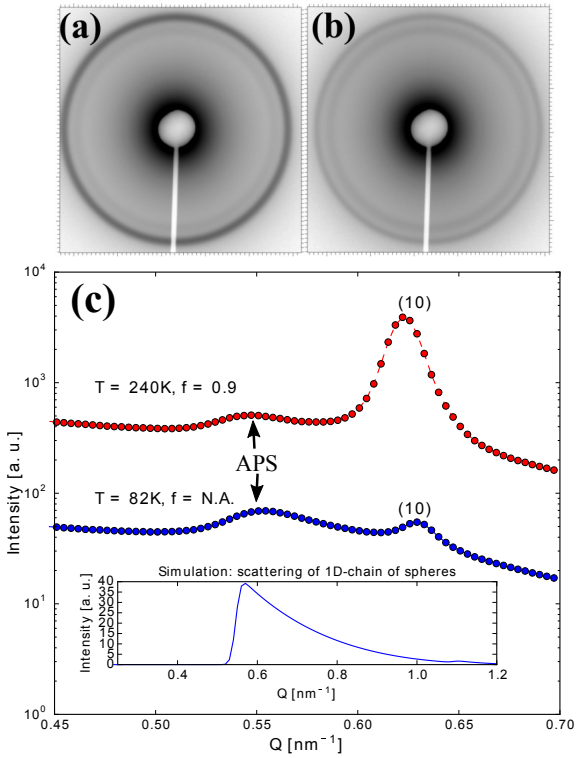

Figure 3.4: The additional periodic signal (APS) in the liquid state at a temperature of 240 K and a filling fraction $f = 0.90$ (a, c) and the solid state at a temperature of 82 K obtained by cooling a completely filled SBA-15 sample (b, c). The inset illustrates a quasi-Bragg reflection caused by a periodic chain of spheres with finite size in a powder average. Reprinted with permission from Ref. [37]. Copyright 2016 American Chemical Society.

mograms of empty SBA-15 by Gommes et al. [154]. The origin of these periodic corrugations is quite fascinating. It is a thermally driven, hydrodynamic instability named after the British mathematician Lord Rayleigh and the Belgian physicist Joseph Plateau [141].†

As any soft matter structure the cylindrical micelles in the SBA-15 templating process are susceptible to thermally driven fluctuations in particular to radial capillary undulations. These undulations can cause a Rayleigh-Plateau shape transition [141] from a single cylindrical micelle to a file of spherical micelles and it is a remarkable observation that the characteristic pore corrugation length as inferred from the scattering experiments agrees well with theoretical predictions [155, 156] for the periodicity of such a file of touching spheres ($\rightarrow$ [37]). It is $d_2 = \Lambda_{RP} = 3.89 R_{BCP}$, where $R_{BCP} = 2.93\,\mathrm{nm}$ the radius of the cylindrical micelle is lightly smaller than the pore radius of the silica mesopores $R = 3.4\,\mathrm{nm}$.

Consequences of the peculiar morphological feature on the spatial arrangement of C_5F_{12}, in particular the formation of periodically arranged nanobubbles (or voids) upon adsorption, desorption and freezing of liquids can be discussed in terms of capillary bridge formation and cavitation in tubular but periodically corrugated pores

†As an entertaining side note, the Rayleigh-Plateau instability is better known as the shape transformation that causes a falling liquid jet to break into spherical droplets upon conservation of total volume but reduction of external surface. An annoying, daily life consequence of the effect is a dripping faucet.

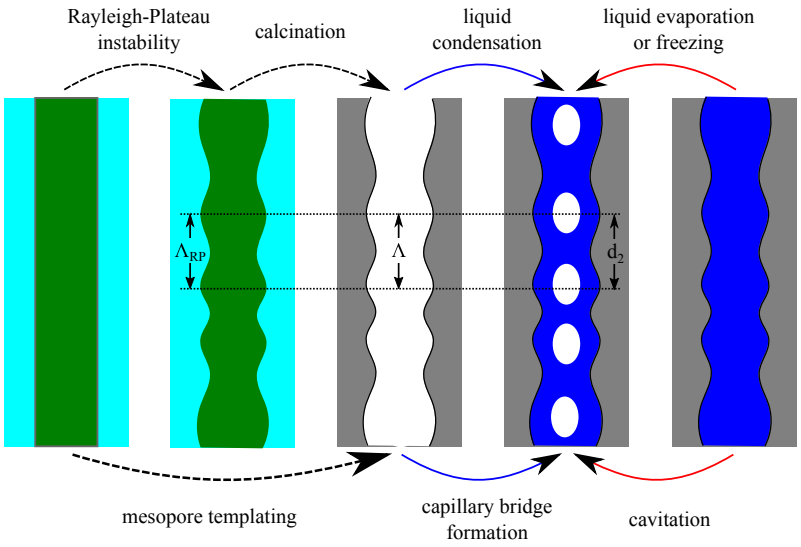

Figure 3.5: Proposed templating process of SBA-15 and envisioned wetting sequence in periodically corrugated nanochannels: 1. Rayleigh-Plateau instabilities in micelles during the templating process cause periodically corrugated mesopores upon calcination. 2. Upon liquid condensation and liquid evaporation nanobubbles form along the tubular pores through liquid bridging and cavitation. Reprinted with permission from Ref. [37]. Copyright 2016 American Chemical Society.

(→ [37]).
Fig. 3.5 illustrates how capillary bridges form in all of these instances to create periodic files of nanobubbles along the channels. It are indeed these chains of nanobubbles that are probed in the scattering experiments. They inherit their periodicity from the characteristic corrugation length and only after their formation at high degree of pore filling the second periodicity becomes unambiguously evident although indications are present also prior to filling (→ [37]).
Publication [37] provides more comprehensive information on the wetting in corrugated pores. Here, only an abridged summary of some main aspects is given in the spirit of a cumulative thesis. I also take the liberty to refer to the excellent article by Gommes [157].

Chapter 4

Structure of Nanoconfined Matter

Structural phase transitions in soft and hard matter upon nanoscale confinement are a fascinating topic to study. It is easy to imagine that a liquid fills a mesoporous host with a more or less complex morphology, like water that penetrates a macroscopic sponge. But with regard to solid phases of matter, a multitude of questions arises. Do liquids solidify in crystalline or amorphous form? Are the same crystalline structures observed as in bulk systems? How are transition temperatures altered? And how do the answers to these questions depend on morphological features like nanostructure sizes, pore geometry and the kind of pore network?
It would be hasty to think that confinement, guest-host interaction and the ratio of volume to interface in the solid phase would not affect the structure of matter. For instance, elementary thermodynamics already predicts that confinement on a length scale R introduces a shift in the liquid-solid phase transition of $\Delta T \propto 1/R$ due to competing surface and volume energies, which scale with R^2 and R^3 in "model" liquids.
Key publications [35], [36] and [44] study the structure of matter upon nanoconfinement to address some of the questions listed above. The articles [35] and [36] compare comprehensively the crystallization of molecular liquids in porous hosts with bulk crystallization. Confined solids are prepared for these studies by first utilizing sorption isotherms (→ Sec. 2.3.1) to fill the porous hosts with liquid and secondly cooling the, then confined, liquid until it solidifies. The nanoimprint-induced molecular orientation in spin-cast semiconducting polymer films is a topic discussed in Ref. [44].
Based on the named publications, I identify and discuss in Sec. 4.1 and 4.2 two guiding mechanisms for the crystallization in pore-confined matter. A nanoscale version of Bridgman growth is often induced in tubular channels by geometric restrictions. Epitaxial overgrowth of nanocrystals is a more exotic crystallization process so far only observed in crystalline pSi. Finally, I provide in Sec. 4.2 an account on the differences between the microscopic structure of a thin polymer film on a flat Si substrate and a nanostructured film, and elaborate on their possible origin in reduced side-wall interfacial energies upon printing.

4.1 Epitaxial Overgrowth in pSi

4.1.1 Deuterium

The crystal structure of confined deuterium cD_2 is studied by means of elastic neutron scattering techniques along the vapor-solid coexistence line. Experiments use

D_2 with a *bona fide* ortho-para spin isomer composition of 2 : 1 at room temperature. Changes in this *normal* composition in favor of the ortho isomer upon cooling are negligible on the time scale (days) of the experiments [158].†
Key publication [35] reports that deuterium with an equilibrium ortho-para composition ($c_{para} < 33\,\%$ for $T < 300\,\mathrm{K}$) forms a cubic closed-packed (fcc) structure in 9 nm wide pSi nanochannels (→ Sec. 2.1.1) in contrast to the expected hexagonal closed-packed (hcp) bulk structure. Further a preferred alignment of D_2 nanocrystals with respect to the surrounding crystalline silicon matrix is discussed in terms of heteroepitaxial growth of solid cD_2 on crystalline pore walls.
The liquid cD_2 freezes in pSi at $T = 14\,\mathrm{K}$ into the cubic phase. This is roughly 5 K below the bulk triple point $T^3_{bulk} = 18.73\,\mathrm{K}$. The appearance of the cubic phase for D_2 with $c_{para} < 33\,\%$ surprises, because a bulk system with the same spin isomer composition solidifies exclusively in a hcp structure upon cooling [158].
Depending on the isomer composition, a transition from hcp to Pa3 - a fcc lattice combined with rotational order of the D_2 molecules along $< 111 >$ directions - becomes possible in bulk crystals below $T = 3.8\,\mathrm{K}$. It however necessitates the presence of anisotropic, quadrupole-quadrupole interactions that are only strong enough in para-enriched (!) D_2 ($c_{para} > 56\,\%$) because only the para isomer with odd rotational quantum number $J = 1$ allows for these interactions [158].
In the wake of the studies in publication [35], no rotational order is found in the probed temperature range $1.7\,\mathrm{K} < T < 14\,\mathrm{K}$ for the cubic cD_2. This agrees with the expectations because the experiments utilize D_2 with fairly low para content $c_{para} < 33\,\%$. One should however remark, that even in macroscopic bulk samples it is more than challenging to prove unambiguously molecular rotational order by means of neutron scattering techniques [159]. Pa3 superstructure reflections in D_2 are notoriously weak.
The interaction of cD_2 with the crystalline pSi substrates alters the free energy landscape, obviously favoring the fcc over the hcp phase. This becomes possible because the free energy difference between fcc and hcp structures is marginal to begin with. After all ABC and AB stacking sequences differ locally only in the third coordination shell. In this context, it was for instance a long standing debate why rare gases with the exception of helium form fcc lattices upon freezing rather than hcp ones although two-body interactions slightly prefer the latter [160].
It is also the D_2-pSi interaction that triggers an epitaxial growth of D_2 crystals (→ Fig. 4.1). It is remarkable that the scattering intensity due to the crystalline structure of cD_2 is not distributed more or less equally over Debye-Scherrer rings as expected for a powdery solid and indicated for the aluminum reflections of the sample cell. Rather, well-defined Bragg reflections are found in reciprocal space indicating a high degree of crystallinity and texture. More so, the location of Bragg reflections in direct vicinity of the Si reflections evidence a strong alignment of the cD_2 nanocrystals with the pSi matrix.
The last statement requires some amendments. As some reflections are allowed in a fcc structure but forbidden in the Si diamond structure, not all D_2 reflections can

†D_2 is a homonuclear diatomic molecule of spin $I = 1$ atoms. Its total nuclear spin-rotational state wave function has consequently bosonic character. The states with rotational quantum number $J = 1$ and $J = 0$ are referred to as para and ortho D_2. Please note that this assignment is reversed for diatomic molecules of spin $I = 1/2$ atoms with fermionic wave functions such as H_2 or N_2. The expressions "ortho" and "para" always indicate a wave function that is symmetric or antisymmetric under spin exchange.

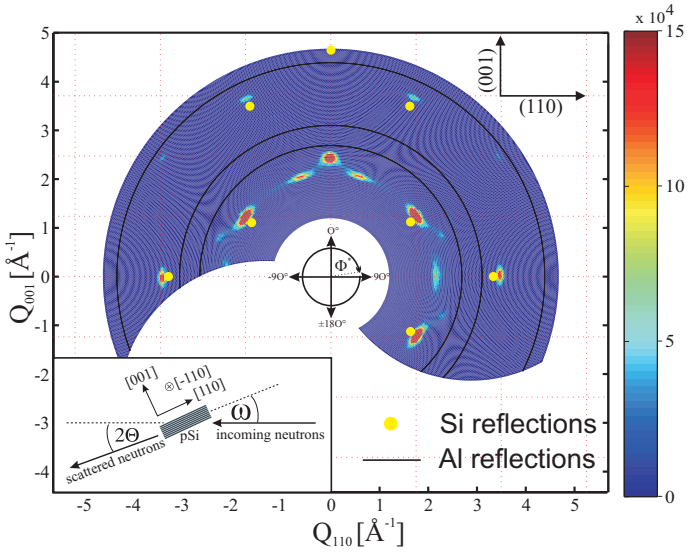

Figure 4.1: Scattered intensity at $T = 1.7\,\mathrm{K}$ in the $(\bar{1}10)$-plane, recorded with a Si-mono-flatcone detector at IN20 (ILL, France) [161, 162]. Background scattering from Si wafers and Al sample cell are subtracted. Q_{110} and Q_{001} depict wavevector transfers in the [110]-direction of Si crystals and along the [001] surface normal. The inset illustrates the scattering geometry. Reprinted with permission from Ref. [35]. Copyright 2013 American Physical Society. https://doi.org/10.1103/PhysRevLett.110.065505

have a Si neighbor in the intensity map. The 002 reflection is one example. Further, a detailed analysis of Fig. 4.1 shows that D_2 nanocrystals form several domains. One domain is perfectly aligned with the single crystalline Si matrix. Its origin is an epitaxial growth of the solid on the pore walls. Several other domains evolve from strain induced twinning out of the perfectly aligned one ($\rightarrow$ [35]).
D_2 is not the only molecular crystal that grows epitaxially in pSi. Neutron scattering experiments indicate, that this particular growth scenario is also found during solidification of the rare gases argon, krypton, neon and xenon. Helium can neither be named on nor excluded from this list due to a lack of experiments. It is the only system that does not solidify along its liquid-vapor coexistence line, not even at lowest temperatures. It poses an exceptional, not resolved experimental challenge to apply the required pressure for solidification to pore confined He to perform the necessary experiments.

4.1.2 Nitrogen

Diatomic, homonuclear nitrogen molecules come in form of ortho ($J = 1$) and para ($J = 0$) spin isomers like D_2 molecules or more accurately like H_2 molecules.[†] There is a *normal* ortho-to-para equilibrium composition of 3 : 1 at room temperature that means the $J = 1$ molecules are the dominant species. Normal bulk nitrogen solidifies upon cooling at $T^3_{bulk} = 63.15\,\mathrm{K}$ in a hexagonal closed packed phase. The fraction of ortho molecules suffices to trigger a structural transformation at $T = 35.6\,\mathrm{K}$ into a Pa3 phase with rotational order by means of quadrupole-quadrupole interactions [163].

[†]All diatomic, homonuclear molecules with finite nuclear spin per atom show spin isomerism. It is only that H_2 and D_2 are the commonly discussed examples.

Solid normal N_2 exhibits the same structural phase sequence as para-enriched D_2. These correspondences in the bulk phases point towards similar structural properties upon confinement in pSi. Indeed, elastic neutron scattering experiments on solid cN_2 in 9 nm wide pSi pores indicate an epitaxial overgrowth of crystals in the porous host ($\rightarrow$ Fig. 4.2). Upon freezing at $T = 56\,\mathrm{K}$, an fcc phase without rotational order forms. Domains of fcc nanocrystals that are aligned perfectly with the single crystalline Si lattice replace the expected hcp bulk phase.
Fig. 4.2 exhibits the texture of solid N_2 upon confinement in pSi. It resembles the one of D_2 evident in Fig. 4.1 except for one remarkable difference. Intense streaks of scattering intensity along the $< 111 >$ directions emanate from the Bragg reflections. There are no Bragg reflections that originate from twinned nanocrystals. This difference appears as a consequence of an increased probability for stacking faults in solid cN_2.
The twinning of fcc crystals in cD_2 results from a small but finite probability for strain induced stacking faults in the various $< 111 >$ directions. They can for instance change an ABCABCABC stacking sequence into ABCABCBAC ($\rightarrow$ [35]) that is the transition from one crystal to two twinned crystals. However, if the probability for stacking faults increases then it goes along with diminishing translational periodicity along the $< 111 >$ directions, which causes significant diffuse scattering. Bragg rods [138] form in reciprocal space along these directions.
As for the origin of an increased number of strain induced stacking faults in cN_2 compared with cD_2, one could unsatisfactorily speculate that it must be a combined consequence of the different elasticity of N_2 and D_2 and the different lattice mismatches between host and guest because they both define the strain energy. The lattice mismatch as source of strain might be larger for deuterium than for nitrogen. It is $(a_{N_2} - a_{Si})/a_{Si} = 4\%$ and $(a_{D_2} - a_{Si})/a_{Si} = -7\%$ with the cubic lattice constants a_{Si,N_2,D_2} of Si, N_2 and D_2 [163, 164]. But neutron scattering studies on the phonon dispersions seemingly imply a significantly higher stiffness in nitrogen than in deuterium [165, 166].
A final observation has to round up the discussion of the scattering data. No rotational order is observed in pSi for ortho-rich ($J = 0$) cD_2. The situation is however different for ortho-rich ($J = 1$) cN_2 in pSi. A molecular rotational order is evident in the experiments at $T < 29\,\mathrm{K}$ upon cooling the confined fcc phase (not shown). The absence of the superstructure reflections $\overline{112}$ and $\overline{221}$ at $T = 45\,\mathrm{K}$ and their presence at $T = 8\,\mathrm{K}$ in Fig. 4.2 evidence unsurprisingly the fcc $\rightarrow$ Pa3 transition for the ortho-rich N_2 in confinement.
The presented discussion of cN_2 has obviously a somehow preliminary, descriptive character as a finalized study has yet to be published. In this spirit, I want to put forward one attention-seeking aspect of the results. It is interesting that the existence of the cubic phase does not necessitate rotational order in confinement because of the epitaxial overgrowth in pSi. Rather, rotational order occurs only several degrees into the cubic phase. A continuous phase transition exists in confinement that does not couple to a lattice reconstruction. This situation is unknown in the bulk with its direct, first-order transition from hcp to Pa3 triggered by the urge for ordering. The quadrupolar interactions "select" the fcc lattice over the hcp lattice [158] intimately coupling the discontinuous and continuous transitions.

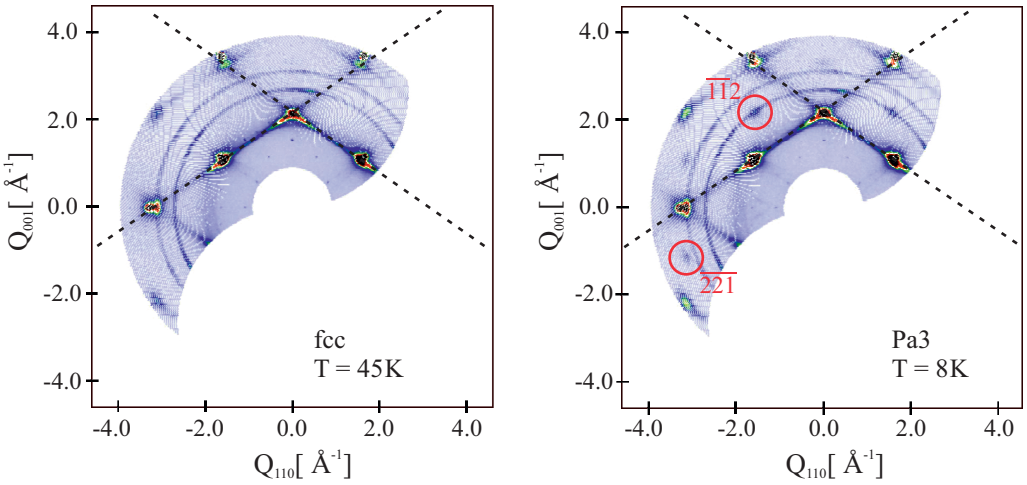

Figure 4.2: Scattered intensity in the $(\bar{1}10)$-plane, recorded with an area detector at E2 (HZB, Germany) [167]. Q_{110} and Q_{001} depict wavevector transfers in the [110]-direction of Si crystals and along the [001] surface normal. Background scattering from Si wafers and Al sample cell are not (!) subtracted. Dashed lines indicate $< 111 >$ directions. (Left) cubic face centered structure at $T = 45\,\mathrm{K}$. (Right) cubic Pa3 structure at $T = 8\,\mathrm{K}$. Superstructure reflections due to rotational order are marked. Not yet published.

4.2 Nanoscale Bridgman Growth

Solid oxygen appears in three different structural phases along its vapor-solid coexistence line. It forms a cubic γ-phase below $T = 53.8\,\mathrm{K}$, an orthorhombic β-phase at temperatures lower than $T = 43.8\,\mathrm{K}$ and a monoclinic α-phase with antiferromagnetic order below 23.8 K. Structural equilibrium transitions are the consequence of a complex interplay between molecular dispersion forces, anisotropic quadrupolar and anisotropic magnetic interactions [168].

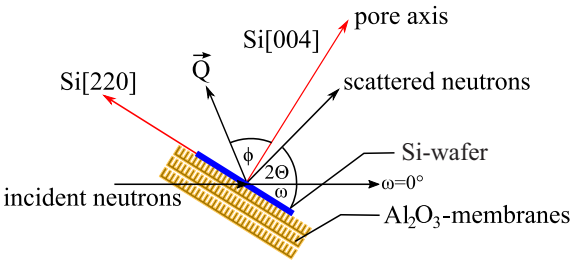

Figure 4.3: Scattering geometry: Incident and scattered neutrons define the scattering angle 2Θ. The orientation of the sample with respect to the incident neutron direction is given by ω. The angle ϕ characterizes the orientation of the wavevector transfer $\mathbf{Q}$ with respect to the pore axis. An attached piece of single crystalline Si facilitates determining the sample orientation. Reprinted from Ref. [36], with the permission of AIP Publishing.

Publication [36] presents a comprehensive neutron scattering study on solid oxygen spatially confined in 12 nm wide AAO nanochannels (→ Sec. 2.1.2). Elastic scattering experiments reveal a structural phase sequence in cO_2 known from bulk. With decreasing temperature cubic γ-, orthorhombic β- and monoclinic α-phases are unambiguously identified in confinement with decreased transition temperatures

$T_{liquid\to\gamma} = 50\,\mathrm{K}$, $T_{\gamma\to\beta} = 38\,\mathrm{K}$ and $T_{\beta\to\alpha} = 18.5\,\mathrm{K}$. Weak antiferromagnetic order is observed in the confined α-phase.
The parallel alignment of the tubular nanochannels along the surface normal of amorphous AAO membranes (→ Sec. 2.1.2) allows probing the texture of the confined solid by means of rocking scans. They measure the scattering intensity of selected Bragg reflections depending on the sample orientation (→ Fig. 4.3) and reveal that cO_2 nanocrystals inside the tubular channels do not form an isotropic powder. From rocking scans on cD_2 and cN_2 in pSi (→ Sec. 4.1) similar insights were gained by utilizing the single crystalline Si matrix as reference for the nanocrystals' orientation (→ inset of Fig. 4.1). This possibility of course does not exist for the amorphous AAO.

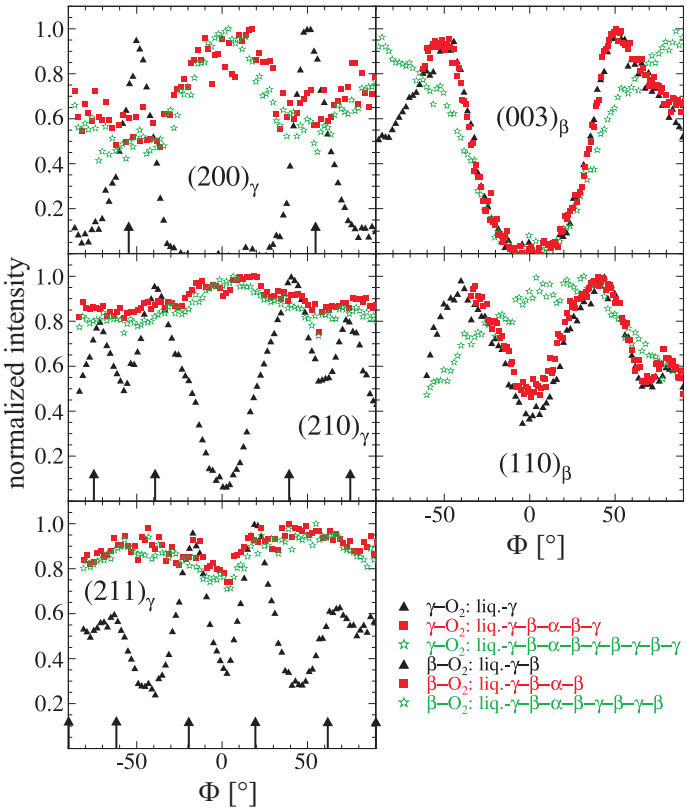

Figure 4.4: Rocking scans for various reflections in γ- and β-phase depending on thermal history. Recorded at E6 (HZB, Germany) [169]. Arrows mark reflex positions as expected for γ-crystals, which are aligned with their [111] direction parallel to the pore axis ($\Phi = 0°$). Reprinted from Ref. [36], with the permission of AIP Publishing.

The orientation of the nanocrystals in the three solid oxygen phases is by no means uncorrelated to the symmetry axis of the tubular pores. Thermal history, microscopic transition mechanisms and preferred crystal growth directions control the orientation of nanocrystals in the pores on a macroscopic scale (→ Fig. 4.4).
Preferred crystal growth directions define textural characteristics after the liquid-γ transition. A multitude of nanocrystals nucleate at the onset of freezing with random orientation and increase in size upon solidification. This growth process favors in tubular channels nanocrystals that align with the fast growing crystallographic direction along the pore axis (→ Fig. 4.5). For the liquid-γ transition it is the [111] direction that aligns. The described "seed" selection upon solidification is a

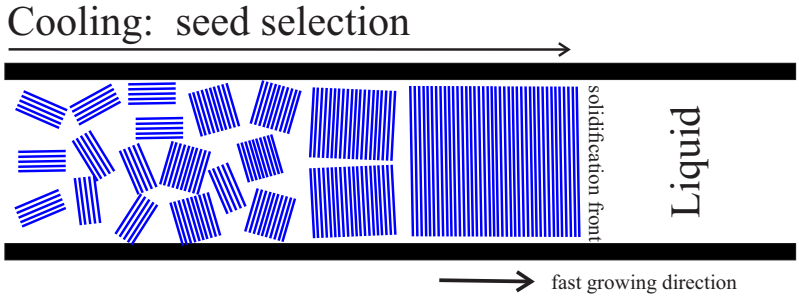

Figure 4.5: Nanoscale Birdgman growth: Seed selection in a tubular pore upon continuous cooling.

nanoscale version of the well-known Bridgman technique [170] to synthesize single crystals.
Textural similarities between β- and α-cO_2 trace back to the mechanism that triggers the orthorhombic to monoclinic transition [171, 172]. The texture in the β-phase as evolved from an anisotropic γ-phase remains mysterious. It might appear as a convoluted result of nucleation and growth of the lower symmetry phase as well as molecular displacements that accompany the transition.
A comprehensive discussion of the texture of cO_2 in AAO as well as its magnetic structure in the α-phase is found in publication [36]. Here I close with the statement, that the nanoscale Bridgman mechanism has been observed before in pore confined solids. It is discussed in Ref. [173–175]. It was as well observed by myself in cN_2 and cD_2 upon confinement in AAO.

4.3 Nanoimprinting

Molecular electron donor-acceptor pairs are the organic electronics' equivalent to the p-n junctions in inorganic diodes [21]. In this context, poly-3(hexylthiophene) (P3HT) is intensively discussed as donor in organic photovoltaics to acceptors such as [6,6]-phenyl-C_{61}-butyric acid methyl ester (PCBM). P3HT is a polymer that consists of a backbone of thiophene rings with hexyl side chains. π-orbitals of the thiophene rings are partially delocalized along the backbone [176, 177], the degree of conjugation depending on the chain configuration (straight vs. folded). The interchain overlap of π-orbitals in amorphous or π-π stacking in (semi)crystalline P3HT can define highly conductive pathways.
Since the exciton diffusion length in organic solar cells is in the order of ten nanometers [178] prior to electron-hole recombination, such devices come often in form of heterogeneous donor-acceptor blends [179]. They utilize microphase separation on these length scales for splitting the excitons at the donor-acceptor interfaces. An alternative approach are bilayers of donor and acceptor materials. Nanostructuring of the layer interface is here the key to increased charge carrier harvesting [180]. This context provides the overarching framework for study [44], which investigates changes in morphology and orientation of thin, (semi)crystalline P3HT films upon nanoimprinting and subsequent thermal annealing by means of GISAXS/GIWAXS experiments (→ Sec. 2.3.2).
In (semi)crystalline P3HT films one identifies three distinct crystallographic directions (→ Fig. 4.6). The polymer forms molecular layers in the [100] direction, [010] coincides with the π-π orbital stacking direction and [001] is parallel to the polymer

backbone. Thin P3HT films adopt on a flat Si support the edge-on configuration (→ Fig. 4.6) in which the [100] direction aligns with the surface normal as evidenced by GISAXS studies (→ Fig. 4.7). The edge-on configuration observed on flat substrates is likely the lowest energy configuration since it maximizes the coverage of the low-energy methyl groups at both interfaces (polymer-substrate & polymer-air). Ocko et al. [181] discuss the same driving force as origin for surface freezing in chain molecules.

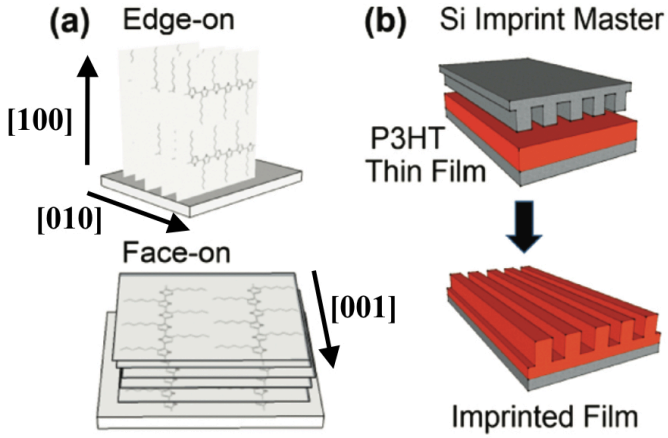

Figure 4.6: Schematics of (a) edge-on and face-on orientation of P3HT domains and (b) the nanoimprint process. Reprinted (adapted) with permission from Ref. [44]. Copyright 2011 American Chemical Society.

Morphology and orientation of such a thin P3HT film - important parameters influencing electronic and photovoltaic device performance - are however significantly altered upon nanoimprinting with 100 nm spaced grooves (→ Fig. 4.6). After applying a pressure of 3.4 MPa between the imprint Si master and polymer coated substrate at $T = 423$ K for 5 min, quenching to room temperature, and subsequent pressure release, the imprinted polymer film (still on a Si support) appears as topographic replica of the imprint Si grating. GISAXS studies demonstrate the excellent fidelity of the pattern transfer (→ [44]). The GIWAXS intensity maps in Fig. 4.7 convincingly show an imprinting-induced π-π reorientation and polymer backbone alignment along the imprinted channels.
Scattering intensity of the 100 reflection[†] along the longitude ($\eta = 90°$) and 010 intensity along the latitude ($\eta = 0°$) indicate in Fig. 4.7 edge-one configurations. Vice versa, a face-on configuration of a sizable number of polymer chains is evidenced by 010 scattering at the poles and equatorial 100 intensity. The backbone alignment is inferred from the Φ dependent η-scans. I refer to Fig. 2.10 in Sec. 2.3.2 and Fig. 4.7 for details on the scattering geometry and the obvious definitions of Φ, the sample rotation around its normal and η, the polar angle in the intensity maps.
For the imprinted film, with its considerable side-wall area, the observed 90° reori-

[†]Equipped with a basic knowledge on single crystal X-ray scattering geometries, the reader might rightfully question the ability to infer at all a 100 wavevector transfer parallel to the surface normal in a GIWAXS experiment with fixed wavelength $\lambda = 0.0886$ nm and fixed incidence angle $\alpha_{inc} << 1°$. Although being correct in final consequence, he or she should consider that the GIWAXS geometry benefits from the mosaicity of a soft polymer (semi)crystal, which is evidently larger than the difference between the fixed incidence angle α_{inc} and the required incidence angle $\alpha_{Bragg} = \theta = 1.45°$ to fulfill the Bragg condition.

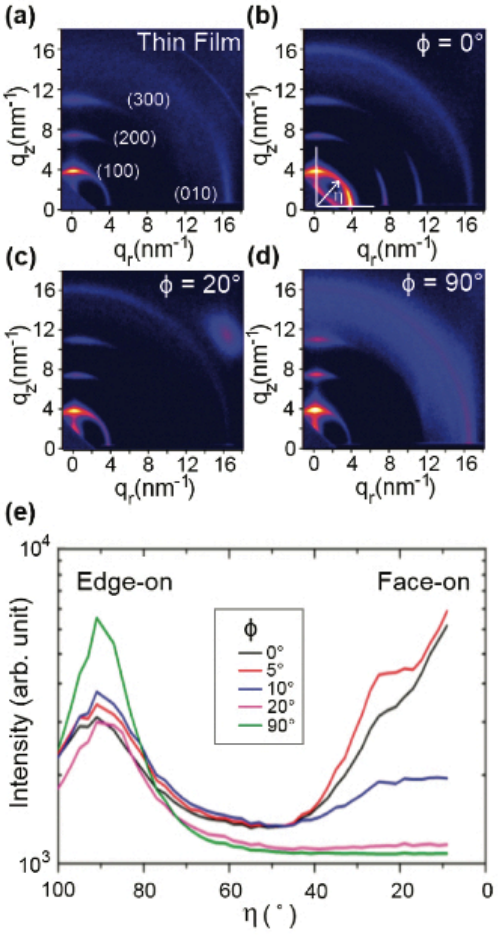

Figure 4.7: Two-dimensional GIWAXS patterns of (a) uniform P3HT thin film and (b) imprinted P3HT taken with azimuthal angle (b) $\Phi = 0°$, (c) $\Phi = 20°$, and (d) $\Phi = 90°$. There are q_z and q_r the out-of-plane and in-plane projections of the wavevector transfer with respect to the thin film. The azimuthal angle Φ is defined as zero when the grating is parallel to the direction of incident X-rays ($\rightarrow$ Fig. 2.10). (e) Polar angle (η) scans along the (100) peak positions for various Φ. The polar angle η is defined as zero for wavevector transfers $q_z = 0\,\mathrm{nm}^{-1}$. Reprinted (adapted) with permission from Ref. [44]. Copyright 2011 American Chemical Society.

entation is likely driven by the reduction of the side-wall interfacial energy, which induces the $< 100 >$ direction to be along the local surface normal. However, one cannot rule out other factors such as flow-induced reorientation which may also contribute upon printing at elevated temperatures [182].
Article [44] obviously provides a more comprehensive account on the touched topics. Beyond the preceding discussions, the article elaborates on the surprising and noteworthy observation that temperature-dependent scattering measurements evidence imprinted induced orientation and alignment even at temperatures where the imprinted topographical features nearly vanish. The molecular reorientation excels in its thermal robustness.

Chapter 5

Dynamics in Nanoconfined Matter

It is a fascinating endeavor to investigate changing dynamics in hard and soft matter as the system size is reduced from macroscopic to mesoscopic length scales. A modified behavior manifests in thermal equilibrium, near thermal equilibrium or even out-of-equilibrium and is of diverse origins. Among the reason for altered characteristics are low dimensionality, confinement, interface effects or even quantum effects. I show in this chapter - the last of the four main chapters promised in the introduction - how mesoporous materials (→ Ch. 2) are utilized in the key publications [34], [38], [39], [41] and [45] to address different aspects of dynamics in nanostructured materials. To be more specific, the chapter and named articles discuss molecular diffusion processes, phonon propagation and thermal transport in structured matter.
Key publications [34] and [45] present quasi-elastic neutron scattering experiments that probe stochastic motions in molecular liquids, which are confined in pSi and CDCs (→ Sec. 2.1.1 & 2.1.5). Publications [38] and [39] present the crystalline structure of pSi as unique opportunity to elucidate the phonon dispersion of a mesoscopic material across the Brillouin zone by means of inelastic neutron scattering experiments. Near-equilibrium thermal transport in nanostructured SPS-pSi is the core topic of Ref [41].

5.1 Dynamic Structure Factor

5.1.1 A Primer

The atomic and molecular dynamics in solids and liquids is encoded in the dynamic structure factor[†]

$$S(\vec{Q},\omega) = \frac{1}{2\pi}\int_{-\infty}^{\infty} d\vec{r}dt\,\exp(i\vec{Q}\vec{r} - i\omega t)G(\vec{r},t). \tag{5.1}$$

It is the space-time Fourier transform of the Van Hove function $G(\vec{r},t)$ that correlates the presence of a particle in position $\vec{r}(t=0)$ at time $t=0$ and the presence of a particle in position $\vec{r}(t=0)+\vec{r}$ at time t [183]. For N particles one writes

$$G(\vec{r},t) = \frac{1}{N}\Big\langle \int d\vec{r}' \sum_{i,j=1}^{N} \delta[\vec{r}' - \vec{r}_i(0)]\delta[\vec{r}' + \vec{r} - \vec{r}_j(t)]\Big\rangle \tag{5.2}$$

[†] $S(\vec{Q},\omega)$ is also called the scattering function. This name is misleading because $S(\vec{Q},\omega)$ describes properties of a system independent of any scattering probe.

with the canonical ensemble average $\langle ... \rangle$. $G(\vec{r},t)$ is the sum of the self-pair correlation function

$$G_s(\vec{r},t) = \frac{1}{N}\Big\langle \int d\vec{r}' \sum_{i=1}^{N} \delta[\vec{r}' - \vec{r}_i(0)]\delta[\vec{r}' + \vec{r} - \vec{r}_i(t)]\Big\rangle \tag{5.3}$$

and the distinct-pair correlation function

$$G_d(\vec{r},t) = \frac{1}{N}\Big\langle \int d\vec{r}' \sum_{i\neq j=1}^{N} \delta[\vec{r}' - \vec{r}_i(0)]\delta[\vec{r}' + \vec{r} - \vec{r}_j(t)]\Big\rangle \tag{5.4}$$

that correlate the positions of one particle (i) at two different times $(0,t)$ and the positions of two distinct particles (i,j).
It was Van Hove [183] who showed that the double differential cross section [184] of an inelastic neutron scattering experiment can be written as

$$\frac{d^2\sigma}{d\Omega d(\hbar\omega)} = \frac{N}{4\pi\hbar}\frac{k_f}{k_i}\big[\sigma_{ch}[\underbrace{S_d(\vec{Q},\omega) + S_s(\vec{Q},\omega)}_{S(\vec{Q},\omega)}] + \sigma_{ich}S_s(\vec{Q},\omega)\big] \tag{5.5}$$

with the wavevectors $\vec{k}_i$ and $\vec{k}_f$ of incident and scattered neutrons, the wavevector transfer $\vec{Q} = \vec{k}_i - \vec{k}_f$, the energy transfer $\hbar\omega$ between neutron and sample, the coherent and incoherent scattering cross sections σ_{ch} and σ_{ich} of the particles, and the obvious definitions of $S_d(\vec{Q},\omega)$ and $S_s(\vec{Q},\omega)$ as the space-time Fourier transforms of $G_d(\vec{r},t)$ and $G_s(\vec{r},t)$.
The intimate relation between the double differential cross section and the dynamic structure factor allows experimentally probing the structure and dynamics of matter. It is $S_d(\vec{Q},\omega)$ that contains vital information about the crystal structure and phonon dispersion of solids. The phonon density of states in solids and stochastic motions in molecular liquids such as translational diffusion or molecular rotations are encoded in $S_s(\vec{Q},\omega)$ [184].

5.1.2 Example: Diffusion

The molecular self-diffusion in a liquid provides a thesis relevant example for $G_s(\vec{r},t)$ in Eq. (5.3) and $S_s(\vec{Q},\omega)$ in Eq. (5.5). Its self-pair correlation function, assuming a continuous diffusion process, obeys the macroscopic transport equation that is Fick's law [185]

$$\frac{\partial G_s(\vec{r},t)}{\partial t} = D\nabla^2 G_s(\vec{r},t) \tag{5.6}$$

with the diffusion constant D. With the isotropic solution

$$G_s(r,t) = (4\pi Dt)^{-3/2}\exp(-r^2/4Dt) \tag{5.7}$$

it is elementary to calculate

$$S_s(Q,\omega) = \frac{1}{\pi}\frac{\hbar DQ^2}{(\hbar\omega)^2 + (\hbar DQ^2)^2}. \tag{5.8}$$

The incoherent quasi-elastic scattering intensity is Lorentz-distributed around the elastic line $\hbar\omega = 0\,\text{meV}$ for fixed wavevector transfer Q. The Q-dependent width

determines D.
A favorable situation arises for an experimentalist studying stochastic motions in a liquid when $\sigma_{ich} >> \sigma_{ch}$ because the scattering experiment becomes solely sensitive to the molecular self-dynamics. Studies [34] and [45] exploit such a situation, since the incoherent scattering on hydrogen atoms (protons) dominates in the liquids under investigation.

5.1.3 Example: Phonons

The dynamic structure factor for one-phonon dynamics in a primitive crystal with one atom per unit cell is a little bit tedious to calculate [184, 186] but writes neatly as

$$S(\vec{Q},\omega) = \frac{4\pi^3\hbar}{NMV}\exp(-2W_{\vec{Q}})\sum_{\vec{\tau},\vec{\epsilon},\vec{q}}\frac{(\vec{Q}\cdot\vec{\epsilon}_{\vec{q}})^2}{\omega_{\vec{\epsilon},\vec{q}}} \times\Big[(n(\vec{q})+1)\delta(\omega-w_{\vec{\epsilon},\vec{q}})\delta(\vec{Q}-\vec{q}-\vec{\tau}) +n(\vec{q})\delta(\omega+w_{\vec{\epsilon},\vec{q}})\delta(\vec{Q}+\vec{q}-\vec{\tau})\Big]. \tag{5.9}$$

Here is $\vec{Q}=\vec{k}_i-\vec{k}_f$ the wavevector transfer, $\vec{q}$ the phonon quasiparticle momentum, $\vec{\tau}$ a reciprocal lattice vector, $\vec{\epsilon}_{\vec{q}}$ the phonon polarization, V the unit cell volume, M the atom mass, $n(\vec{q})$ the thermal phonon population and $\hbar\omega_{\vec{\epsilon},\vec{q}}$ the phonon energy. The exponential term in front of the sum is the Debye Waller factor.
Eq. (5.9) provides important insights for neutron scattering experiments as the ones discussed in key publications [38] and [39]. The presence of various δ-distributions indicates not surprisingly that coherent inelastic neutron scattering is only possible if energy and quasimomentum are conserved. Two distinct one-phonon processes exist. The first and second term in the square brackets reflect phonon creation and annihilation that are two scattering channels that allow probing a distinct phonon $\vec{q}$. Since $S(\vec{Q},\omega)$ scales with $(\vec{Q}\cdot\vec{\epsilon}_{\vec{q}})^2$, phonons cannot be measured when their polarization vector is perpendicular to the wavevector transfer and one ideally studies phonons in higher Brillouin zones to enhance the scattering signal.
Eq. (5.9) describes only the one-phonon dynamics. Therefore it contains no information about the finite quasiparticle lifetime $\tau = \hbar/\Gamma(\omega_{\vec{\epsilon},\vec{q}})$ due to phonon-phonon scattering, a multi-phonon process. To this end, one has to replace the δ-distributions that express energy conservation with Lorentz functions of appropriate widths $\Gamma(\omega_{\vec{\epsilon},\vec{q}})$ to account for the energy spread associated with phonon creation and annihilation [187]. Of course, there are other scattering mechanisms like phonon-electron or phonon-boundary scattering that contribute to this spread as well.

5.2 Stochastic Motions

5.2.1 Hexane in pSi

I present in publication [34] incoherent quasi-elastic neutron scattering measurements [185] in a wavevector transfer range from 0.4 Å^{-1} - 1.6 Å^{-1} on liquid n-hexane confined in tubular, parallel-aligned nanochannels of 6 nm mean diameter and 260 µm

length in monolithic pSi (→ Sec. 2.1.1). The anisotropy of the pSi host allows searching for directional dependencies in the molecular dynamics. Measurements on confined liquids are complemented with, and compared to measurements on the bulk system in a temperature range from 50 K - 250 K.
The time-of-flight data [186] are recorded at spectrometer IN5 (Institut Laue-Langevin, France). For the bulk liquid they can be modeled by microscopic translational as well as fast localized rotational, thermally-excited, stochastic motions of the molecules. The molecular dynamics in the nanoconfined state of the liquid, which was prepared by vapor condensation (→ Sec. 2.3.1), is analyzed by means of the dynamic structure factor[†]

$$S_s^{total}(Q,\omega) = (1-f_c)\left(\frac{A(Q)}{\pi}\frac{\gamma_T}{\hbar^2\omega^2+\gamma_T^2}\right. \\ \left. -\frac{1-A(Q)}{\pi}\frac{\gamma_T+\gamma_{loc}}{\hbar^2\omega^2+(\gamma_T+\gamma_{loc})^2}\right)+\frac{f_c}{\hbar}\delta(\omega), \tag{5.10}$$

utilizing a ω-convolution ($*$) with the energy resolution function $R(Q,\omega)$:

$$S_s^{exp}(Q,\omega) = R(Q,\omega) * S_s^{total}(Q,\omega). \tag{5.11}$$

The two Lorentz functions in $S_s^{total}(Q,\omega)$ originate from the convolution of the dynamic structure factors for a translational diffusion (time scale $\tau = \hbar/\gamma_T$) and a localized rotational motion ($\tau = \hbar/\gamma_{loc}$), both assumed to be mutually independent. The δ-distribution allows for part of the molecules to be entirely immobile therefore causing only elastic scattering ($\hbar\omega = 0\,\mu$eV). $A(Q)$ is the elastic incoherent structure factor that emerges from spatial restrictions by definition imposed on localized stochastic motions [188].
Analyzing the temperature dependent scattering data with Eq. (5.11), I find in the confined liquid two molecular populations with distinct dynamics, a fraction f_c which is immobile on the time scale of 1 ps - 100 ps probed in our experiments and a second component $(1-f_c)$ with a self-diffusion dynamics $D(T)$ slightly slower than observed for the bulk liquid (→ Fig. 5.1). A potential anisotropy of the translational diffusion with regard to the orientation of the channels' long axes remains however elusive.
The immobile fraction amounts to about 5 % at 250 K and accounts likely for molecules stuck to the pore walls. It gradually increases upon cooling and exhibits an abrupt increase at 160 K ($\approx$ 20 K below bulk crystallization), which indicates pore freezing (→ Fig. 5.2). One observes here a manifestation of the reduced liquid-solid transition temperatures that are characteristic for matter upon confinement (→ Ch. 4). Although one might consider the experimental approach used to infer it as slightly exaggerated.

5.2.2 Ionic Liquids in CDCs

Key publication [45] reports on the influence of spatial confinement on the thermally excited stochastic cation dynamics of the room-temperature ionic liquid 1-N-butylpyridinium bis-[(trifluoromethyl)sulfonyl]imide ([BuPy][Tf2N]) inside CDCs

[†]I am a little reckless in [34] and refer to $S(Q,\omega)$ occasionally as *differential cross section* or *intensity*. That youthful sin hopefully being forgiven, experimental data are indeed presented in form of a dynamic structure factor and so are the theoretical models.

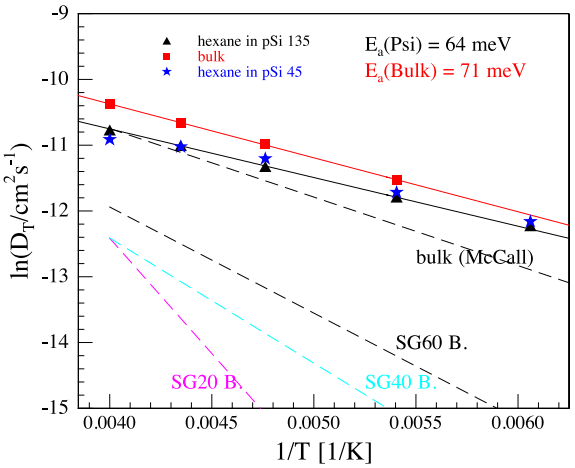

Figure 5.1: Arrhenius plot for the T-dependence of the translational diffusion coefficient D_T: Squares denote bulk data. Triangles and stars refer to diffusion coefficients along the pore axis ($Q \parallel$ pore axis) and perpendicular to the pore axis ($Q \perp$ pore axis). Solid lines illustrate linear fits to extract the activation energies E_A. Dashed lines exhibit IQENS results from Baumert et al. as shown in [189] for mesoporous silica gels with 2 nm, 4 nm and 6 nm pore diameter and results from McCall et al. obtained in NMR spin-echo experiments [190]. Results of Baumert et al. are not corrected for a missing factor of 2π. Reprinted from Ref. [34], with the permission of AIP Publishing.

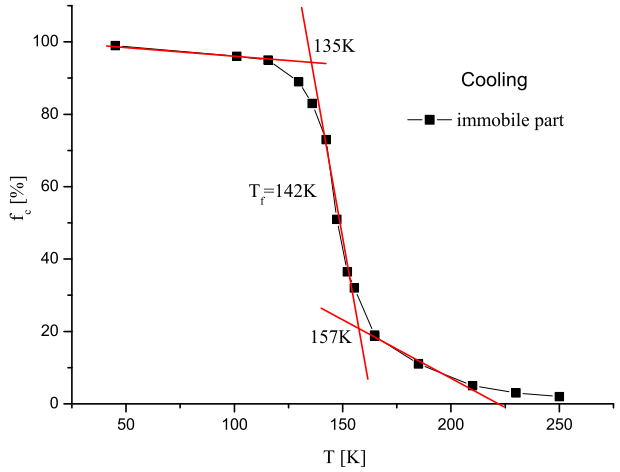

Figure 5.2: Temperature dependence of the amount f_c of immobile hexane in the pores. Symbols represent values extracted from the scattering data. Lines help to guide the eye. Reprinted from Ref. [34], with the permission of AIP Publishing.

(→ Sec. 2.1.5) with various pore sizes (→ Fig. 2.6) in the sub- to a few nanometer range. Molecular dynamics in confinement is investigated by quasi-elastic neutron scattering at FOCUS (Paul Scherrer Institute, Switzerland) [191], a time-of-flight spectrometer and IN16B (Institut Laue-Langevin, France) [192], a backscattering spectrometer [186].
An overview of the dynamic landscape within a wide temperature range as depicted in Fig. 5.3 is obtained using the potential of fixed window scans at IN16B, in other

words scanning the temperature, while observing the scattering intensity solely for one specific energy transfer value. A first qualitative observation in Fig. 5.3 indicates that the two characteristic dynamic processes of the bulk liquid, that are freezing of the liquid and the cation endgroup dynamics at distinct temperatures $T = 300\,\mathrm{K}$ and $T = 180\,\mathrm{K}$, are strongly interweaved in the confined state. Beyond this qualitative assessment, publication [45] shows that already these data provide a quite comprehensive and quantitative understanding of the confinement-induced alteration of the molecular mobility in comparison to the bulk.

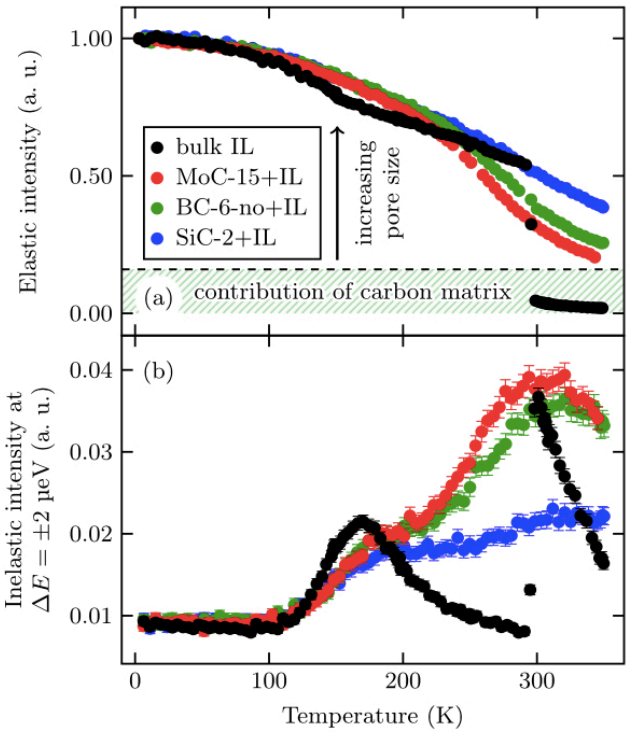

Figure 5.3: Fixed window scans in a temperature range from 2 K - 355 K with a heating rate of $1\,\mathrm{K\,min^{-1}}$ for the ionic liquid in bulk (black symbols) and in nanoconfinement of different pore sizes (red, green, blue symbols). Sec. 2.1.5 provides more details on the various samples. The scattering intensity is averaged over a Q range from $0.44\,\mathrm{Å^{-1}}$ - $1.90\,\mathrm{Å^{-1}}$: (a) Elastic fixed window scans with $\Delta E = \hbar\omega = 0\,\mu\mathrm{eV}$; (b) inelastic fixed window scans at an energy transfer of $\Delta E = \pm 2\,\mu\mathrm{eV}$. Reprinted from Ref. [45] under CCA 4.0 International.

A complementary, more detailed analysis of full energy transfer spectra $I(Q,\omega)$ recorded at FOCUS and IN16B at selected temperatures T applies a model similar to Eq. (5.10). The combined data from both instruments reveal two translational diffusive processes on different time scales and localized motions of the cation endgroup. Diffusion is found to be considerably slower than in the bulk liquid and shows a decrease of the respective self-diffusion coefficients with decreasing nanopore size. Different thermal activation energies for molecular self-diffusion in nanoporous carbons with similar pore size indicate the importance of pore morphology on the molecular mobility, beyond the pure degree of confinement. In spite of the dynamic slowing down the study shows that the temperature range of the liquid state upon nanoconfinement is remarkably extended to much lower temperatures, which is beneficial for potential technical applications of such systems. This last observation is

obviously on par with the results of chapter 4 as well as the preceding Sec. 5.2.1.

5.3 Phonons

Several studies precede this section that are concerned with some sort of soft matter, which is either confined in a mesoporous host or at least interacts with nanosculptured substrates. Less attention has been paid in the thesis so far to the structured substrates itself. The subsequently discussed studies [38] and [39] mark an overdue change in this paradigm by focusing on the mesoporous materials themselves as a form of nanostructured matter that is worth the attention.

5.3.1 Porous Silicon: Debye Regime

Key publication [38] presents a comprehensive scattering study of pSi. Neutron and X-ray scattering experiments combined elucidate the structure of and the one-phonon dynamics in electrochemically etched, porous silicon membranes with pores roughly 8 nm across. The formidable challenge that discussed inelastic neutron scattering experiments require a macroscopic amount of crystalline pSi is readily overcome by synthesizing dozens of membranes to form a stacked ensemble with well aligned crystallographic directions at a mosaicity below 1° (→ [38]).
Inelastic cold neutron scattering experiments [193] performed at the triple-axis spectrometer FLEXX (Helmholtz-Zentrum Berlin, Germany) [194] reveal the phonon energy-momentum relation or equivalently the phonon dispersion $\omega(\vec{q})$ of the nanostructured, single crystalline samples in the linear Debye regime ($\omega = v^{[hkl]}|\vec{q}|$) for energy transfers up to 4 meV (→ Fig. 5.4). They in particular probe in pSi the acoustic phonon dispersion in the high symmetry directions [001], [110], and [111] for longitudinal (L) and transverse (T) modes.
It is the intimate relation between sound velocities $v^{[hkl]}$ and the components of the stiffness tensor c_{ij} (→ [38]) that allows for a thorough characterization of the samples' elasticity. Eq. (5.12) quantifies this relation for a cubic structure [195] such as the one evident in elastic neutron scattering experiments on pSi (→ Fig. 4.1). ρ refers to the Si mass density. As the two transverse modes in the [110] direction are not degenerate the symbol || indicates explicitly a phonon polarization in the probed scattering plane.

$$\begin{aligned}
v_L^{[100]} &= (\frac{c_{11}}{\rho})^{1/2} \\
v_T^{[100]} &= (\frac{c_{44}}{\rho})^{1/2} \\
v_L^{[110]} &= (\frac{c_{11}+c_{12}+2c_{44}}{2\rho})^{1/2} \\
v_{T,\parallel}^{[110]} &= (\frac{c_{44}}{\rho})^{1/2} \\
v_L^{[111]} &= (\frac{c_{11}+2c_{12}+4c_{44}}{3\rho})^{1/2} \\
v_T^{[111]} &= (\frac{c_{11}-c_{12}+c_{44}}{3\rho})^{1/2}.
\end{aligned} \tag{5.12}$$

As a main result of the data analysis, a modified phonon dispersion characterized by systematically reduced sound velocities $v^{[hkl]}$ (→ Fig. 5.4) manifests itself in

altered elastic properties of pSi when compared to bulk silicon (bSi). For instance, the modified sound velocities translate into smaller Young moduli, e.g. 108 GPa = $Y^{pSi}_{[111]} < Y^{bSi}_{[111]} = 130$ GPa in agreement with recent studies on the elastic response of pSi upon water adsorption [3].

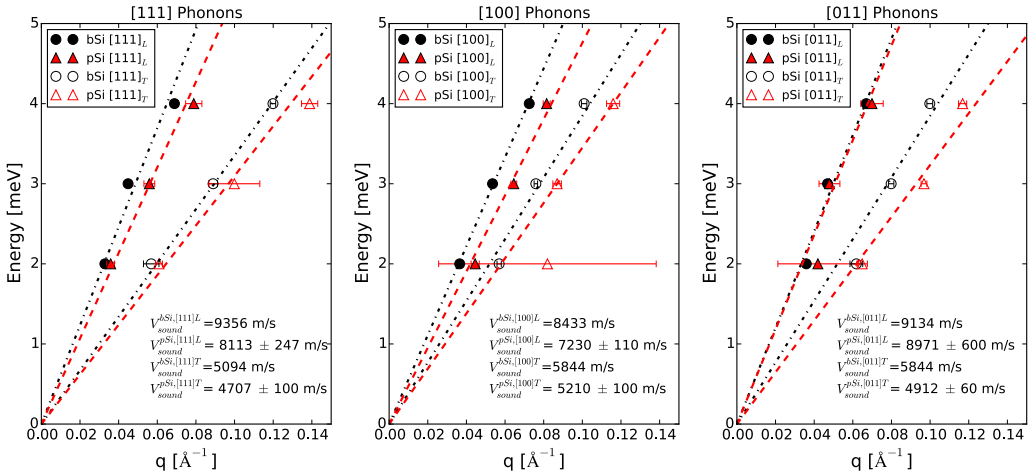

Figure 5.4: Phonon dispersion of pSi and bSi in the linear Debye regime. From left to right, symbols represent $[111]_{L/T}$, $[100]_{L/T}$, and $[011]_{L/T}$ phonons. Dashed lines illustrate the linear dispersion relation close to the center of the Brillouin zone. For bSi the slopes of the dispersions translate exactly into the literature values for respective sound velocities. Bulk data were used to reliably calibrate the instrumental offset close to the Brillouin zone center. The slopes of the dispersions for the nanostructured sample were obtained by linear least squares fitting and provide the sound velocities in pSi. Shown data are corrected for the instrumental offset. Reprinted with permission from Ref. [38]. Copyright 2017 Elsevier.

In publication [38], I interpret the apparent phonon softening in the Debye regime as an intrinsic property of the pSi skeleton putting it in contrast to properties of the compound, which consists of Si and pore space. This interpretation motivated by the wavelength $\lambda = 2\pi/q$ of the studied phonons between 2 nm - 10 nm is refined in the subsequently described study [39]. There, phonons are probed closer to the Brillouin zone boundary and the experiments become even more sensitive to microscopic properties rather than to volumetric compound averages.

5.3.2 Porous Silicon: Brillouin Zone Boundary

The article [39] presents inelastic thermal neutron scattering experiments probing the phonon dispersion in mesoporous silicon with pores 8 nm across. Scattering studies performed at spectrometer PUMA (Heinz Maier-Leibnitz Zentrum, Germany) [196] reveal the energy-momentum relation $\omega(\vec{q})$ for transverse and longitudinal phonons along the high symmetry directions $\overline{\Gamma L}$, $\overline{\Gamma K}$ and $\overline{\Gamma X}$, that are the crystallographic [111], [110] and [001] directions. The experiments are an extension of the cold neutron scattering studies discussed in key publication [38] towards the Brillouin zone boundary.
The dispersion in the phonon energy range between 4 meV - 35 meV (→ Fig. 5.5) unambiguously proves that the phonon group velocities $\vec{v}_g = \nabla\omega(\vec{q})$ in highly-crystalline silicon are not modified by nanostructuring down to sub-10 nanometer length scales. Modeling the dispersion with the Born-von-Kármán expression for

Table 5.1: Elastic moduli and uniaxial Young moduli for pSi and bSi as obtained from inelastic thermal neutron scattering experiments. Reprinted with permission from Ref. [39]. Copyright 2021 Elsevier.

	c_{11} [GPa]	c_{12} [GPa]	c_{44} [GPa]	$Y^{[100]}$ [GPa]	$Y^{[110]}$ [GPa]	$Y^{[111]}$ [GPa]
bSi	181 ± 1	68 ± 2	69 ± 1	145 ± 2	162 ± 1	169 ± 1
pSi	178 ± 2	73 ± 3	69 ± 1	135 ± 5	160 ± 2	170 ± 1.5

linear chains of lattice planes [197]

$$\omega(q) = \sqrt{\sum_{i=1}^{\infty} D_i(1 - cos(qia))} \tag{5.13}$$

allows first inferring the sound velocities as low-q limit of the group velocities and secondly the elastic constants as already discussed in the preceding section and publication [38]. Here, D_i is the "'spring constant per mass unit" between i-th nearest neighbor planes and a the distance between nearest neighbors.
This analysis scheme shows that on the sub-10 nanometer length scales, there is apparently no effect of structuring on the elastic moduli of the silicon skeleton in pSi (→ Table 5.1). No evidence can be found for phonon-softening in topologically complex, geometrically disordered mesoporous silicon putting it in contrast to silicon nanotubes and nanoribbons [2, 198].
This result is only on interpretational grounds a contradiction to the findings reported in [38]. In the latter article, phonons with wavelengths between 2 nm - 10 nm are utilized to determine the elasticity of pSi. The given interpretation assumes that I probe dominantly the properties of the pSi-skeleton itself and not a compound average. Consequently, a sizable phonon-softening is inferred for the skeleton. The basic assumption on which this interpretation relies on is however retrospectively not correct.
The experiments with the probed length scales between 2 nm - 10 nm return clearly no compound averages for the material in the continuum limit ($q \to 0$, $\lambda \to \infty$) as evident from a comparison with the "macroscopic" studies by Aliev and Andrews [199, 200]. Unfortunately, the experiments do not yet assert the characteristics solely of the skeleton itself either.
The cold neutron scattering experiments presented in Ref. [38] start the transition from microscopic probes like thermal neutron scattering to macroscopic probes like acoustic transmission spectroscopy. This troubling and admonishing tale of length scale dependent experimental results is unfortunately not new and known from diffusion experiments in confinement [201, 202] where different probes seemingly give different answers to the same question.
The inelastic neutron scattering studies presented in [38] and [39] are significant steps towards a thorough understanding of the influence of the pSi nanostructure on the phonon dynamics. But there is more to the story. Macroscopic thermal transport measurements evidence a strongly reduced thermal conductivity in pSi [203] and therefore indicate by a process of elimination, which excludes now obviously a modified phonon dispersion as origin, that the inherent nanostructure of pSi affects phonon scattering rates. Deeper insights into the pSi phonon dynamics are consequently expected from studies that probe the phonon lifetimes or equivalently the

scattering rates directly (→ Sec. 5.1.3). Neutron resonance spin-echo spectroscopy appears as appropriate scattering technique to gain these insights [204]. It is however experimentally very challenging and comes along with new demands for sample quality and quantity. So this topic is left for now, with the prospect of tempting studies ahead.

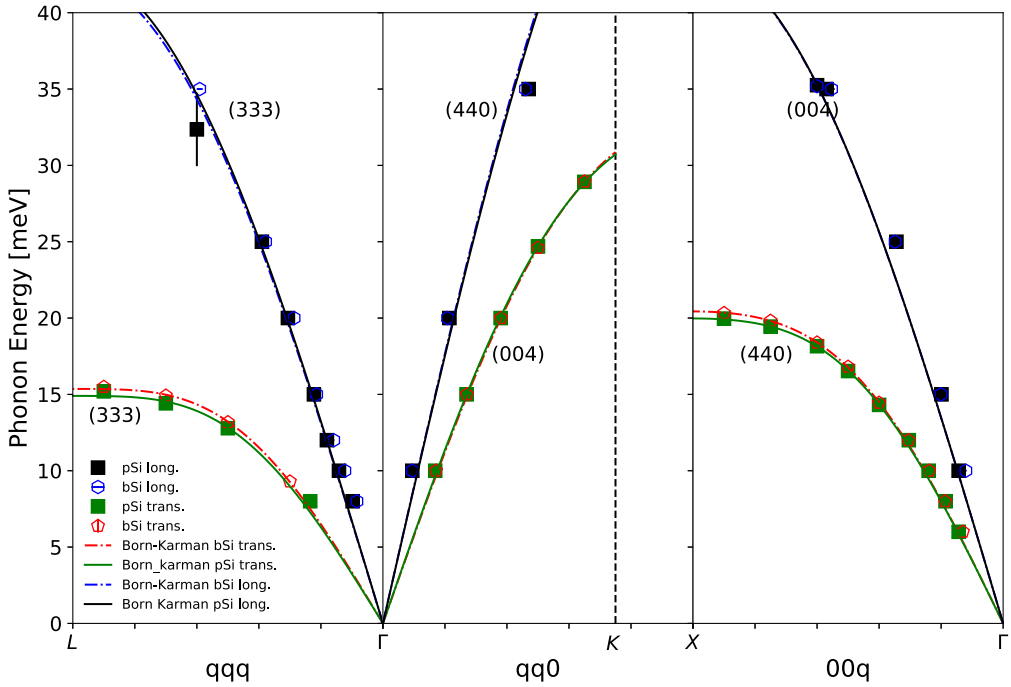

Figure 5.5: Dispersion of longitudinal and transverse phonons in bSi (open symbols) and in porous silicon (filled symbols) along high symmetry directions [100]($\overline{\Gamma L}$), [110] ($\overline{\Gamma K}$) and [111] ($\overline{\Gamma X}$): Labels indicate the Bragg reflections at which the phonons were measured. Colored lines (dashed, solid) represent Born-von-Kármán approximations of the different dispersion branches. Reprinted with permission from Ref. [39]. Copyright 2021 Elsevier.

Beyond the insights into the elasticity of pSi, the performed investigations demonstrate the potential of neutron scattering techniques to probe the phonon dispersion of nanostructured, crystalline materials. Employed techniques overcome the limitations of other techniques like Brillouin scattering and acoustic transmission spectroscopy [199, 200], which only provide information close to the high-symmetry Γ-point and as such only allow inferring long-wavelength averaged ($q \to 0$) material properties. This experimental approach is of particular interest in the field of nanophononics or thermoelectrics where phonon gap engineering or phonon dispersion engineering in general is expected to play an important role to improve or tailor device performances.

5.4 Thermal Conductivity of SPS-pSi and SPS-Si

Key publication [41] presents a detailed study of the thermal conductivity of SPS-Si and SPS-pSi samples (→ Sec. 2.1.4) with well characterized porosity, domain size and pore-pore distance distributions. The synthesis strategy to prepare these nanostructured bulk monoliths relies on metal-induced crystallization in bulk sam-

ples and builds partially on the porosity inherent to the nanoporous starting material (→ Sec. 2.1.1) prior to spark plasma sintering.
Quantitative SEM image analysis as depicted in Fig. 5.6 demonstrates morphology control of SPS-(p)Si samples synthesized by different ultra-sonic dispersion methodologies. Since the high porosity of pSi is maintained after SPS processing and macroscopic grain growth is suppressed upon sintering, both nanometer sized domains and porosity simultaneously lead to a particularly strong reduction of thermal conductivity in SPS-pSi samples (→ [41]).

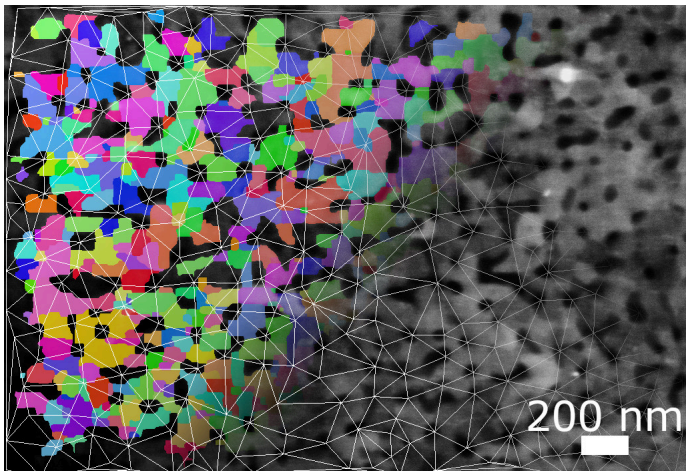

Figure 5.6: SEM image of a SPS-pSi sample.The line grid shows the pore network. Colored regions indicate domains as identified by quantitative image analysis. The graphic is a courtesy of Danny Kojda (HZB).

Temperature-dependent thermal conductivity measurements are the key to understand the thermal transport in SPS-(p)Si samples on a microscopic level. They allow disentangling porosity and domain size effects to explain the reduction of the thermal conductivity in SPS-(p)Si samples compared to bulk. Fig. 5.7 exhibits exemplarily the thermal conductivity for various SPS-pSi samples.
The heart of the data analysis is Eq. (5.14) for the T-dependent thermal conductivity.

$$\lambda_{\text{eff}}(T) = \lambda_r \lambda_0 = \lambda_r \left(\frac{k_B^2 \pi}{6} T \right) \int_0^{\omega_0} \frac{4}{3} \Lambda(\omega) M_{ph}(\omega) W_{ph}(\omega) d\omega \tag{5.14}$$

It incorporates the window function reminiscent of the Bose-Einstein distribution of excited phonon modes

$$W_{ph}(\omega) = \frac{3}{\pi^2 k_B T} \left(\frac{\hbar\omega}{k_B T} \right)^2 \left(e^{\frac{\hbar\omega}{k_B T}} - 1 \right)^{-2} e^{\frac{\hbar\omega}{k_B T}}, \tag{5.15}$$

and the mode function

$$M_{ph}(\omega) = \frac{\pi}{2} DOS(\omega) v_g(\omega), \tag{5.16}$$

which depends on the phonon density of states $DOS(\omega)$ and the phonon group velocity $v_g(\omega)$. The phonon mean free path Λ is the important parameter for the analysis of the conductivity data. For more details on the model and its application to the data, the reader might consult Ref. [41] and its supplementary information available online.

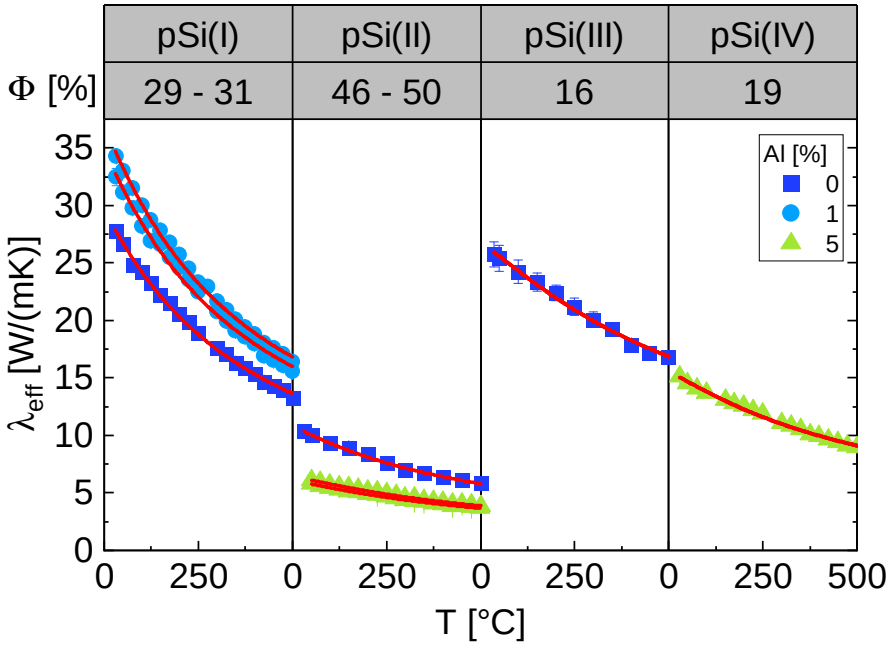

Figure 5.7: The effective thermal conductivity of sintered pSi. Red solid lines represent non-linear least square fits applying the model described in the text with λ_r and Λ_D as the only free parameters. Reprinted from Ref. [41] under CC-BY.

Eq. (5.14) represents a modified Landauer/Lundstrom model [205, 206] to describe the temperature-dependent thermal conductivity ($\lambda_{eff}(T)$). It disentangles the effects of porosity (λ_r) and phonon scattering lengths (λ_0) on the phononic heat transport. The unitless relative conductivity λ_r accounts for the porosity [207] and is motivated by effective medium models [208, 209]. The thermal conductivity λ_0 incorporates the combined effect of different phonon scattering mechanisms through the phonon mean free path Λ.
The phonon mean free path accounts for impurity scattering, boundary scattering, umklapp scattering and scattering on the nanostructure

$$\Lambda_{tot}^{-1} = \Lambda_{imp}^{-1} + \Lambda_{boundary}^{-1} + \Lambda_{umklapp}^{-1} + \Lambda_{D}^{-1}. \tag{5.17}$$

Treated as independent scattering channels, the four contributions are combined via Matthiesen's rule. The first three contributions to Λ_{tot} are known from bulk silicon, the last contribution is a free model parameter that is estimated for the various samples by non-linear least squares approximation of the data (Fig. 5.7).
Fig. 5.8a compares the relative thermal conductivity λ_r to several effective medium models [209]. A favorable agreement is found with the model from Kirkpatrick, which introduces a percolation threshold in the porosity for the thermal conductance in porous materials. This threshold is about 60 % for the series of synthesized samples.
Fig. 5.8b exhibits an excellent agreement between the phonon mean free path as extracted from the non-linear least squares approximation and an effective length scale characteristic for the sintered SPS-(pSi) samples $\Lambda_{eff,SEM}$. This effective length scale is obtained from quantitative image analysis of the SEM micrographs (→ [41] & Fig. 2.5) and combines average domain sizes with average pore-pore distances by

means of Matthiessen's rule

$$\Lambda_{\mathrm{eff,SEM}}^{-1} = \Lambda_{\mathrm{D,SEM}}^{-1} + \Lambda_{\mathrm{pore,SEM}}^{-1}. \tag{5.18}$$

The outlined model is applicable to a broad range of materials based on porous nanomaterials beyond the specific material system studied in the present work. Due to the close correspondence of heat transport by phonons to charge carrier transport, the proposed model provides a pathway to a thorough understanding of electronic transport in porous nanostructured material systems as well.

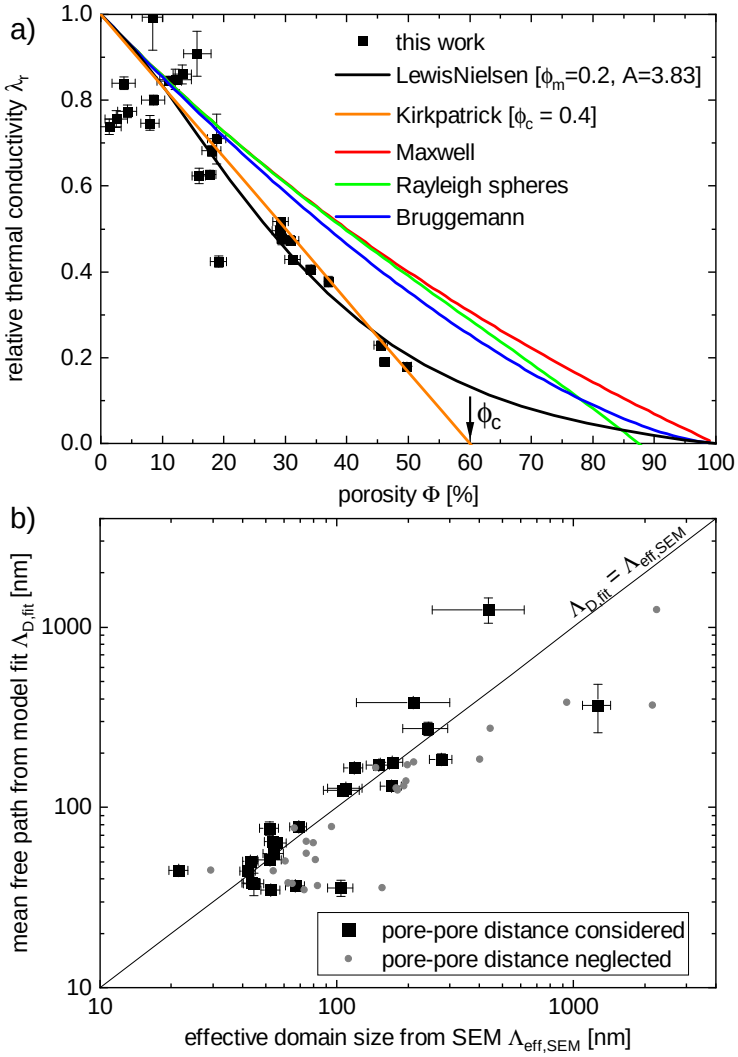

Figure 5.8: a) Extracted relative thermal conductivity λ_r as function of the porosity Φ is compared to effective medium models like the Maxwell model (red), the Rayleigh model for spherical pores (green), the Bruggemann model (blue) and the Lewis-Nielsen model (black) for different packing fractions ϕ_m and aspect ratios A (solid, dashed, dotted). b) Mean free path $\Lambda_{\mathrm{D,fit}}$ extracted from fitting the temperature-dependent effective thermal conductivity as function of the effective domain size $\Lambda_{\mathrm{eff,SEM}}$. Gray points show the mean free path only taking the domain size into account. The solid line shows the identity $\Lambda_{\mathrm{D,fit}} = \Lambda_{\mathrm{eff,SEM}}$. Reprinted from Ref. [41] under CC-BY.

Chapter 6

Conclusion

The studies presented in this thesis address foremost three key questions. How do simple, molecular liquids interact with nanostructured materials? How does confinement affect crystal structures and structural phase transitions? What is the impact of nanostructuring on the dynamic behavior of matter?
I addressed the first question intensively in nanowetting studies that employed X-ray scattering techniques. Synchrotron based small-angle scattering was utilized to study the wetting of molecular liquids on nanosculptured Si surfaces and inside mesoporous SBA-15 substrates. From these investigations, I like to emphasize two results.
The theoretical predictions of the Augmented Young-Laplace equation were experimentally validated on sub-10 nanometer length-scales. The importance, of long range dispersion forces for nanoscale wetting became evident. Such insights, I expect to be of fundamental importance for emerging nanoimprinting and nanofluidic applications.
Subtle morphological characteristics of the porous host were revealed in my wetting studies on SBA-15. The formation of stable nanobubbles in SBA-15-confined liquids was evidenced by X-ray scattering measurements. Nanobubbles were caused by regular pore corrugations along the tubular nanochannel, which themselves originate in a hydrodynamic instability during the synthesis of SBA-15. Although a result of more fundamental relevance, I like to imply a more pragmatic importance for templating applications, which utilize SBA-15 substrates.
The second question was mainly addressed in a series of neutron scattering studies on pore-confined matter. Two principal mechanisms were identified in these experiments to affect crystal growth in confinement.
A nanoscale version of Bridgeman growth prefers in tubular pores the nucleation of crystallites that align with the fast growing crystallographic direction along the pore channel. This causes strongly textured confined solids in anisotropic pore networks. I observed this crystallization scenario in AAO-confined solid oxygen, nitrogen and rare gases.
Epitaxial overgrowth was found as a rare crystallization mechanism during the solidification of deuterium and nitrogen in porous silicon. The highly crystalline nature of pSi imprints two-fold on the pore-confined solid. Not only is the stable hcp bulk phase for D_2 and N_2 abandoned in favor of a cubic phase. Rather, nanocrystals inside the pores align perfectly with the cubic quasi-single-crystalline structure of the pSi host. They form an ensemble of highly orientated crystals.
My thesis discusses dynamics in nanostructured matter in a three-fold manner. I investigated stochastic motions of individual molecules in confined liquids, collective

atomic motions that are phonons in pSi and diffusive heat transport in spark-plasma-sintered Si.
Quasi-elastic neutron scattering techniques helped to elucidate stochastic motions in molecular liquids upon nanoconfinement. Translational diffusion could be discerned from faster molecular rotations in pSi-confined hexane. Mobile molecules close to the pore center stood opposite immobile molecules close to the pore walls.
Ionic liquids exhibited a pore-size dependent slowing down of stochastic dynamics upon confinement in porous carbon. This insight bears some inherent importance for technological applications such as super capacitors that microscopically rely on ion diffusion during charging-discharging cycles.
Coherent inelastic neutron scattering experiments allowed probing the elasticity of the silicon skeleton in pSi. It was possible to overcome the limitations of other techniques like Brillouin scattering that probe compound averages in the sense of effective medium models. A surprisingly robust phonon dispersion in nanostructured pSi was found. An intriguing absence of phonon softening down to 10 nm length-scales contrasted expectations arising from the observation of such effects in nanowires or nanoribbons.
Thermal transport measurements and quantitative analysis of SEM micrographs were essential to develop a reliable model for the temperature dependent thermal conductivity of nanostructured, spark-plasma-sintered Si samples. The proposed model distinguishes between a reduction in thermal conductivity due to porosity in the sense of effective medium approaches and the reduction due to additional phonon scattering at nanostructural features such as grain boundaries or pores.
The presented studies cover of course only selected aspects of the cited key questions. No claim can be raised to answer them in their entire complexity and generality. As usually seems to be the case, each study answers some questions but raises new ones and inevitably points towards new interesting projects. Consequently, this thesis should conclude with addressing one final question. What lies ahead?
The thermal conductivity studies on SPS samples as well as the phonon dispersion measurements on pSi make the attempt to understand macroscopic heat transport in nanostructured systems on a microscopic level. Gaining such an understanding is not only of academic interest. Rather, it appears as a prerequisite to smartly optimize nanostructured materials for selected applications such as heat management or thermoelectrics. It is consequently tempting to extend such studies to other transport phenomena and other members of this diverse material class.
One notices momentarily an increasing interest in stimulus responsive nanostructured systems because they naturally trigger novel and visionary applications. For instance, the mechano-elastic response of pSi upon liquid absorption or desorption is considered for actuation devices or energy harvesting. It is the necessity to link microscopic and macroscopic processes to achieve a comprehensive understanding of such responsive effects that suggests a multitude of fascinating studies.
Last but not least, it is appealing to consider a change in paradigm. So far, I took often the singular perspective and studied either condensed matter in confinement or mesoporous materials themselves. It might be even more interesting and pleasing to see whether matter and porous host combine to novel hybrids that exhibit synergistic properties that go beyond compound averages.
That said, everything must end and the time seems right to finish this thesis for good. Closing with a profound insight for the future, I might say: "There is still a

lot to be done, there is a lot to be learned, let's do it" or more directly "let's have some fun".

Bibliography

[1] E. Rolley, N. Garroum, and A. Grosman. "Using capillary forces to determine the elastic properties of mesoporous materials". In: *Physical Review B* 95.6 (Feb. 2017), p. 064106.

[2] Lin Yang, Yang Yang, Qian Zhang, Yin Zhang, Youfei Jiang, Zhe Guan, Matthew Gerboth, Juekuan Yang, Yunfei Chen, D. Greg Walker, Terry T. Xu, and Deyu Li. "Thermal conductivity of individual silicon nanoribbons". In: *Nanoscale* 8.41 (2016), pp. 17895–17901.

[3] Gennady Y. Gor, Luca Bertinetti, Noam Bernstein, Tommy Hofmann, Peter Fratzl, and Patrick Huber. "Elastic response of mesoporous silicon to capillary pressures in the pores". In: *Applied Physics Letters* 106.26 (2015), p. 261901.

[4] Gennady Y. Gor and Alexander V. Neimark. "Adsorption-Induced Deformation of Mesoporous Solids: Macroscopic Approach and Density Functional Theory". In: *Langmuir* 27.11 (2011), pp. 6926–6931.

[5] A. Vega-Flick, N. W. Pech-May, F. Cervantes-Alvarez, J. O. Estevez, and J. J. Alvarado-Gil. "Thermal conductivity reduction in highly doped mesoporous silicon: The effect of nano-crystal formation". In: *Journal of Applied Physics* 124.08 (Aug. 2018), p. 085101.

[6] R.J. Martín-Palma, H. Cabrera, B. Martín-Adrados, D. Korte, E. Pérez-Cappe, Y. Mosqueda, M.A. Frutis, and E. Danguillecourt. "Thermoelectric properties of nanostructured porous silicon". In: *Materials Research Express* 5.1 (2018), p. 015004.

[7] Katerina Valalaki. "Study of thermoelectric properties and thermal isolation of porous Si and nanocrystalline Silicon". PhD thesis. 2016.

[8] Y. Lubianiker and I. Balberg. "Two Meyer-Neldel Rules in Porous Silicon". In: *Physical Review Letters* 78.12 (Mar. 1997), pp. 2433–2436.

[9] Kathrin Sentker, Arne W. Zantop, Milena Lippmann, Tommy Hofmann, Oliver H. Seeck, Andriy V. Kityk, Arda Yildirim, Andreas Schönhals, Marco G. Mazza, and Patrick Huber. "Quantized Self-Assembly of Discotic Rings in a Liquid Crystal Confined in Nanopores". In: *Physical Review Letters* 120.6 (Feb. 2018), p. 067801.

[10] Kathrin Sentker, Arda Yildirim, Milena Lippmann, Arne W. Zantop, Florian Bertram, Tommy Hofmann, Oliver H. Seeck, Andriy V. Kityk, Marco G. Mazza, Andreas Schönhals, and Patrick Huber. "Self-assembly of liquid crystals in nanoporous solids for adaptive photonic metamaterials". In: *Nanoscale* 11.48 (2019), pp. 23304–23317.

[11] Sylwia Całus, Andriy V. Kityk, and Patrick Huber. "Molecular ordering of the discotic liquid crystal HAT6 confined in mesoporous solids". In: *Microporous and Mesoporous Materials* 197 (Oct. 2014), pp. 26–32.

[12] Patrick Huber. *Kondensierte Materie in beschränkten Geometrien*. Habilitationsschrift Universität des Saarlandes. 2007.

[13] Patrick Huber. "Soft matter in hard confinement: phase transition thermodynamics, structure, texture, diffusion and flow in nanoporous media". In: *Journal of Physics: Condensed Matter* 27.10 (2015), p. 103102.

[14] Michele Amato, Stefano Ossicini, Enric Canadell, and Riccardo Rurali. "Preferential Positioning, Stability, and Segregation of Dopants in Hexagonal Si Nanowires". In: *Nano Letters* (Jan. 2019).

[15] Ibrahim N. Qader and M. S. Omar. "Carrier concentration effect and other structure-related parameters on lattice thermal conductivity of Si nanowires". In: *Bulletin of Materials Science* 40.3 (2017), pp. 599–607.

[16] Danny Kojda, Rüdiger Mitdank, Stefan Weidemann, Anna Mogilatenko, Zhi Wang, Johannes Ruhhammer, Michael Kroener, William Töllner, Peter Woias, Kornelius Nielsch, and Saskia F. Fischer. "Surface effects on thermoelectric properties of metallic and semiconducting nanowires". In: *Physica Status Solidi (a)* 213.3 (2016), pp. 557–570.

[17] Lingzheng Bu, Shaojun Guo, Xu Zhang, Xuan Shen, Dong Su, Gang Lu, Xing Zhu, Jianlin Yao, Jun Guo, and Xiaoqing Huang. "Surface engineering of hierarchical platinum-cobalt nanowires for efficient electrocatalysis". In: *Nature Communications* 7 (June 2016), p. 11850.

[18] T. Hofmann, D. Wallacher, P. Huber, R. Birringer, K. Knorr, A. Schreiber, and G. H. Findenegg. "Small-Angle X-Ray Diffraction of Kr in Mesoporous Silica: Effects of Microporosity and Surface Roughness". In: *Phys. Rev. B* 72 (2005), p. 064122.

[19] D. Wallacher, N. Künzner, D. Kovalev, N. Knorr, and K. Knorr. "Capillary Condensation in Linear Mesopores of Different Shape". In: *Physical Review Letters* 92.19 (May 2004), p. 195704.

[20] Victor P. Soprunyuk, Dirk Wallacher, Patrick Huber, Klaus Knorr, and Andriy V. Kityk. "Freezing and melting of Ar in mesopores studied by optical transmission". In: *Phys. Rev. B* 67 (14 Apr. 2003), p. 144105.

[21] Tommy Hofmann. "Nanostructured Energy Materials: From Organic Photovoltaic to Hybrid Thermoelectrics". In: *Soft Matter and Biomaterials on the Nanoscale*. World Scientific, Feb. 2020, pp. 435–479.

[22] Albrecht Petzold, Anika Juhl, Jonas Scholz, Boris Ufer, Günter Goerigk, Michael Fröba, Matthias Ballauff, and Simone Mascotto. "Distribution of Sulfur in Carbon/Sulfur Nanocomposites Analyzed by Small-Angle X-ray Scattering". In: *Langmuir* 32.11 (Mar. 2016), pp. 2780–2786.

[23] Xinhui Lu, Htay Hlaing, Chang-Yong Nam, Kevin G. Yager, Charles T. Black, and Benjamin M. Ocko. "Molecular Orientation and Performance of Nanoimprinted Polymer-Based Blend Thin Film Solar Cells". In: *Chemistry of Materials* 27.1 (Jan. 2015), pp. 60–66.

[24] Jonathan E. Allen, Kevin G. Yager, Htay Hlaing, Chang-Yong Nam, Benjamin M. Ocko, and Charles T. Black. "Enhanced charge collection in confined bulk heterojunction organic solar cells". In: *Applied Physics Letters* 99.16 (2011), p. 163301.

[25] Yan Qiao and Chang Ming Li. "Nanostructured catalysts in fuel cells". In: *Journal of Materials Chemistry* 21.12 (2011), pp. 4027–4036.

[26] J. Chmiola, G. Yushin, Y. Gogotsi, C. Portet, P. Simon, and P. L. Taberna. "Anomalous Increase in Carbon Capacitance at Pore Sizes Less Than 1 Nanometer". In: *Science* 313.5794 (2006), pp. 1760–1763.

[27] Yanwu Zhu, Shanthi Murali, Meryl D. Stoller, K. J. Ganesh, Weiwei Cai, Paulo J. Ferreira, Adam Pirkle, Robert M. Wallace, Katie A. Cychosz, Matthias Thommes, Dong Su, Eric A. Stach, and Rodney S. Ruoff. "Carbon-Based Supercapacitors Produced by Activation of Graphene". In: *Science* 332.6037 (2011), pp. 1537–1541.

[28] Kisung Chae, Seoung-Hun Kang, Seon-Myeong Choi, Duck Young Kim, and Young-Woo Son. "Enhanced Thermoelectric Properties in a New Silicon Crystal Si24 with Intrinsic Nanoscale Porous Structure". In: *Nano Letters* (July 2018).

[29] Woochul Kim. "Strategies for engineering phonon transport in thermoelectrics". In: *J. Mater. Chem. C* 3 (40 2015), pp. 10336–10348.

[30] J. de Boor, D. S. Kim, X. Ao, M. Becker, N. F. Hinsche, I. Mertig, P. Zahn, and V. Schmidt. "Thermoelectric properties of porous silicon". In: *Applied Physics A* 107.4 (2012), pp. 789–794.

[31] G. Jeffrey Snyder and Eric S. Toberer. "Complex thermoelectric materials". In: *Nature Publishing Group* 7.2 (Feb. 2008), pp. 105–114.

[46] J. Rouquerol, D. Avnir, C. W. Fairbridge, D. H. Everett, J. M. Haynes, N. Pernicone, J. D. F. Ramsay, K. S. W. Sing, and K. K. Unger. "Recommendations for the characterization of porous solids (Technical Report)". In: *Pure and Applied Chemistry* 66.8 (1994), pp. 1739–1758.

[47] V. Lehmann, R. Stengl, and A. Luigart. "On the morphology and the electrochemical formation mechanism of mesoporous silicon". In: *Materials Science and Engineering: B* 69-70 (2000), pp. 11–22.

[48] A. Uhlir Jr. "Electrolytic Shaping of Germanium and Silicon". In: *Bell System Technical Journal* 35.2 (Mar. 1956), pp. 333–347.

[49] P. Gupta, V. L. Colvin, and S. M. George. "Hydrogen desorption kinetics from monohydride and dihydride species on silicon surfaces". In: *Phys. Rev. B* 37 (14 1988), pp. 8234–8243.

[50] A.C. Dillon, P. Gupta, M.B. Robinson, A.S. Bracker, and S.M. George. "FTIR studies of water and ammonia decomposition on silicon surfaces". In: *Journal of Electron Spectroscopy and Related Phenomena* 54-55 (1990), pp. 1085–1095.

[51] Rolfe C. Erson, Richard S. Muller, and Charles W. Tobias. "Investigations of porous silicon for vapor sensing". In: *Sensors and Actuators A: Physical* 23.1 (1990), pp. 835–839.

[52] A. C. Dillon, M. B. Robinson, M. Y. Han, and S. M. George. "Diethylsilane Decomposition on Silicon Surfaces Studied Using Transmission FTIR Spectroscopy". In: *Journal of The Electrochemical Society* 139.2 (1992), pp. 537–543.

[53] M.J. Sailor. *Porous Silicon in Practice: Preparation, Characterization and Applications*. Wiley, 2012.

[54] V. Lehmann and U. Gösele. "Porous silicon formation: A quantum wire effect". In: *Applied Physics Letters* 58.8 (1991), pp. 856–858.

[55] L. T. Canham. "Silicon quantum wire array fabrication by electrochemical and chemical dissolution of wafers". In: *Applied Physics Letters* 57.10 (1990), pp. 1046–1048.

[56] Maziar Ashuri, Qianran He, and Leon L. Shaw. "Silicon as a potential anode material for Li-ion batteries: where size, geometry and structure matter". In: *Nanoscale* 8.1 (2016), pp. 74–103.

[57] Andreas Janshoff, Keiki-Pua S. Dancil, Claudia Steinem, Douglas P. Greiner, Victor S. -Y. Lin, Christian Gurtner, Kianoush Motesharei, Michael J. Sailor, and M. Reza Ghadiri. "Macroporous p-Type Silicon Fabry-Perot Layers. Fabrication, Characterization, and Applications in Biosensing". In: *Journal of the American Chemical Society* 120.46 (Nov. 1998), pp. 12108–12116.

[58] Leonora Velleman, Cameron James Shearer, Amanda Vera Ellis, Dusan Losic, Nicolas Hans Voelcker, and Joseph George Shapter. "Fabrication of self-supporting porous silicon membranes and tuning transport properties by surface functionalization". In: *Nanoscale* 2.9 (2010), pp. 1756–1761.

[59] S. H. C. Anderson, H. Elliott, D. J. Wallis, L. T. Canham, and J. J. Powell. "Dissolution of different forms of partially porous silicon wafers under simulated physiological conditions". In: *Physica Status Solidi (a)* 197.2 (May 2003), pp. 331–335.

[60] J. de Jong, R. G. H. Lammertink, and M. Wessling. "Membranes and microfluidics: a review". In: *Lab on a Chip* 6.9 (2006), pp. 1125–1139.

[61] Mingyuan Ge, Jiepeng Rong, Xin Fang, and Chongwu Zhou. "Porous Doped Silicon Nanowires for Lithium Ion Battery Anode with Long Cycle Life". In: *Nano Letters* 12.5 (May 2012), pp. 2318–2323.

[62] Hyunjung Kim, Byunghee Han, Jaebum Choo, and Jaephil Cho. "Three-Dimensional Porous Silicon Particles for Use in High-Performance Lithium Secondary Batteries". In: *Angewandte Chemie International Edition* 47.52 (Dec. 2008), pp. 10151–10154.

[63] Jan Hendrik Petermann, Dimitri Zielke, Jan Schmidt, Felix Haase, Enrique Garralaga Rojas, and Rolf Brendel. "19%-efficient and 43 μm-thick crystalline Si solar cell from layer transfer using porous silicon". In: *Progress in Photovoltaics: Research and Applications* 20.1 (Jan. 2012), pp. 1–5.

[64] P. Menna, G. Di Francia, and V. La Ferrara. "Porous silicon in solar cells: A review and a description of its application as an AR coating". In: *Solar Energy Materials and Solar Cells* 37.1 (1995), pp. 13–24.

[65] Jinyao Tang, Hung-Ta Wang, Dong Hyun Lee, Melissa Fardy, Ziyang Huo, Thomas P. Russell, and Peidong Yang. "Holey Silicon as an Efficient Thermoelectric Material". In: *Nano Letters* 10.10 (Oct. 2010), pp. 4279–4283.

[66] Stefano Mariani, Valentina Robbiano, Lucanos M. Strambini, Aline Debrassi, Gabriela Egri, Lars Dähne, and Giuseppe Barillaro. "Layer-by-layer biofunctionalization of nanostructured porous silicon for high-sensitivity and high-selectivity label-free affinity biosensing". In: *Nature Communications* 9.1 (2018), p. 5256.

[67] Valentina Robbiano, Giuseppe M. Paternò, Antonino A. La Mattina, Silvia G. Motti, Guglielmo Lanzani, Francesco Scotognella, and Giuseppe Barillaro. "Room-Temperature Low-Threshold Lasing from Monolithically Integrated Nanostructured Porous Silicon Hybrid Microcavities". In: *ACS Nano* 12.5 (May 2018), pp. 4536–4544.

[68] Christian R. Ocier, Neil A. Krueger, Weijun Zhou, and Paul V. Braun. "Tunable Visibly Transparent Optics Derived from Porous Silicon". In: *ACS Photonics* 4.4 (Apr. 2017), pp. 909–914.

[69] Anton Ressine, Irina Corin, Kerstin Järås, Ginevra Guanti, Cristiano Simone, György Marko-Varga, and Thomas Laurell. "Porous silicon surfaces –A candidate substrate for reverse protein arrays in cancer biomarker detection". In: *Electrophoresis* 28.23 (Dec. 2007), pp. 4407–4415.

[70] Chanseok Hong, Jungkeun Lee, Hongmei Zheng, Soon-Sun Hong, and Chongmu Lee. "Porous silicon nanoparticles for cancer photothermotherapy". In: *Nanoscale Research Letters* 6.1 (2011), p. 321.

[71] R. Busselez, R. Lefort, M. Guendouz, B. Frick, O. Merdrignac-Conanec, and D. Morineau. "Molecular dynamics of glycerol and glycerol-trehalose bioprotectant solutions nanoconfined in porous silicon". In: *The Journal of Chemical Physics* 130.21 (June 2009), p. 214502.

[72] R. Guégan, D. Morineau, R. Lefort, W. Béziel, M. Guendouz, L. Noirez, A. Henschel, and P. Huber. "Rich polymorphism of a rod-like liquid crystal (8CB) confined in two types of unidirectional nanopores". In: *The European Physical Journal E* 26.3 (July 2008), pp. 261–273.

[73] R. Guégan, D. Morineau, R. Lefort, A. Moréac, W. Béziel, M. Guendouz, J. -M. Zanotti, and B. Frick. "Molecular dynamics of a short-range ordered smectic phase nanoconfined in porous silicon". In: *The Journal of Chemical Physics* 126.6 (Feb. 2007), p. 064902.

[74] Wei Chen and Haroon Ahmed. "Fabrication of 5–7 nm wide etched lines in silicon using 100 keV electron-beam lithography and polymethylmethacrylate resist". In: *Applied Physics Letters* 62.13 (Mar. 1993), pp. 1499–1501.

[75] A. Küller, W. Eck, V. Stadler, W. Geyer, and A. Gölzhäuser. "Nanostructuring of silicon by electron-beam lithography of self-assembled hydroxybiphenyl monolayers". In: *Applied Physics Letters* 82.21 (May 2003), pp. 3776–3778.

[76] Chienliu Chang, Yeong-Feng Wang, Yoshiaki Kanamori, Ji-Jheng Shih, Yusuke Kawai, Chih-Kung Lee, Kuang-Chong Wu, and Masayoshi Esashi. "Etching submicrometer trenches by using the Bosch process and its application to the fabrication of antireflection structures". In: *Journal of Micromechanics and Microengineering* 15.3 (2005), pp. 580–585.

[77] Yuji Hirai, Hiroshi Yabu, Yasutaka Matsuo, Kuniharu Ijiro, and Masatsugu Shimomura. "Biomimetic bi-functional silicon nanospike-array structures prepared by using self-organized honeycomb templates and reactive ion etching". In: *Journal of Materials Chemistry* 20.48 (2010), pp. 10804–10808.

[78] Zhipeng Huang, Nadine Geyer, Peter Werner, Johannes de Boor, and Ulrich Gösele. "Metal-Assisted Chemical Etching of Silicon: A Review". In: *Advanced Materials* 23.2 (Jan. 2011), pp. 285–308.

[79] C. Chartier, S. Bastide, and C. Lévy-Clément. "Metal-assisted chemical etching of silicon in HF–H2O2". In: *Electrochimica Acta* 53.17 (2008), pp. 5509–5516.

[80] X. Li and P. W. Bohn. "Metal-assisted chemical etching in HF/H2O2 produces porous silicon". In: *Applied Physics Letters* 77.16 (Oct. 2000), pp. 2572–2574.

[81] Zailei Zhang, Yanhong Wang, Wenfeng Ren, Qiangqiang Tan, Yunfa Chen, Hong Li, Ziyi Zhong, and Fabing Su. "Scalable Synthesis of Interconnected Porous Silicon/Carbon Composites by the Rochow Reaction as High-Performance Anodes of Lithium Ion Batteries". In: *Angewandte Chemie International Edition* 53.20 (2014), pp. 5165–5169.

[82] R. E. Hummel and Sung-Sik Chang. "Novel technique for preparing porous silicon". In: *Applied Physics Letters* 61.16 (Oct. 1992), pp. 1965–1967.

[83] A. V. Kabashin and M. Meunier. "Fabrication of photoluminescent Si-based layers by air optical breakdown near the silicon surface". In: *Applied Surface Science* 186.1 (2002), pp. 578–582.

[84] X. G. Zhang. "Morphology and Formation Mechanisms of Porous Silicon". In: *Journal of The Electrochemical Society* 151.1 (Jan. 2004), pp. C69–C80.

[85] F. Keller, M. S. Hunter, and D. L. Robinson. "Structural Features of Oxide Coatings on Aluminum". In: *Journal of The Electrochemical Society* 100.9 (1953), p. 411.

[86] J. W. Diggle, Thomas C. Downie, and C. W. Goulding. "Anodic oxide films on aluminum". In: *Chemical Reviews* 69.3 (June 1969), pp. 365–405.

[87] G. E. Thompson and G. C. Wood. "Porous anodic film formation on aluminium". In: *Nature* 290.5803 (1981), pp. 230–232.

[88] Hideki Masuda and Kenji Fukuda. "Ordered Metal Nanohole Arrays Made by a Two-Step Replication of Honeycomb Structures of Anodic Alumina". In: *Science* 268.5216 (1995), pp. 1466–1468.

[89] Tomáš Lednický and Attila Bonyár. "Large Scale Fabrication of Ordered Gold Nanoparticle–Epoxy Surface Nanocomposites and Their Application as Label-Free Plasmonic DNA Biosensors". In: *ACS Applied Materials & Interfaces* 12.4 (Jan. 2020), pp. 4804–4814.

[90] Alejandra Ruiz-Clavijo, Olga Caballero-Calero, and Marisol Martín-González. "Revisiting anodic alumina templates: from fabrication to applications". In: *Nanoscale* 13.4 (2021), pp. 2227–2265.

[91] Spomenka Simovic, Dusan Losic, and Krasimir Vasilev. "Controlled drug release from porous materials by plasma polymer deposition". In: *Chemical Communications* 46.8 (2010), pp. 1317–1319.

[92] A. M. Mebed, Alaa M. Abd-Elnaiem, and Najm M. Al-Hosiny. "Electrochemical fabrication of 2D and 3D nickel nanowires using porous anodic alumina templates". In: *Applied Physics A* 122.6 (2016), p. 565.

[93] S. Z. Chu, K. Wada, S. Inoue, M. Isogai, Y. Katsuta, and A. Yasumori. "Large-Scale Fabrication of Ordered Nanoporous Alumina Films with Arbitrary Pore Intervals by Critical-Potential Anodization". In: *Journal of The Electrochemical Society* 153.9 (2006), B384.

[94] O. Jessensky, F. Müller, and U. Gösele. "Self-organized formation of hexagonal pore structures in anodic alumina". In: *Journal of The Electrochemical Society* 145.11 (Nov. 1998), pp. 3735–3740.

[95] O. Jessensky, F. Müller, and U. Gösele. "Self-organized formation of hexagonal pore arrays in anodic alumina". In: *Applied Physics Letters* 72.10 (Mar. 1998), pp. 1173–1175.

[96] Ferdi Schüth and Stephan Andreas Schunk. "Synthesis of zeolite-like inorganic compounds". In: *ChemInform* 29 (1998), pp. 229–263.

[97] Ying Ma, Wei Tong, Hua Zhou, and Steven L. Suib. "A review of zeolite-like porous materials". In: *Microporous and Mesoporous Materials* 37.1 (2000), pp. 243–252.

[98] Martin E. Nordberg. "Poperties of some vycor-brand glasses". In: *Journal of the American Ceramic Society* 29 (1944), pp. 299–305.

[99] C. Hodgson and R. McIntosh. "The freezing of water and benzene in porous vycor glass". In: *Canadian Journal of Chemistry* 38.6 (1960), pp. 958–971.

[100] Z. Zhao, Q. Huo, J. Feng, B.F. Chmelka, and G.D. Stucky. "Nonionic Triblock and Star Diblock Copolymer and Oligomeric Surfactant Syntheses of Highly Ordered, Hydrothermally Stable, Mesoporous Silica Structures". In: *J. Am. Chem. Soc.* 120 (1998), p. 6024.

[101] Tomas Kjellman, Nina Reichhardt, Motolani Sakeye, Jan-Henrik Smått, Mika Lindén, and Viveka Alfredsson. "Independent Fine-Tuning of the Intrawall Porosity and Primary Mesoporosity of SBA-15". In: *Chemistry of Materials* 25.9 (2013), pp. 1989–1997.

[102] Filiz Sevimli and Ayşen Yılmaz. "Surface functionalization of SBA-15 particles for amoxicillin delivery". In: *Microporous and Mesoporous Materials* 158.0 (2012), pp. 281–291.

[103] Haifeng Yang, Qihui Shi, Bozhi Tian, Songhai Xie, Fuqiang Zhang, Yan, Bo Tu, and Dongyuan Zhao. "A Fast Way for Preparing Crack-Free Mesostructured Silica Monolith". In: *Chemistry of Materials* 15.2 (2003), pp. 536–541.

[104] P. G. de Gennes, F. Brochard-Wyart, and D. Quere. *Capillarity and Wetting Phenomena: Drops, Bubbles, Pearls, Waves*. New York: Springer, 2004.

[105] Lulu Wang, Haiying Huang, and Tianbai He. "Rayleigh Instability Induced Cylinder-to-Sphere Transition in Block Copolymer Micelles: Direct Visualization of the Kinetic Pathway". In: *ACS Macro Letters* 3.5 (2014), pp. 433–438.

[106] Nan Yan, Yuping Sheng, Hongxia Liu, Yutian Zhu, and Wei Jiang. "Templated Self-Assembly of Block Copolymers and Morphology Transformation Driven by the Rayleigh Instability". In: *Langmuir* 31.5 (2015), pp. 1660–1669.

[107] María Esperanza Adrover, Marisa Pedernera, Magali Bonne, Bénédicte Lebeau, Verónica Bucalá, and Loreana Gallo. "Synthesis and characterization of mesoporous SBA-15 and SBA-16 as carriers to improve albendazole dissolution rate". In: *Saudi Pharmaceutical Journal* 28.1 (2020), pp. 15–24.

[108] Olivier Guillon, Jesus Gonzalez-Julian, Benjamin Dargatz, Tobias Kessel, Gabi Schierning, Jan Räthel, and Mathias Herrmann. "Field-Assisted Sintering Technology/Spark Plasma Sintering: Mechanisms, Materials, and Technology Developments". In: *Advanced Engineering Materials* 16.7 (2014), p. 830.

[109] Ambreen Nisar, Cheng Zhang, Benjamin Boesl, and Arvind Agarwal. "Unconventional Materials Processing Using Spark Plasma Sintering". In: *Ceramics* 4.1 (2021), pp. 20–39.

[110] Martha Guerrero, Mile B. Djurdjević, Srećko Manasijević, Zoran Odanović, and Natalija Dolić. "Calculation of Liquidus Temperature for Aluminum and Magnesium Alloys Applying Method of Equivalency". In: *Advances in Materials Science and Engineering* 2013 (2013), p. 170527.

[111] W.A. Mohun. "A novel amorphous carbon". In: *Proceedings of the Conference on Carbon*. Vol. 4. Elsevier, 1960, pp. 443–453.

[112] A. K. Kuriakose and J. L. Margrave. "Kinetics of the Reactions of Elemental Fluorine with Zirconium Carbide and Zirconium Diboride at High Temperatures". In: *The Journal of Physical Chemistry* 68.2 (Feb. 1964), pp. 290–295.

[113] A. K. Kuriakose and J. L. Margrave. "Kinetics of Reaction of Elemental Fluorine. II. The Fluorination of Hafnium Carbide and Hafnium Boride". In: *The Journal of Physical Chemistry* 68.8 (Aug. 1964), pp. 2343–2345.

[114] Nathan S. Jacobson, Yury G. Gogotsi, and Masahiro Yoshimura. "Thermodynamic and experimental study of carbon formation on carbides under hydrothermal conditions". In: *Journal of Materials Chemistry* 5.4 (1995), pp. 595–601.

[115] Gleb N. Yushin, Elizabeth N. Hoffman, Alexei Nikitin, Haihui Ye, Michel W. Barsoum, and Yury Gogotsi. "Synthesis of nanoporous carbide-derived carbon by chlorination of titanium silicon carbide". In: *Carbon* 43.10 (2005), pp. 2075–2082.

[116] Yury Gogotsi, Ranjan K. Dash, Gleb Yushin, Taner Yildirim, Giovanna Laudisio, and John E. Fischer. "Tailoring of Nanoscale Porosity in Carbide-Derived Carbons for Hydrogen Storage". In: *Journal of the American Chemical Society* (2005).

[117] Patrice Simon and Yury Gogotsi. "Materials for electrochemical capacitors". In: *Nature Materials* 7.11 (Nov. 2008), pp. 845–854.

[118] Boris Dyatkin, Eugene Mamontov, Kevin M. Cook, and Yury Gogotsi. "Capacitance, charge dynamics, and electrolyte-surface interactions in functionalized carbide-derived carbon electrodes". In: *Progress in Natural Science: Materials International* 25.6 (2015), pp. 631–641.

[119] François Béguin, Volker Presser, Andrea Balducci, and Elzbieta Frackowiak. "Carbons and Electrolytes for Advanced Supercapacitors". In: *Advanced Materials* 26.14 (2014), pp. 2219–2251.

[120] Volker Presser, Min Heon, and Yury Gogotsi. "Carbide-Derived Carbons – From Porous Networks to Nanotubes and Graphene". In: *Advanced Functional Materials* 21.5 (Mar. 2011), pp. 810–833.

[121] Jayesh Cherusseri, Kowsik Sambath Kumar, Nitin Choudhary, Narasimha Nagaiah, Yeonwoong Jung, Tania Roy, and Jayan Thomas. "Novel mesoporous electrode materials for symmetric, asymmetric and hybrid supercapacitors". In: *Nanotechnology* 30.20 (2019), p. 202001.

[122] Boris Dyatkin and Yury Gogotsi. "Effects of structural disorder and surface chemistry on electric conductivity and capacitance of porous carbon electrodes". In: *Faraday Discussions* 172.0 (2014), pp. 139–162.

[123] S. Lowell, J.E. Shields, M.A. Thomas, and M. Thommes. *Characterization of Porous Solids and Powders: Surface Area, Pore Size and Density*. Particle Technology Series. Springer Netherlands, 2010.

[124] Joona Bang, Unyong Jeong, Du Yeol Ryu, Thomas P. Russell, and Craig J. Hawker. "Block Copolymer Nanolithography: Translation of Molecular Level Control to Nanoscale Patterns". In: *Advanced Materials* 21.47 (Dec. 2009), pp. 4769–4792.

[125] G. Mason and Douglas Hugh Everett. "A model of adsorption-desorption hysteresis in which hysteresis is primarily developed by the interconnections in a network of pores". In: *Proceedings of the Royal Society of London. Series A - Mathematical and Physical Sciences* 390.1798 (Nov. 1983), pp. 47–72.

[126] Geoffrey Mason. "The effect of pore space connectivity on the hysteresis of capillary condensation in adsorption-desorption isotherms". In: *Journal of Colloid and Interface Science* 88.1 (July 1982), pp. 36–46.

[127] W. F. Saam and Milton W. Cole. "Excitations and thermodynamics for liquid-helium films". In: *Physical Review B* 11.3 (Feb. 1975), pp. 1086–1105.

[128] Stephen Brunauer, P. H. Emmett, and Edward Teller. "Adsorption of Gases in Multimolecular Layers". In: *Journal of the American Chemical Society* 60.2 (Feb. 1938), pp. 309–319.

[129] Elliott P. Barrett, Leslie G. Joyner, and Paul P. Halenda. "The Determination of Pore Volume and Area Distributions in Porous Substances. I. Computations from Nitrogen Isotherms". In: *Journal of the American Chemical Society* 73.1 (Jan. 1951), pp. 373–380.

[130] J. Frenkel. *Kinetic Theory of Liquids*. Dover, 1955.

[131] George Halsey. "Physical Adsorption on non-uniform surfaces". In: *The Journal of Chemical Physics* 16.10 (Oct. 1948), pp. 931–937.

[132] Terrell L. Hill. "Theory of Physical Adsorption". In: *Advances in Catalysis*. Ed. by W. G. Frankenburg, V. I. Komarewsky, and E. K. Rideal. Vol. 4. Academic Press, 1952, pp. 211–258.

[133] Rémi Lazzari, Frédéric Leroy, and Gilles Renaud. "Grazing-incidence small-angle x-ray scattering from dense packing of islands on surfaces: Development of distorted wave Born approximation and correlation between particle sizes and spacing". In: *Physical Review B* 76.12 (Sept. 2007), p. 125411.

[134] Gilles Renaud, Rémi Lazzari, and Frédéric Leroy. "Probing surface and interface morphology with Grazing Incidence Small Angle X-Ray Scattering". In: *Surface Science Reports* 64.8 (2009), pp. 255–380.

[135] B.E. Warren. *X-Ray Diffraction*. Dover Books on Physics. Dover Publications, 2012.

[136] Markus Rauscher, Rogerio Paniago, Hartmut Metzger, Zoltan Kovats, Jan Domke, Johann Peisl, Hans-Dieter Pfannes, Jörg Schulze, and Ignaz Eisele. "Grazing incidence small angle x-ray scattering from free-standing nanostructures". In: *Journal of Applied Physics* 86.12 (Dec. 1999), pp. 6763–6769.

[137] J. Daillant and A. Gibaud. *X-ray and Neutron Reflectivity: Principles and Applications*. Lecture Notes in Physics. Springer Berlin Heidelberg, 2008.

[138] J. Als-Nielsen and D. McMorrow. *Elements of Modern X-ray Physics*. Wiley, 2011.

[139] R. E. Collins and C. E. Cooke. "Fundamental basis for the contact angle and capillary pressure". In: *Transactions of the Faraday Society* 55.0 (1959), pp. 1602–1606.

[140] S. Safran. *Statistical Thermodynamics Of Surfaces, Interfaces, And Membranes*. Frontiers in Physics. Avalon Publishing, 2003.

[141] P.G. de Gennes, F. Brochard-Wyart, and D. Quere. *Capillarity and Wetting Phenomena: Drops, Bubbles, Pearls, Waves*. Springer New York, 2003.

[142] Robert N. Wenzel. "Resistance of solid surfaces to wetting by water". In: *Industrial & Engineering Chemistry* 28.8 (Aug. 1936), pp. 988–994.

[143] Robert N. Wenzel. "Surface Roughness and Contact Angle." In: *The Journal of Physical and Colloid Chemistry* 53.9 (Sept. 1949), pp. 1466–1467.

[144] A.B.D. Cassie and S. Baxter. "Wettability of porous surfaces". In: *Transactions of the Faraday Society* 40.0 (1944), pp. 546–551.

[145] A.B.D. Cassie. "Contact angles". In: *Discussions of the Faraday Society* 3.0 (1948), pp. 11–16.

[146] J.N. Israelachvili. *Intermolecular and Surface Forces*. Elsevier Science, 2015.

[147] R. Evans. "The nature of the liquid-vapour interface and other topics in the statistical mechanics of non-uniform, classical fluids". In: *Advances in Physics* 28.2 (Apr. 1979), pp. 143–200.

[148] M. Tasinkevych and S. Dietrich. "Complete wetting of pits and grooves". In: *The European Physical Journal E* 23.1 (May 2007), pp. 117–128.

[149] M. Tasinkevych and S. Dietrich. "Complete Wetting of Nanosculptured Substrates". In: *Phys. Rev. Lett.* 97 (10 Sept. 2006), p. 106102.

[150] D. Cline. *Variational Principles in Classical Mechanics: 2nd Edition*. River Campus Libraries, 2018.

[151] R. Becker. *Theorie der Wärme*. Heidelberger Taschenbücher. Springer, 1966.

[152] C. Rascón and A. O. Parry. "Geometry-dominated fluid adsorption on sculpted solid substrates". In: *Nature* 407.6807 (2000), pp. 986–989.

[153] M. Impéror-Clerc, P. Davidson, and A. Davidson. "Existence of a microporous corona around the mesopores of silica-based SBA-15 materials templated by triblock copolymers". In: *Journal of the American Chemical Society* 122.48 (2000), pp. 11925–11933.

[154] Cedric J. Gommes, Heiner Friedrich, Mariska Wolters, Petra E. de Jongh, and Krijn P. de Jong. "Quantitative Characterization of Pore Corrugation in Ordered Mesoporous Materials Using Image Analysis of Electron Tomograms". In: *Chemistry of Materials* 21.7 (2009), pp. 1311–1317.

[155] Lulu Wang, Haiying Huang, and Tianbai He. "Rayleigh Instability Induced Cylinder-to-Sphere Transition in Block Copolymer Micelles: Direct Visualization of the Kinetic Pathway". In: *ACS Macro Letters* 3.5 (2014), pp. 433–438.

[156] Wenlong Wang, Cunyao Li, Li Yan, Yuqing Wang, Miao Jiang, and Yunjie Ding. "Ionic Liquid/Zn-PPh3 Integrated Porous Organic Polymers Featuring Multifunctional Sites: Highly Active Heterogeneous Catalyst for Cooperative Conversion of CO2 to Cyclic Carbonates". In: *ACS Catalysis* 6.9 (Sept. 2016), pp. 6091–6100.

[157] Cedric J. Gommes. "Adsorption, Capillary Bridge Formation, and Cavitation in SBA-15 Corrugated Mesopores: A Derjaguin-Broekhoff-de Boer Analysis". In: *Langmuir* 28.11 (2012), pp. 5101–5115.

[158] I.F. Silvera. "The Solid Molecular Hydrogens in the Condensed Phase - Fundamentals and Static Properties". English. In: *Review of Modern Physics* 52.2 (1980), pp. 393–452.

[159] J. L. Yarnell, R. L. Mills, and A. F. Schuch. "Neutron diffraction studies of deuterium solid structures and transitions". In: *Sov. J. Low Temp. Phys.* 1 (1975), p. 366.

[160] K.F. Niebel and J.A. Venables. "An Explanation of the Crystal Structure of the Rare Gas Solids". In: *Proceedings of the Royal Society of London. Series A - Mathematical and Physical Sciences* 336.1606 (Feb. 1974), pp. 365–377.

[161] M. Kempa, B. Janousova, J. Saroun, P. Flores, M. Boehm, F. Demmel, and J. Kulda. "The FlatCone multianalyzer setup for ILL's three-axis spectrometers". In: *Physica B: Condensed Matter* 385-386 (2006), pp. 1080–1082.

[162] J. Kulda, J. Šaroun, P. Courtois, M. Enderle, M. Thomas, and P. Flores. "IN20 –The ILL high-flux polarised-neutron three-axis spectrometer". In: *Applied Physics A* 74.1 (2002), s246–s248.

[163] T.A. Scott. "Solid and liquid nitrogen". In: *Physics Reports* 27.3 (1976), pp. 89–157.

[164] A.F. Schuch and R.L. Mills. "Crystal Structure of Deuterium at Low Temperatures". In: *Phys. Rev. Lett.* 16.14 (Apr. 1966), p. 616.

[165] M. Nielsen and H. Bjerrum Møller. "Lattice Dynamics of Solid Deuterium by Inelastic Neutron Scattering". In: *Physical Review B* 3.12 (June 1971), pp. 4383–4385.

[166] J.K. Kjems and G. Dolling. "Crystal dynamics of nitrogen: The cubic α-phase". In: *Physical Review B* 11.4 (Feb. 1975), pp. 1639–1647.

[167] J.U. Hoffmann and M. Reehuis. "E2: The Flat-Cone Diffractometer at BER II". In: *Journal of large-scale research facilities* 4 (2018), A129.

[168] Yu.A. Freiman and H.J. Jodl. "Solid oxygen". In: *Physics Reports* 401.1-4 (Nov. 2004), pp. 1–228.

[169] Alexandra Buchsteiner and Norbert Stüßer. "Optimizations in angular dispersive neutron powder diffraction using divergent beam geometries". In: *Nuclear Instruments and Methods in Physics Research Section A: Accelerators, Spectrometers, Detectors and Associated Equipment* 598.2 (2009), pp. 534–541.

[170] K. Seevakan and S. Bharanidharan. "Different types of crystal growth methods". In: *International Journal of Pure and Applied Mathematics* 119 (Jan. 2018), pp. 5743–5758.

[171] Gary C. DeFotis. "Transformation characteristics and orientation relations among the phases of solid oxygen". In: *The Journal of Chemical Physics* 71.12 (Dec. 1979), pp. 5336–5351.

[172] C. S. Barrett, Lothar Meyer, and J. Wasserman. "Expansion Coefficients and Transformation Characteristics of Solid Oxygen". In: *Physical Review* 163.3 (Nov. 1967), pp. 851–854.

[173] A. Henschel, P. Kumar, T. Hofmann, K. Knorr, and P. Huber. "Prefered Orientation of n-Hexane Crystallized in Silicon Nanochannels: A combined X-ray Diffraction and Sorption Isotherm Study". In: *Physical Review E* 79 (2009), p. 032601.

[174] A. Henschel, T. Hofmann, P. Huber, and K. Knorr. "Preferred orientations and stability of medium length n-alkanes solidified in mesoporous silicon". In: *Physical Review E* 75.2 (Feb. 2007), p. 021607.

[175] Benjamin D. Hamilton, Jeong-Myeong Ha, Marc A. Hillmyer, and Michael D. Ward. "Manipulating Crystal Growth and Polymorphism by Confinement in Nanoscale Crystallization Chambers". In: *Accounts of Chemical Research* 45.3 (Mar. 2012), pp. 414–423.

[176] David P. McMahon, David L. Cheung, Ludwig Goris, Javier Dacuña, Alberto Salleo, and Alessandro Troisi. "Relation between Microstructure and Charge Transport in Polymers of Different Regioregularity". In: *The Journal of Physical Chemistry C* 115.39 (Oct. 2011), pp. 19386–19393.

[177] Carl Poelking, Kostas Daoulas, Alessandro Troisi, and Denis Andrienko. "Morphology and Charge Transport in P3HT: A Theorist's Perspective". In: *P3HT Revisited –From Molecular Scale to Solar Cell Devices*. Ed. by Sabine Ludwigs. Berlin, Heidelberg: Springer Berlin Heidelberg, 2014, pp. 139–180.

[178] Oleksandr V. Mikhnenko, Paul W.M. Blom, and Thuc-Quyen Nguyen. "Exciton diffusion in organic semiconductors". In: *Energy & Environmental Science* 8.7 (2015), pp. 1867–1888.

[179] Burak Kadem, Aseel Hassan, and Wayne Cranton. "Efficient P3HT : PCBM bulk heterojunction organic solar cells; effect of post deposition thermal treatment". In: *Journal of Materials Science: Materials in Electronics* 27.7 (2016), pp. 7038–7048.

[180] Guangzhu Ding, Kaixuan Wang, Xiaohui Li, Qing Chen, Zhijun Hu, and Jieping Liu. "The Fabrication of Nanoimprinted P3HT Nanograting by Patterned ETFE Mold at Room Temperature and Its Application for Solar Cell". In: *Nanoscale Research Letters* 11.1 (2016), p. 258.

[181] B.M. Ocko, X. Z. Wu, E. B. Sirota, S. K. Sinha, O. Gang, and M. Deutsch. "Surface freezing in chain molecules: Normal alkanes". In: *Physical Review E* 55.3 (Mar. 1997), pp. 3164–3182.

[182] Zhijun Hu, Benoît Muls, Loïk Gence, Dana A. Serban, Johan Hofkens, Sorin Melinte, Bernard Nysten, Sophie Demoustier-Champagne, and Alain M. Jonas. "High-Throughput Fabrication of Organic Nanowire Devices with Preferential Internal Alignment and Improved Performance". In: *Nano Letters* 7.12 (Dec. 2007), pp. 3639–3644.

[183] Léon Van Hove. "Correlations in Space and Time and Born Approximation Scattering in Systems of Interacting Particles". In: *Physical Review* 95.1 (July 1954), pp. 249–262.

[184] G.L. Squires. *Introduction to the Theory of Thermal Neutron Scattering*. Cambridge University Press, 2012.

[185] Günter Schatz and Alois Weidinger. "Neutronenstreuung". In: *Nukleare Festkörperphysik: Kernphysikalische Meßmethoden und ihre Anwendungen*. Ed. by Günter Schatz and Alois Weidinger. Wiesbaden: Vieweg+Teubner Verlag, 1992, pp. 226–257.

[186] A. Furrer, J.F. Mesot, and T. Straessle. *Neutron Scattering In Condensed Matter Physics*. Series On Neutron Techniques And Applications. World Scientific Publishing Company, 2009.

[187] W. Marshall and S.W. Lovesey. *Theory of Thermal Neutron Scattering: The Use of Neutrons for the Investigation of Condensed Matter*. International series of monographs on physics. Clarendon Press, 1971.

[188] M. Bée. "A physical insight into the elastic incoherent structure factor". In: *Physica B: Condensed Matter* 182.4 (1992), pp. 323–336.

[189] J. Baumert, B. Asmussen, C. Gutt, and R. Kahn. "Pore-Size Dependence of the Self-Diffusion of Hexane in Silica Gels". In: *The Journal of Chemical Physics* 116.24 (2002), pp. 10869–10876.

[190] David W. McCall, Dean C. Douglass, and Ernest W. Anderson. "Self-Diffusion in Liquids: Paraffin Hydrocarbons". In: *The Physics of Fluids* 2.1 (Jan. 1959), pp. 87–91.

[191] S. Janßen, J. Mesot, L. Holitzner, A. Furrer, and R. Hempelmann. "FOCUS: a hybrid TOF-spectrometer at SINQ". In: *Physica B: Condensed Matter* 234-236 (1997), pp. 1174–1176.

[192] Bernhard Frick, Eugene Mamontov, Lambert van Eijck, and Tilo Seydel. "Recent Backscattering Instrument Developments at the ILL and SNS". In: Zeitschrift für Physikalische Chemie 224.1-2 (2010), pp. 33–60.

[193] G. Shirane, S.M. Shapiro, and J.M. Tranquada. *Neutron Scattering with a Triple-Axis Spectrometer: Basic Techniques*. Cambridge University Press, 2002.

[194] M.D. Le, D.L. Quintero-Castro, R. Toft-Petersen, F. Groitl, M. Skoulatos, K.C. Rule, and K. Habicht. "Gains from the upgrade of the cold neutron triple-axis spectrometer FLEXX at the BER-II reactor". In: *Nuclear Instruments and Methods in Physics Research Section A: Accelerators, Spectrometers, Detectors and Associated Equipment* 729 (Nov. 2013), pp. 220–226.

[195] C. Kittel. *Introduction to Solid State Physics*. Wiley, 1996.

[196] Oleg Sobolev and Jitae T. Park. "PUMA: Thermal three axes spectrometer". In: *Journal of large-scale research facilities JLSRF* 1.A13 (2015), pp. 1–4.

[197] R. Gross and A. Marx. *Festkörperphysik*. De Gruyter Studium. De Gruyter, 2018.

[198] Matthew C. Wingert, Soonshin Kwon, Ming Hu, Dimos Poulikakos, Jie Xiang, and Renkun Chen. "Sub-amorphous Thermal Conductivity in Ultrathin Crystalline Silicon Nanotubes". In: *Nano Letters* 15.4 (Apr. 2015), pp. 2605–2611.

[199] G.N. Aliev, B. Goller, and P.A. Snow. "Elastic properties of porous silicon studied by acoustic transmission spectroscopy". In: *Journal of Applied Physics* 110.4 (2011), p. 043534.

[200] G.T. Andrews, A.M. Polomska, E. Vazsonyi, and J. Volk. "Brillouin light scattering from porous silicon films and multilayers". In: *Physica Status Solidi (a)* 204.5 (2007), pp. 1372–1377.

[201] Christian Chmelik, Dirk Enke, Petrik Galvosas, Oliver Gobin, Andreas Jentys, Hervé Jobic, Jörg Kärger, Cordula B. Krause, Jens Kullmann, Johannes Lercher, Sergej Naumov, Douglas M. Ruthven, and Tobias Titze. "Nanoporous Glass as a Model System for a Consistency Check of the Different Techniques of Diffusion Measurement". In: *ChemPhysChem* 12.6 (2011), pp. 1130–1134.

[202] Daria Kondrashova, Alexander Lauerer, Dirk Mehlhorn, Hervé Jobic, Armin Feldhoff, Matthias Thommes, Dipanjan Chakraborty, Cedric Gommes, Jovana Zecevic, Petra de Jongh, Armin Bunde, Jörg Kärger, and Rustem Valiullin. "Scale-dependent diffusion anisotropy in nanoporous silicon". In: *Scientific Reports* 7 (Jan. 2017), p. 40207.

[203] L. Canham. *Handbook of Porous Silicon*. Handbook of Porous Silicon. Springer International Publishing, 2014.

[204] Klaus Habicht. *Neutron-Resonance Spin-Echo Spectroscopy: A High Resolution Look at Dispersive Excitations*. Habilitationsschrift Universität Potsdam. 2017.

[205] Joseph Callaway. "Model for Lattice Thermal Conductivity at Low Temperatures". In: *Physical Review* 113.4 (Feb. 1959), pp. 1046–1051.

[206] Changwook Jeong, Supriyo Datta, and Mark Lundstrom. "Thermal conductivity of bulk and thin-film silicon: A Landauer approach". In: *Journal of Applied Physics* 111.9 (May 2012), p. 093708.

[207] Austin Minnich and Gang Chen. "Modified effective medium formulation for the thermal conductivity of nanocomposites". In: *Applied Physics Letters* 91.7 (2007), p. 073105.

[208] K. Pietrak and T.S. Wiśniewski. "A review of models for effective thermal conductivity of composite materials". In: *Journal of Power Technologies* 95.1 (2015), pp. 14–24.

[209] Ce-Wen Nan, R. Birringer, David R. Clarke, and H. Gleiter. "Effective thermal conductivity of particulate composites with interfacial thermal resistance". In: *Journal of Applied Physics* 81.10 (1997), pp. 6692–6699.

Key Publications

[32] T. Hofmann, E. Dobisz, and B. M. Ocko. "Grazing incident small angle x-ray scattering: A metrology to probe nanopatterned surfaces". In: *Journal of Vacuum Science & Technology B* 27.6 (2009), pp. 3238–3243.

[33] T. Hofmann, M. Tasinkevych, A. Checco, E. Dobisz, S. Dietrich, and B. M. Ocko. "Wetting of Nanopatterned Grooved Surfaces". In: *Phys. Rev. Lett.* 104 (10 Mar. 2010), p. 106102.

[34] Tommy Hofmann, Dirk Wallacher, Maria Mayorova, Reiner Zorn, Bernhard Frick, and Patrick Huber. "Molecular dynamics of n-hexane: A quasi-elastic neutron scattering study on the bulk and spatially nanochannel-confined liquid". In: *The Journal of Chemical Physics* 136.12 (2012), p. 124505.

[35] T. Hofmann, P. Kumar, M. Enderle, and D. Wallacher. "Growth of Highly Oriented Deuterium Crystals in Silicon Nanochannels". In: *Physical Review Letters* 110.6 (Feb. 2013), pp. 065505–.

[36] Danny Kojda, Dirk Wallacher, Simon Baudoin, Thomas Hansen, Patrick Huber, and Tommy Hofmann. "Solid phases of spatially nanoconfined oxygen: A neutron scattering study". In: *The Journal of Chemical Physics* 140.2 (2014), p. 024705.

[37] Tommy Hofmann, Dirk Wallacher, Jan Perlich, Sarathlal Koyiloth Vayalil, and Patrick Huber. "Formation of Periodically Arranged Nanobubbles in Mesopores: Capillary Bridge Formation and Cavitation during Sorption and Solidification in an Hierarchical Porous SBA-15 Matrix". In: *Langmuir* 32.12 (Mar. 2016), pp. 2928–2936.

[38] Tommy Hofmann, Dirk Wallacher, Rasmus Toft-Petersen, Britta Ryll, Manfred Reehuis, and Klaus Habicht. "Phonons in mesoporous silicon: The influence of nanostructuring on the dispersion in the Debye regime". In: *Microporous and Mesoporous Materials* 243 (May 2017), pp. 263–270.

[39] Tommy Hofmann, Danny Kojda, Haider Haseeb, Dirk Wallacher, Oleg Sobolev, and Klaus Habicht. "Phonons in highly-crystalline mesoporous silicon: The absence of phonon-softening upon structuring silicon on sub-10 nanometer length scales". In: *Microporous and Mesoporous Materials* 312 (2021), p. 110814.

[40] N. Gostkowska-Lekner, D. Wallacher, N. Grimm, K. Habicht, and T. Hofmann. "A novel electrochemical anodization cell for the synthesis of mesoporous silicon". In: *Review of Scientific Instruments* 91.10 (2020), p. 105113.

[41] Danny Kojda, Tommy Hofmann, Natalia Gostkowska-Lekner, and Klaus Habicht. “Characterization and modeling of the temperature-dependent thermal conductivity in sintered porous silicon-aluminum nanomaterials”. In: *Nano Research* 15.6 (2022), pp. 5663–5670.

[42] Antonio Checco, Tommy Hofmann, Elaine DiMasi, Charles T. Black, and Benjamin M. Ocko. “Morphology of Air Nanobubbles Trapped at Hydrophobic Nanopatterned Surfaces”. In: *Nano Letters* 10.4 (Apr. 2010), pp. 1354–1358.

[43] Oleg Gang, Antonio Checco, Tommy Hofmann, Du Yeol Ryu, Thomas P. Russell, and Benjamin M. Ocko. “Liquid adsorption at surfaces patterned with cylindrical nano-cavities”. In: *Soft Matter* 9.44 (2013), pp. 10550–10558.

[44] Htay Hlaing, Xinhui Lu, Tommy Hofmann, Kevin G. Yager, Charles T. Black, and Benjamin M. Ocko. “Nanoimprint-Induced Molecular Orientation in Semiconducting Polymer Nanostructures”. In: *ACS Nano* 5.9 (Sept. 2011), pp. 7532–7538.

[45] Mark Busch, Tommy Hofmann, Bernhard Frick, Jan P. Embs, Boris Dyatkin, and Patrick Huber. “Ionic liquid dynamics in nanoporous carbon: A pore-size- and temperature-dependent neutron spectroscopy study on supercapacitor materials”. In: *Physical Review Materials* 4.5 (May 2020), pp. 055401–.

List of Figures